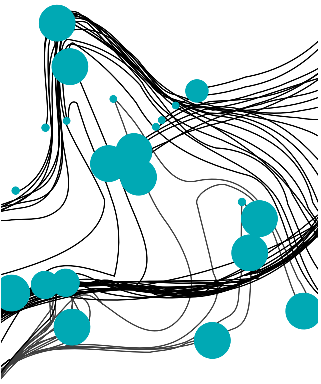

RAM ROBOTICS AND MECHATRONICS

MODELING, DESIGN AND CHARACTERIZATION OF A 3D-PRINTED CAPACITIVE SHEAR STRESS SENSOR

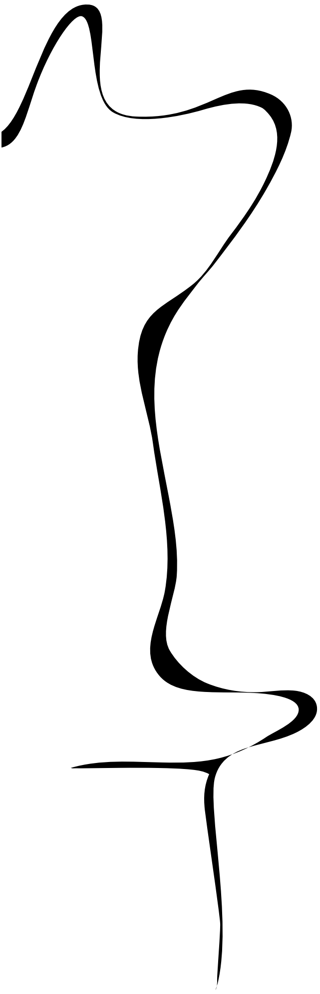

J. (Jens) Oprel

BSC ASSIGNMENT

Committee:
prof. dr. ir. G.J.M. Krijnen
G.J.W. Wolterink, MSc
dr. ir. J.P. Schilder

April, 2021

021RaM2021
Robotics and Mechatronics
EEMCS
University of Twente
P.O. Box 217
7500 AE Enschede
The Netherlands

UNIVERSITY OF TWENTE. | TECHMED CENTRE

UNIVERSITY OF TWENTE. | DIGITAL SOCIETY INSTITUTE

Summary

This bachelor assignment concerns the modelling, design, fabrication and characterization of a 3D-printed shear stress sensor. The design is optimized for application in measurements on the human foot, which are interesting for health related applications. More specifically, shear stress monitoring could help to prevent development of diabetic foot ulcers.

This application imposes some requirements and objectives. Measurement range, accuracy of peak measurements and the sensor dimensions are the most crucial points of attention. Based on these requirements and objectives, capacitive sensing and Fused Deposition Modelling printing are selected as most promising sensing and printing principles.

Theoretical models are developed to study the electrostatic (capacitive) and mechanical behavior of sensing structures. The electrostatic model introduces an approximation for structures of parallel wires. The mechanical model is based upon an hyperelastic beam model. Finite Element Methods are used for verification of the models. These models are used to optimize the design of the sensor, which consists of 3 sets of 3 electrodes in a beam structure. These are used to measure differential capacitance changes using a capacitance to digital converter.

The results show that it is possible to measure shear stresses. The smallest fabricated sensor with dimensions of $8.75 \times 8.75 \times 11\,\mathrm{mm}$ has a sensitivity of $0.9\,\mathrm{pF/MPa}$ in the measurement range of 0 to 140 kPa. The fabricated sensors show a linear displacement-capacitance relation. The mechanical behavior of the sensor shows some hysteresis. The durability and repeatability of measurements are main points of attention that need further research if the sensor is to be applied for shear force measurements on the foot.

Acknowledgements

This thesis is the result of my Bachelor Assignment for my study Advanced Technology. In this 11 week project, I got the chance to work on a very interesting and challenging project on the modelling and design of a capacitive shear force sensor.

The adventure started at the end of 2019 when Gijs Krijnen took the time to introduce me to the world of 3D-printed sensors. I really appreciated the time that Gijs took to find a project that best fit my interests. Also during the project Gijs kept bringing up interesting questions and ideas that gave more direction to my project. In the final stage of the project, Gijs spent a lot of time on providing me very valuable feedback. Thanks for everything, Gijs!

Throughout the project, I was supervised by Gerjan Wolterink, who was always available to answer questions and share some of his thoughts on the challenges along the way. Towards the end of the project I was given the possibility to go into the lab to test the ideas that were the result of my modelling work. I am really happy that this was possible given the restrictions imposed by the current pandemic. During this lab work, the experience of Gerjan with the practical issues associated with printing sensors was of great help. I'd like to thank Gerjan for all his guidance, and contributions during the project!

During the experimentation phase, Dimitris helped me with the capacitive measurements. I'd like to thank him for the time he took to provide me the tools and kwow-how necessary to perform these measurements, especially since measuring a capacitance is kind of crucial for a capacitive sensor... I'd also like to thank all other members from the NIFTy (Nature Inspired Fabrication and Transduction) group for their inputs during the bi-weekly meetings.

I'd like to thank Jurnan Schilder for his input during the mid-term meeting and for being part of my examination committee.

I'd like to thank my parents for providing me all their support in different forms. For example providing me a nice workplace at home, or a fun week to go ice skating in between the modelling process, just to name a few...

Also in Enschede, I'm grateful to my housemates for having a environment to work in, and all fun things at home, which is important in these times... In special, I'd like to thank Juul, who has been my fellow AT-student and housemate for my entire study and has learnt me a lot, especially in the projects that we did together during this time. I'd also like to specially thank Emiel for all the fun evenings we had during this project, which often end in an interesting discussion. His critical thoughts were valuable in this project.

Last but certainly not least, I'd like to thank Imme, my girlfriend, for all her support throughout this project and the rest of my studies (and accepting that some of my weekends were filled with sensors).

Enjoy!

Jens
April 2020

Contents

1 Introduction

Shear stresses on the human foot

Measurements of stresses on the human foot are interesting for health related applications. Specifically, shear and normal stresses [1–3] play an important role in development of foot ulcers. This is especially relevant for persons with diabetes, who have increased risk at ulcers on the feet [4]. Furthermore, shear stress peak locations [5] are a good indicator of risk locations for ulcer development. As the effects of development of Diabetic Foot Ulcers (DFUs) are large, both for the patient and for society, there is interest in technology for prevention of DFUs [1]. Measurements are useful in a clinical setting [2]. Additionally, monitoring shear stresses during daily life at the feet of risk-patients can be valuable in the prevention of DFU deveopment for a group of patients [2]. Partially because the monitoring can help in advising about physical activity for patients [1], which is currently a challenging trade-off for clinicians.

3D-printed sensors

In recent research, 3D-printing is shown to be a viable method to fabricate sensors [6–11]. Potential fields of applications include robotics and medicine (e.g. in prothesis and orthoses). Compared to other manufacturing methods, Additive Manufacturing, or 3D-printing, has various advantages [6, 9]: the initial costs are low, which is especially advantageous if a small number of parts is needed. Additionally each part can be customized and sensors and electrical interfacing can be integrated into a single part.

Goal

As discussed in Section 1, measurements of shear stress on the feet can prove to be of value both in clinical settings as in daily life of persons with diabetes. Furthermore, a shoe fit is very important for this group [12]. For that reason, soles or insoles are often custom made. In recent research [13, 14], 3D-printing was used to successfully optimize the fit of insoles such that pressures on the foot are reduced. In addition 3D-printed sensors have already been developed for various applications. If a suitable shear stress sensor could be developed, a single 3D-printed object could be customized for fitting and sensing purposes.

The goal of this project is to design a 3D-printed sensor that can be implemented in shoe insoles and that is capable of monitoring shear stresses on the feet of persons with diabetes in a daily life environment. The following research questions need to be answered to achieve this goal:

- What are requirements for a 3D-printed sensor applied for monitoring shear stress on the feet (of diabetic persons)?
- What are suitable sensing techniques for the sensor?
- What are suitable printing techniques for the sensor?
- How can a capacitive shear stress sensor be modelled?
- Which parameters determine the performance of a shear stress sensor and what are optimal parameters?
- Can an optimized 3D-printed shear stress sensor design meet the requirements?

Previous work

There are already non-printed sensors developed to measure stresses on the foot [2], both commercially and research based. The commercial sensors in general have a better spatial resolution than the research based systems, with systems of a few hundred sensors. However, most commercial systems only measure normal stresses. Some research-based systems [15, 16] are able to measure shear stresses (possibly in addition to normal stresses, in which case it is a multiaxial system [2]). The use of these sensors is not common in clinical settings [2], let alone in daily life measurements. The main reason for this is the high cost of the sensing systems. Also the required spatial resolution and wish for multiaxial measurements are a cause of this.

In recent literature, the basic principles of 3D-printing sensors are already established. The most common and accessible technique of 3D-printing is Fused Deposition Modelling (FDM) [6, 10, 17], where the material is extruded from a nozzle and deposited in layers. The introduction of multi-material printing and conductive thermoplastic materials [18] made it possible to print a conductor and insulator in a single object, which is crucial for printing complete sensors [6]. Also direct ink writing (DIW) [19] and polyjetting [10, 20] can print multiple materials and could be suitable to 3D-print sensors.
Examples of 3D-printed force sensors include a flexible sensor capable of measuring the normal force [21] by measuring capacitance of a parallel plate capacitor. In a study in embedded sensors, Shemelya et al [22], designed a prototype capacitive sensor capable of measuring both normal and shear forces. Wolterink et al. designed and tested a shear force sensor for use on fingertips using piezoresistive gauges [8].
Furthermore, Mertodikromo et al [23] designed a capacitive sensor with a cylindrical layout for applications in shoe soles which is capable of measuring the shear forces acting a human foot. However, electronics parts of this design are not printed and therefore this design is harder to incorporate in a single 3D-printed object or shoe sole.

Overview

In this thesis, the requirements and objectives for the sensor will be set in Chapter 2. In Chapter 3, these requirements and objectives are used to select the most suitable printing and sensing technique. In Chapters 4 and 5, theoretical models are presented to describe the electrostatic and mechanical principles that are needed to understand the working principle of sensor designs. In Chapter 6, the theoretical models are used to find suitable sensor designs. The fabrication of the sensor is discussed in Chapter 7. Chapter 8, presents the experimental results of the sensor designs. The results are discussed in Chapter 9 and conclusions are drawn in Chapter 10, where also some suggestions for futher research are given.

2 Requirements and objectives

In this chapter, the requirements and objectives for the sensor are set. Using literature, it is determined which characteristics are crucial for effective use in the desired application and which aspects are important to optimize in the design process. The minimum requirements are described in Section 2.1. Next the objectives are presented in Section 2.2. The objectives in this section are weighted to make design choices in other chapters, this is elaborated in Section 2.3.

2.1 Requirements

In order to develop a shear stress sensor for application in the shoe sole of diabetic patients the following requirements should be met:

- **No increase in risk factors for ulcerations**
  The target group of persons with diabetes should not be exposed to increased risk factors for ulcerations, the technology should help reduce this risk. In particular the following aspect should be taken into consideration: there should be no bumps or other irregular shapes on the sensor surface. Some shear stress sensors use the rotation of a vertical beam or bumb to measure the shear stress [24,25]. As these irregular shapes can increase plantar pressures, which are a risk factor for development of DFUs, these sensing concepts are not suitable for this application.

- **Measurement range**
  The sensor should be able to measure shear stresses that act on the foot during everyday activities. Wang et al. [2] reviewed measurement results from current measurement systems. The highest peak shear stress on the human foot that is reported in literature is 135.3 kPa. Therefore, the sensor should be able to measure shear stress up to a pressure of at least 140 kPa.

2.2 Objectives

In this project, there are different objectives: various characteristics need to be optimized. The objectives are elaborated in the list below. The specific objectives are assigned a certain weight which indicates their importance in this project. The importance is described qualitatively in this section. The quantitative weights are determined using pairwise comparison and hierarchical weighing [26], which is further discussed in Section 2.3.

- **Accurately identify risk levels of shear stresses on the foot**
  Reducing the risk on DFUs can help to reduce health damage. For this goal, the following aspects play a role.

  - *Accuracy of peak-to-peak shear measurements (Weight: 20%)*
    As most existing measurement systems are not capable of measuring shear stresses [2], there is little understanding [27] of the exact effect of shear stresses on ulceration. Yavuz et al. [5] found that peak locations of shear stresses can predict to an extent the formation of DFUs. Furthermore, Hamatani et al. [28] found that shear peak-to-peak (p-p) measurements are a statistically significant predictor of callus formation for persons with diabetes. Callus formation in turn is a first stage in diabetic ulceration.

    The cited research indicates that peak shear values are a promising indicator for ulceration risk. As there are no clear thresholds established for acceptable stress levels [27], the peak measurements from the sensor should be relatively accurate to be able to assess the risk associated to these peak values for each patient.

To have an accurate measurement, the influence of other parameters such as humidity and temperature changes should be minimized. Furthermore, ideally the sensor should be insensitive to normal pressures, for which peak values up to 740 kPa are reported [2].

- *Accuracy of other (off-peak) measurements (Weight: 10%)*
  Most current research is focused on the peak values of shear and pressure measurements [1]. Other variables also have been suggested for use in the prevention of DFUs, for example Yavuz et al. [29] suggest that shear time integral values can be a better predictor for ulceration. For this reason and to improve the chances that the sensor can be used in other applications, the weight of this objective is still moderate.

- *Dimensions (Weight: 15%)*
  In the vertical direction, the sensor needs to fit in a sole beneath the foot. Therefore the sensor will need to be relatively thin.

  Also in the horizontal direction, dimensions need to be limited to prevent underestimation of the peak shear stress level: if the sensor is larger, the stress is integrated and averaged over a larger area, resulting in an underestimation of the peak level. For this reason the surface area of the sensor should not exceed 10 mm × 10 mm. Some researchers even argue that smaller areas are needed; Berki and Davis [30] advise to use sensors smaller than 4.8 mm × 4.8 mm instead. It is expected that the measured peak shear levels decrease [30] by about 10 to 17% if sensor area is increased from 4.8 mm × 4.8 mm to 10 mm × 10 mm.

  3D-printed sensors tend to be relatively large [11] compared to other production techniques (usually a few centimeters). Furthermore a smaller sensor generally results in smaller signals with similar noise and thus a smaller signal to noise ratio. For these reasons, no strict requirement is set. To prevent severe underestimation of the shear stress, it is important to limit the surface area of the sensor as much as possible. Some underestimation could be acceptable, especially for monitoring applications and if the underestimation is compensated by extra caution when using the measurement values.

- *Determination of the direction of stress (Weight: 3.75%)*
  There are two directions of shear: the anterior-posterior (AP) stress that is acting in the forward and backwards direction and the medio-lateral (ML) stress that is acting sideways. The stresses acting in the AP direction are substantially higher than in the ML direction [29]. Furthermore, the ML peak shear locations are around the pressure peak locations in most cases [31], and can thus be predicted more easily from other measurements than AP peak locations. For these reasons, the ML direction seems of less importance than the AP direction. This cannot be said without uncertainty, as most of the existing shear stress sensors are unidirectional [2] and thus measure only stresses in the AP direction.

  Although interesting for research, for the described monitoring application, two dimensional measurements are not strictly necessary for a meaningful result: a sensor that can only measure AP stresses or is insensitive to direction can still be sufficient to assess ulceration risks. Therefore, the weight of this objective is relatively low.

- *Number of sensors that can be interfaced (Weight: 3.75%)*
  Within a 3D-printed structure it might be challenging to connect a large number of sensors to a readout structure. This can be problematic if the goal is to identify risk areas. However, in this project the goal is to monitor shear stresses, probably at risk areas which can be known in advance. For example, almost half of DFUs (44.5%)

occur at the toes [32], most of them being the big toe. Alternatively, risk areas could be identified personally for each person using other methods. Therefore a smaller number of sensors might be capable of monitoring the most important area. This is the reason for a relatively low weight: although multiple sensors are necessary, there is no focus on maximizing the number of sensors (in this research).

- **Ease of use**
  The following objectives deal with the ease of use in daily life of users, which is especially relevant for monitoring applications.
  - *Durability (Weight: 11.25%)*
    The lifetime of the sensor should be sufficient to measure the stresses accurately during a longer period of time. For this reason, the sensor should be durable. Many existing solutions are not suitable to apply for a longer time in real-life environments [2]. Because this is one of the main goals of this sensor, the weight associated with this objective is relatively high.
  - *Simple readout (Weight: 8.75%)*
    The readout method should be simple enough such that the device needed for readout can be relatively small. Furthermore, the readout method should be energy efficient, as it should be able to run on a battery for a substantial amount of time.
  - *Cost (Weight: 5%)*
    As the cost of 3D-printing is relatively low compared to other manufacturing methods [6, 10] and health cost associated with DFUs are high [1], there is no major objective in limiting the cost of the technology in this project.
- **Practical application in clinical environments**
  Available systems are not commonly used in clinical environments [2]. This is mainly due to high cost, time consuming setup and lack of multidimensional measurements (most systems only measure pressure). Therefore, the following two objectives are considered:
  - *Ease of implementation (Weight: 13.75%)*
    To ensure that the design is practical for use by clinicians, the implementation of the sensor in a sole should be relatively easy. This means for example that manual placement of materials during construction should be avoided.
  - *Accessibility of production technology (Weight: 11.25%)*
    To be able to produce the sensors the manufacturing technique needs to be available for research in the current project and in a later stage also in clinical manufacturing processes. Some patients need to make use of customized shoe (in)soles, for example after amputation of toes or to reduce the stresses acting on their feet [12–14], therefore it is important that this can be part of the production processes.

2.3 Weighing of the objectives

The weights that are assigned to all objectives in Section 2.2 serve to be able to compare the importance of advantages and disadvantages of different alternatives. To arrive at these weights, the objectives are first ranked from most important to least important. This order is determined using pairwise weighing [26]: for each combination of objectives it is determined which of the two is most important. The comparison of all pairs can be seen in Appendix A, the final ranks are shown in Table 2.1.

With use of the ranks, the final weighing is assigned using hierarchical weighing [26]. First the weights on the three main objectives are set. Next, the sub-objectives are compared in their own category. The final weight is found by multiplying these weights of the different levels. These weights are assigned based on the knowledge gained in the preceding section (2.2),

Objective	***Rank***	***Weight in level***	***Weight***
Identify risk levels of shear stress		**50%**	
Accuracy of peak measurements	9	40%	20.00%
Accuracy of off-peak measurement	5	20%	10.00%
Determination of force direction	1	5%	2.5%
Number of sensors that can be interfaced	1	5%	2.5%
Dimensions	7	30%	15.00%
Ease of use		**25%**	
Durability	6	45%	11.25%
Simple readout	4	35%	8.75%
Cost	1	20%	5.00%
Implementability in medical environments		**25%**	
Ease of implementation	6	55%	13.75%
Accessability of techniques	5	45%	11.25%

Table 2.1: Objectives with their ranking and weights

where the importance is described qualitatively. In Table 2.1 the assigned weights are shown. The weights and ranks are color coded to see that the weights correspond well to the assigned ranks.

2.4 Conclusion: Research focus

With the discussion of the requirements and objectives, the main research focus of this project is determined. The main focus will be on the sensing requirements and objectives: Measurement range, accuracy of peak measurements and the sensor dimensions are the most crucial points of attention. Also the implementation and durability remain important in the design of the sensor.

3 Fundamental design choices

As a first step towards a final sensor design, the fundamental design choices are made. In this chapter, the printing method and the sensing principle will be selected. In order to come to an elaborated choice, various alternatives are described in Section 3.1 and 3.2. In Section 3.3 the final choice is made by weighing advantages and disadvantages against the objectives as discussed in Chapter 2.

3.1 Printing techniques

There exists a variety of techniques for Additive Manufacturing (AM) or 3D-printing. Most commonly, extrusion based methods are used. Alternatives include selective laser melting (SLM) [10] (where parts of layers of powder are solidified into an object using a laser), Laminated object manufacturing (LOM) [33] (the object is built up from sheets of material, which are cut using a laser or knives) and polyjetting [10] (where material is ejected from an inkjet nozzle. Again the object is built up from layers).

In the process of printing sensors, it is essential that multiple materials can be used in the same object [6]. For example, conductive and non-conductive parts or materials with different stiffness. For this reason, not all methods of 3D-printing are suitable to print sensors. Currently, extrusion based methods and polyjetting are the only methods commercially available that are capable of using multiple materials in a single print [19]. In the following subsections, the advantages and disadvantages of these methods are discussed.

3.1.1 Extrusion based methods

In the category of extrusion based methods, there are different printing methods that have the same basic principle [10, 33]: material is extruded by a nozzle, the object is formed with different layers of this material. The most common method is Fused Deposition Modelling (FDM) [10], in this method, a material (usually a thermoplastic) is heated to be deposited in liquid form. Advantages of FDM are that the technology has a relatively low cost [6] and that it is easy to make modifications to printing setups as the technology is open source and widely used [10]. There is a variety of materials available with various properties, such as conductive materials [6,18] and flexible materials [6,11]. In recent research [6], it was also shown to be possible to embed fibers in between layers. This can improve mechanical and electrical properties of the printed object. Disadvantages of FDM are quite low printing speed and the minimum feature size (in the order of 100 µm. In the z-direction, orthogonal to the layers, this can be slightly lower ($\approx 50\,\mu$m)) [33].

Direct Ink Writing (DIW) is a method where a viscous ink or paste is extruded [19]. After layers are placed, the object needs to solidify (for example by drying, using UV light or increased temperature). There is a large variety of materials available for DIW [6], it is even claimed to be the most versatile method in terms of material choice [19]. However, not all combinations of materials can be used [19], as the post-processing steps need to be compatible. An extra advantage for most sensor designs is that with DIW it is possible to achieve substantially lower electrical resistances compared to FDM [34]. The printing speed of DIW is comparable to FDM, and the minimum feature size can be slightly smaller (10 µm to 100 µm) [33].

It is also possible to combine FDM and DIW methods [34], resulting in an even wider choice of materials and combinations.

3.1.2 Polyjetting

In polyjetting [10], droplets of photosensitive material are ejected from nozzles and solidified using UV-light. Multiple materials and colors can be used at the same time. The method is substantially faster than extrusion-based methods [20]. Furthermore, the method also has a high resolution (10 µm) [33]. Disadvantages are that that the costs are relatively high [10] and that the method is less straightforward. Futhermore, because the material is solidified using UV-light, additional exposure to UV-light can make the material more brittle, resulting in a weaker or less durable object [10].

3.2 Sensing principles

There are different types of sensing principles that can be used. Two types of sensors are commonly used to make 3D-printed force sensors [6,35,36]; capacitive and (piezo)resistive sensors. Inductive techniques are quite common in sensors, but are hard to implement in printed sensors because of the limited conductivity of printing materials [6]. Therefore the piezoresistive and capacitive sensing techniques are elaborated upon in the following subsections.

3.2.1 Piezoresistive sensing

In piezoresistive sensing, the resistance of the material changes due to compression or stretching of the material. This partially occurs due to geometric changes [37] (e.g. change in cross-sectional area), however most of the effect is due to a change in the conductive path [6]: if the material is stretched the resistance in general increases. However, in printing materials this behaviour is non-linear [6]. Advantages are that the technology is quite simple to apply in force sensors (especially for normal forces). Also readout of the resistance is straightforward [38]. Furthermore piezoresistive sensing can result in a large sensing range [35], especially since the piezoresistive constants [6] of common conductors in 3D-printing are high.

For shear stress measurement, the application is less straightforward to apply, as stretching or compression is more obviously present in normal force (or pressure) measurements. Different techniques are used to measure shearing using piezoresistive effects. For example, Noda et al used a setup using cantilevers in elastic material (see Figure 3.1a). And Yin et al. [35] used a setup with two strain gauges to measure shear forces on robotic fingertips, see Figure 3.1b. Wolterink et al. [8] produced a 3D printed sensor using the same concept.
The main advantages of piezoresistive sensing are straightforward readout and a potentially large sensing range. The main disadvantages are non-linearities in the piezoresistive behaviour and the relatively complex and thick designs needed to measure shear stresses using this sensing technique.

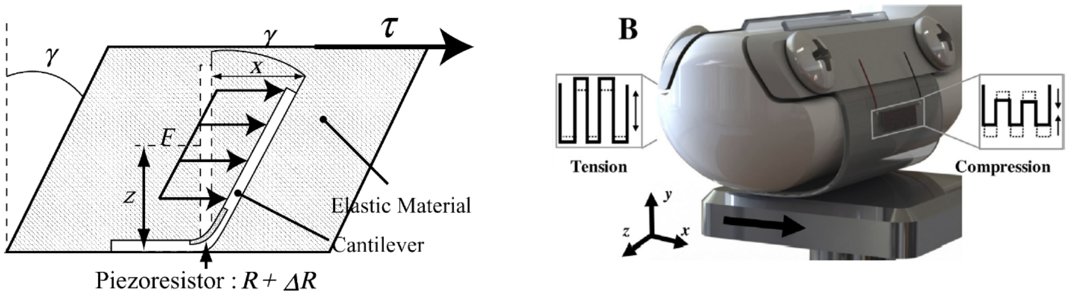

(a) Sensor design from Noda et al. [39] using cantilevers with piezoresistive material inside an elastic material.

(b) Sensor design from Yin et al. [35] where tension and compression from shearing are measured using piezoresistive gauges.

Figure 3.1: Examples of shear sensor designs using piezoresistivity

3.2.2 Capacitive sensing

In capacitive sensing, the capacitance between two plates (or other geometries) is changed by a displacement [37]. In many cases the distance between the plates is variable [21, 40], if a higher force is applied normal to the plates, the distance between plates decreases, causing an increased capacitance. When measuring shear forces another option is parallel to the applied force [41,42], such that the overlap in the plates causes a change in capacitance. This approach is quite natural to measure shear forces and has potential to be thinner than the piezoresistive concepts discussed earlier. Furthermore, capacitive sensing methods are insensitive to non-linearities in conductivities of the materials [6,38] and are more temperature independent [38]. The main disadvantage of capacitive sensing is that there can be electromagnetic interference [6, 35, 38], caused by nearby dielectrics or conductors. Also parasictic effects and, in case of sensing arrays, crosstalk [35] can influence the results. With proper shielding, the effects of these disadvantages can be reduced.

3.3 Design choices

The design choices between different alternatives are made using the objectives determined in Chapter 2. For the different objectives, a score is assigned to the alternative printing and sensing techniques. A 5-point scale [26] is used: ++ (excellent, 2 points), + (good, 1 point), o (satisfactory, 0 points), - (weak, -1 point), - - (inadequate, -2 points). The scores are multiplied with the weight of the objectives and summed to arrive at a utility value [26] for the alternatives. The alternative with the highest value is most promising in this project (based on the objectives).
Based upon the theory in section Section 3.1 and 3.2, the scores were assigned to different objectives, see Table 3.1 and 3.2. For some objectives there is no clear distinction between different techniques, in that case the row is left empty. From the resulting utility values, fused deposition modelling seems to be the most suitable printing technique. This is mainly due to the ease of implementation, especially in existing (in)sole models and the fact that the technology is already widespread and therefore more easily accessible.

Capacitive sensing was selected as sensing principle, the higher linearity and insensitivity to temperature make capacitive sensing more likely to result in accurate measurement values. A trade-off is made here as readout is in general harder for capacitive sensing, compared to piezoresistive sensing.

In both decisions, there is a substantial difference between the different alternatives, however for objectives with high weight a slight difference in scores is able to change the design choice. Especially the *accuracy of peak measurements* objective in the printing techniques choice and the *dimensions* objective in the sensing principle choice have a high weight and are relatively hard to assess in the early stage of the project. Further research might change the scores in favour of piezoresistive sensing and/or a combination of FDM and DIW printing methods.

3.4 Capacitive readout method

As capacitive sensing is chosen as the sensing method, also the way of readout needs to be chosen. There are various methods to determine the capacitance of a certain structure. One method is to measure the impedance of the capacitor at known frequencies. Another method is to find the oscillation frequency of an oscillator of which the capacitor is a part. This can also be extended to measure differentially, if both capacitors are part of the oscillator (e.g. the work by Brookhuis et al. [43]). There are existing solutions that are based on these concepts and output a digital signal, so called capacitance to digital converters (CDCs). As these solutions are already optimized and can compensate for unwanted effects such as temperature dependence of elements in the circuit, it is chosen to use an existing CDC. In this project the Analog Devices AD7747 [44] is used. In this CDC, the positive and negative electrode are excited using the same

Objective	***Weight***	***Fused Deposition Modelling (FDM)***	***Direct Ink Writing (DIW)***	***Combined FDM+DIW***	***Polyjetting***
Identify risk levels of shear stress					
Accuracy of peak measurements	20.00%				
Accuracy of off-peak measurement	10.00%				
Determination of force direction	2.5%				
No. of sensors that can be interfaced	2.5%	o	o	o	+
Dimensions	15.00%	-	o	o	++
Ease of use					
Durability	11.25%	o	o	o	-
Simple readout	8.75%				
Cost	5.00%	+	o	o	- -
Implementability in med. environments					
Ease of implementation	13.75%	++	+	++	o
Accessability of techniques	11.25%	+	-	-	- -
Score		***0.29***	***0.025***	***0.16***	***-0.11***

Table 3.1: Determination of the utility value for alternative printing techniques

Objective	***Weight***	***Piezoresistive***	***Capacitive***
Identify risk levels of shear stress			
Accuracy of peak measurements	20.00%	o	+
Accuracy of off-peak measurement	10.00%	o	+
Determination of force direction	3.75%		
No. of sensors that can be interfaced	3.75%		
Dimensions	15.00%		
Ease of use			
Durability	11.25%		
Simple readout	8.75%	+	-
Cost	5.00%		
Implementability in med. environments			
Ease of implementation	13.75%		
Accessability of techniques	11.25%		
Score		***0.09***	***0.21***

Table 3.2: Determination of the utility value for alternative printing techniques

signal, which makes the capacitance between these electrodes irrelevant. Active shielding can be used by applying this signal also on the shield. This device has a sampling frequency of up to 45.5 Hz and uses an excitation frequency of 16 kHz [44].

3.5 Conclusion

In this chapter, alternative printing and sensing methods were compared to make fundamental design choices. Based upon the weighted objectives from the preceding chapter, Fused Deposition Modelling was selected as a printing technique and it was chosen to use a capacitive sensing method. The choice was based upon literature and how advantages and disadvantages translate to potential sensor designs. In later modelling and experimental work that is discussed in the next chapters, it could be that there are sensor designs that have other (dis)advantages than were expected from the literature that was discussed in this chapter. Mainly the scores of the *accuracy of peak measurements* and *dimensions* objectives are relatively uncertain and can better be assessed with the knowledge from the next chapters.

4 Electrostatic modelling

In this section electrostatic analysis is used to develop methods to calculate the capacitance of printed structures. In Section 4.1, basic electrostatic theory is briefly introduced. In Section 4.2, the capacitance of structures consisting of infinitely long wires is analyzed analytically. The analytical expressions are implemented in MATLAB to numerically perform the last steps of the approach, which consist for a large part of the inversion of a (large) matrix. A Finite Element Method-based model is presented in Section 4.3 and compared to the approximation in Section 4.4. Plate and cylindrical layouts are discussed in Section 4.5.

4.1 Electrostatic theory and the parallel plate capacitor

In the following sections, different approaches will be studied to calculate the capacitance between conductive structures. In this section the basic concepts of capacitance and electrostatics are briefly introduced. As an example, the capacitance of the parallel plate capacitor is derived. (This well-known relation is used later in Section 4.5).

The electric field that is caused by electric charge is described by the Maxwell equations [45, 46]. For a static situation, where currents and charges vary relatively slow, the equations that describe the electric field are given by:

$$\nabla \cdot \vec{E} = \frac{\rho}{\epsilon_0} \tag{4.1a}$$

$$\nabla \times \vec{E} = -\frac{\partial \vec{B}}{\partial t} \approx 0 \tag{4.1b}$$

Where $\vec{E}$ is the electric field, $\vec{B}$ is the magnetic field, ρ is the charge density, ϵ_0 is the permittivity of vacuum (constant). In Equation (4.1b) the last approximation can be made because a static situation is considered.

Gauss' theorem can be used to rewrite Equation (4.1a) to a form that is especially useful to calculate the electric field in highly symmetrical situations, known as Gauss' law:

$$\oiint_S \vec{E} \cdot \vec{n} \mathrm{d}A = \frac{Q_{\text{inside}}}{\epsilon_0} \tag{4.2}$$

This equation is relating the electric flux trough a closed surface S to the charge enclosed by this surface.
An example of a symmetric situation where Equation (4.2) can be used is the electric field around an infinitely large charged sheet with surface charge density σ. As surface S, a block is used that is symmetrically positioned around an area A of the sheet. By symmetry, the electric field is directed perpendicular to the surface. Therefore, there is a uniform electric flux trough the surfaces of the block that are parallel to the plate. There is no flux trough the sides that are perpendicular to the sheet. The flux is thus $2A\left|\vec{E}\right|$. Thus, by Equation (4.2),

$$\left|\vec{E}\right| = \frac{Q}{2A\epsilon_0} = \frac{\sigma}{2\epsilon_0} \tag{4.3}$$

A useful property of the electric field is that the superposition principle applies. The field caused by one charge can simply be added by the field caused by another charge to find the total electric field. For example if an oppositely charged sheet is placed parallel to the original sheet, the fields can be added. In that case the field in between the plates is twice as large,

and the field outside is 0 (this can also be seen from Gauss' Law: as the plates are oppositely charged, the net charge is 0).
The electric potential ϕ, is the line integral of the electric field. As $\vec{E}$ is a conservative vector field, for static situations(Equation (4.1b)), this is path independent.
The potential difference between the two charged sheets is thus given by:

$$\Delta\phi = \int_{\text{plate1}}^{\text{plate2}} \vec{E} \cdot \mathrm{d}\vec{l} = \frac{\sigma S_{\text{plates}}}{\epsilon_0} \tag{4.4}$$

Where S_{plates} is the separation between the sheets.
The capacitance [45] between two oppositely charged conductors is given by:

$$C = \frac{Q}{\Delta\phi} \tag{4.5}$$

With substitution of Equation (4.4), the (well-known) equation for the capacitance between a parallel plate capacitor is obtained. As the derivation assumes that the plates are infinitely long, this is an approximation which can be used if the plate dimensions are much larger than the distance between the plates:

$$C = \frac{A\sigma}{\frac{\sigma S_{\text{plates}}}{\epsilon_0}} = \epsilon_0 \frac{A}{S_{\text{plates}}} \tag{4.6}$$

4.2 Capacitance of wire structures (Center-charge approximation)

As FDM printing forms an object by placing stripes of material (traxels) to form layers, conductive materials are initially wire-shaped. When printing full layers, these individual traxels more resemble rounded plates or beams, however the contact resistance [47] between the traxels is much higher than their bulk conductivity. As in that case most conductivity is in the center of the traxel, a wire could be a reasonable approximation. Therefore, calculating the capacitance between wire structures can form a basis for future designs. In this section, a method is presented which is used to approximate the capacitance between two structures consisting of a finite number of parallel wires. This approximation is referred to as the center-charge approximation, after its most crucial assumption.

4.2.1 Assumptions

To be able to compute these capacitances analytically, the following assumptions are made:

1. The wires are infinitely long.
2. The charge distribution on the surface is uniform. This means that for the electric field outside the wires, all charge on the wires is approximated by a line charge (λ) positioned at the center of each wire.
3. All wires have an equal, strictly positive diameter (d)

The first assumption is made to simplify the electric field from the individual wires, with this approximation it is possible to use Gauss' theorem and Equation (4.1a) to find the (well-known) expression for the electric field around an infinitely long line charge:

$$\vec{E} = \frac{\lambda}{2\pi\epsilon_0 |\vec{r}|} \frac{\vec{r}}{|\vec{r}|} \tag{4.7}$$

In this equation λ is the line charge, in coulomb per meter. $\vec{r}$ is the vector perpendicular to the line-charge and pointing from the line-charge to the point of interest. The magnitude of $\vec{E}$ is thus decreasing $\propto \frac{1}{|\vec{r}|}$, its direction is always radially outward (in case of a positive line charge).

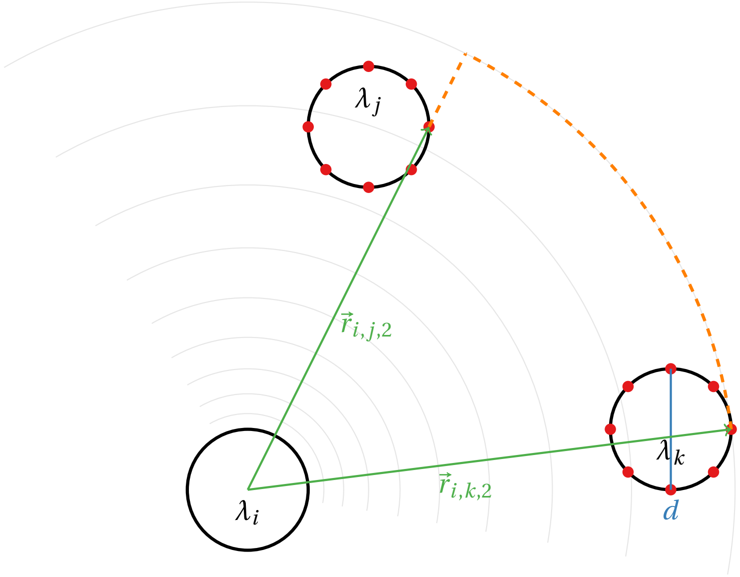

Figure 4.1: Sketch of a structure with three wires illustrating parameters for the contribution of wire i for the potential difference between wires j and k. The potential difference is found by integrating the electric field along the orange dashed path, which is partially along an equipotential line (shown in lightgray).

The second assumption is most crucial for the approximation, as it makes it possible to find the charge on all wires from their potential in an analytical manner. Finding a possible charge distribution from a potential field without this assumption makes calculations substantially more complex and is to the best of the authors knowledge not been done for non-specific configurations without the use of finite element models.

Note that there is no assumption that the wires are conductive: This is not compatible with the second assumption, as charges are not allowed to move inside the conductor. Therefore the surfaces of the metals are not necessarily equipotentials. The average potential of a number of points on the surface is used as the potential of the wires, which is further discussed in the derivation of the method in the next section. The influence of this assumption is estimated in Section 4.2.3.

4.2.2 Derivation of the approximation method

To find the potential difference between two wires, the superposition principle can be used: the contribution of each wire can be calculated separately and summed at the end. The first step is to calculate the contribution of an arbitrary wire to the potential difference between two wires. See Figure 4.1 for a general sketch. For the contribution of an arbitrary wire i to the potential difference between wire j and k, the electric field of wire i has to be integrated along a path from j to k:

$$\Delta\phi_{(1,2),i} = -\int_{\text{wire j}}^{\text{wire k}} \frac{\lambda_i}{2\pi\epsilon_0 |\vec{r}|} \frac{\vec{r}}{|\vec{r}|} \cdot \mathrm{d}\vec{l} \tag{4.8}$$

By integrating along a path that is radially outward from wire i and further only along equipotential lines (see the dashed orange line in 4.1). The integral in Equation (4.8) can then be written as:

$$\Delta\phi_{(j,k),i} = \frac{\lambda_i}{2\pi\epsilon_0} \ln\left(\frac{|\vec{r}_{i,j}|}{|\vec{r}_{i,k}|}\right) \tag{4.9}$$

where $\left|\vec{r}_{i,k}\right|$ is the distance from wire i to a point on the edge of wire k. In theory, the potential on (the surface of) an ideal conductor is homogeneous. However, the center charge approximation can cause the potential to be (slightly) inhomogeneous on the conductors. This is caused by the fact that the wires are not modelled as a conductor: the charge is not free to move but fixed in the center. Therefore, the end point of the integration on wires j and k should be chosen carefully. To minimize the effect of the choice of these integration bound-points, multiple points are used which are uniformly distributed on the surface of the conductors. The number of points at each conductor, n_p, is chosen to be 16, as a trade-off between accuracy and computation time. (In Figure 4.1 $n_\mathrm{p} = 8$ points are shown to illustrate this concept). To find the potential, the (non-weighted) average is used.

$$\Delta\phi_{(j,k),i} = \frac{\lambda_i}{2\pi\epsilon_0}\frac{1}{n_\mathrm{p}}\sum_{m=1}^{n_\mathrm{p}}\ln\left(\frac{\left|\vec{r}_{i,j,m}\right|}{\left|\vec{r}_{i,k,m}\right|}\right) \tag{4.10}$$

where $\vec{r}_{i,j,m}$ denotes the vector from the center of wire i to the m-th point on wire j.

In Equation (4.10), the potential difference caused by wire i has been expressed in terms of the line charge λ_i and constants depending on the geometry of the structure. Note that the potential difference $\phi_{(j,k),i}$ depends linearly on λ_i. Therefore, the elastance-length, which will be defined as $P_{(j,k),i} := \frac{\partial\phi_{(j,k),i}}{\partial\lambda_i}$ and has units meter per Farad ($\mathrm{m\,F^{-1}}$), can be written as:

$$P_{(j,k),i} = \frac{\Delta\phi_{(j,k)}}{\lambda_i} = \frac{1}{2\pi\epsilon_0}\frac{1}{n_\mathrm{p}}\sum_{m=1}^{n_\mathrm{p}}\ln\left(\frac{\left|\vec{r}_{i,j,m}\right|}{\left|\vec{r}_{i,k,m}\right|}\right) \tag{4.11}$$

As wire i is an arbitrary wire, Equation (4.11) can be used for all other wires in the structure, this includes wires j and k as well. The potential difference between wires j and k can be found by summing the contribution of all individual wires (by the superposition principle):

$$\Delta\phi_{(j,k)} = \sum_{i=1}^{n}\Delta\phi_{(j,k),i} = \sum_{i=1}^{n}P_{(j,k),i}\lambda_i \tag{4.12}$$

The same approach can be taken to find the potential between any other pair of wires. As $\Delta\phi_{(j,k),i}$ is linear in λ_i, this results in a system of linear equations. For a structure of n wires, there are $n-1$ independent voltage differences. However, there are n values of λ_i, which are (usually) unknown. In order to solve for the values of λ_i, an n-th independent equation is needed. It would be natural to make a last equation for the potential difference between one of the wires and infinity, as usually ϕ is defined to be zero at infinity. However, in this case, the assumption is made that the wires are infinitely long. This causes a problem as the electric field will now decrease $\propto 1/\left|\vec{r}\right|$, meaning that the potential will go towards $\pm\infty$ as $\left|\vec{r}\right| \to \infty$. This problem can be evaded by letting the total charge be equal to zero. This makes sure that the potential at infinity tends to zero, however the freedom of choosing an offset for the potential of the wire structure is lost. As the potential difference between the wires can still be set, there is still enough freedom to find the capacitance of the structure. Therefore, the last equation that is used in the system of equations is:

$$\sum_{i=1}^{n}\lambda_i = 0 \tag{4.13}$$

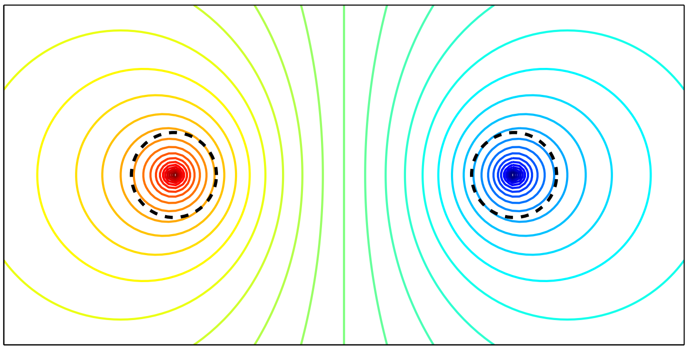

Figure 4.2: Estimation of the equipotential lines of wires (shown in dashed black), using the center line charge approximation

The system of equations in matrix form can be written as:

$$\begin{bmatrix} P_{(1,2),1} & \cdots & P_{(1,2),n} \\ \vdots & \ddots & \vdots \\ P_{((n-1),n),1} & \cdots & P_{((n-1),n),n} \\ 1 & \cdots & 1 \end{bmatrix} \begin{bmatrix} \lambda_1 \\ \vdots \\ \lambda_n \end{bmatrix} = \begin{bmatrix} \Delta\phi_{(1,2)} \\ \vdots \\ \Delta\phi_{((n-1),n)} \\ 0 \end{bmatrix} \tag{4.14}$$

If all wires are at different locations, the elastance matrix (on the left of equation 4.14) is invertible, as all rows are linearly independent. In that case, both sides can be left-multiplied with this inverse to find the charge on all wires from the potential differences [48]. With that, the capacitiance per length C/L between two oppositely charged structures (consisting of multiple wires) can be found by summing all charges in one of the structures:

$$\frac{C}{L} = \frac{\sum\limits_{i\in \text{ struct. } 1} \lambda_i}{\phi_{\text{struct.2}} - \phi_{\text{struct.1}}} \left(= \frac{\sum\limits_{i\in \text{ struct. } 2} \lambda_i}{\phi_{\text{struct.1}} - \phi_{\text{struct.2}}} \right) \tag{4.15}$$

As computational complexity increases rapidly with the addition of more wires, especially the inversion of the matrix in Equation (4.14), the approach above was implemented in MATLAB-functions.

4.2.3 Two wire approximation error

For a case with two wires, it is possible to analyze the error that is made with the center-charge approximation. To do that, the potential field of two line charges is calculated, the result is shown in Figure 4.2. It can be seen that the wires (in black) are not exactly on an equipotential, which would be the case for perfect conductors. However, the equipotential lines of the two oppositely charged wires do look like circles, suggesting that it would be possible to exactly describe the electric field of two infinitely long wires using two line charges. Indeed, it can be shown that this is the case: two oppositely charged wires that are centered at $x = \pm\frac{S}{2}$ with diameter d produce the same potential field as two line charges located at $x = \pm b$, where $b = \frac{1}{2}\sqrt{S^2 - d^2}$ (see Figure 4.3). This result is proven in Appendix B. The potential can be written as the superposition of the potential fields of the two individual line charges:

$$\phi = \phi_+ + \phi_- = \frac{\lambda}{2\pi\epsilon_0} \ln \frac{|r_-|}{|r_+|} + K \tag{4.16}$$

where K is an integration constant. The potential difference can be found by evaluating equation Equation (4.16) at any point on the boundary of the two wires. Note that this is not an

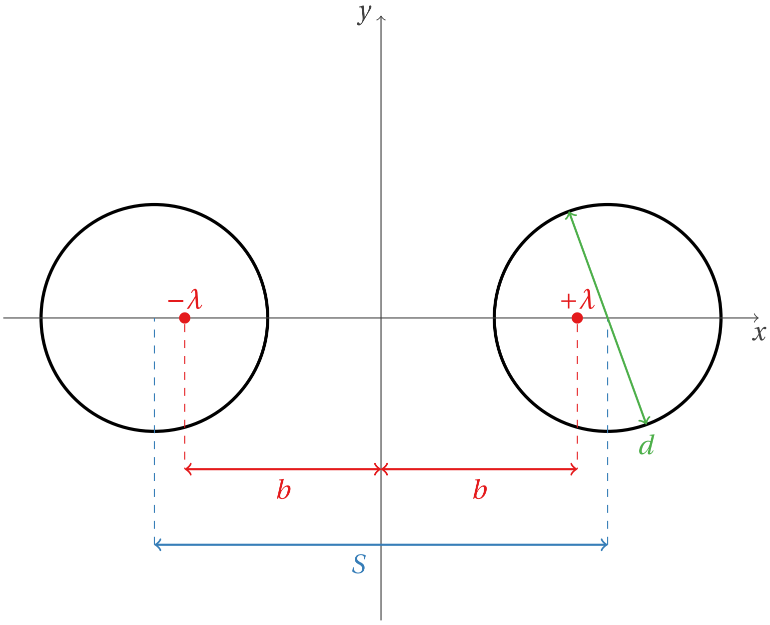

Figure 4.3: Sketch of two wires and two line charges, with relevant parameters

approximation (in contrast to the case in Section 4.2.2), as the boundaries of the wires are equipotentials. If on each wire the point on the x-axis closest to the y-axis is used, the potential difference can be written as follows:

$$\begin{aligned}\Delta\phi &= \frac{\lambda}{2\pi\epsilon_0}\left(\ln\left(\frac{b+1/2(S-d)}{b-1/2(S-d)}\right)-\ln\left(\frac{b-1/2(S-d)}{b+1/2(S-d)}\right)\right)\\ &= \frac{\lambda}{\pi\epsilon_0}\ln\left(\frac{\sqrt{S^2-d^2}+(S-d)}{\sqrt{S^2-d^2}-(S-d)}\right)\end{aligned} \tag{4.17}$$

To find the capacitance per unit length, the definition of capacitance can be used to find:

$$\frac{C}{L}=\frac{\lambda}{\Delta\phi}=\frac{\pi\epsilon_0}{\ln\left(\frac{\sqrt{S^2-d^2}+(S-d)}{\sqrt{S^2-d^2}-(S-d)}\right)} \tag{4.18}$$

This corresponds to the expression that is derived by Green [49], found using a slightly different approach. Additionally, Green [49] shows that that Equation (4.18) can be rewritten to a simpeler form:

$$\frac{C}{L}=\frac{\lambda}{\Delta\phi}=\frac{\pi\epsilon_0}{\cosh^{-1}\left(\frac{S}{d}\right)} \tag{4.19}$$

With this analytical expression for the capacitance, the error that is made in the center-wire approximation can be evaluated. From Equation (4.19), it can be noted that scaling all in-plane dimensions (separations S and the diameter) by a certain factor does not change the capacitance, because the $\frac{S}{d}$-ratio remains equal. The capacitance of the center-wire approximation and the analytical expression are therefore compared for different $\frac{S}{d}$-ratios. The result can be seen in figure Figure 4.4. For $\frac{S}{d} > 2$ the approximation error is less than 5%. This is relatively close, since S is defined from center to center ($\frac{S}{d} = 2$ is the situation where there can exactly fit one wire with the same diameter in between the two wires).

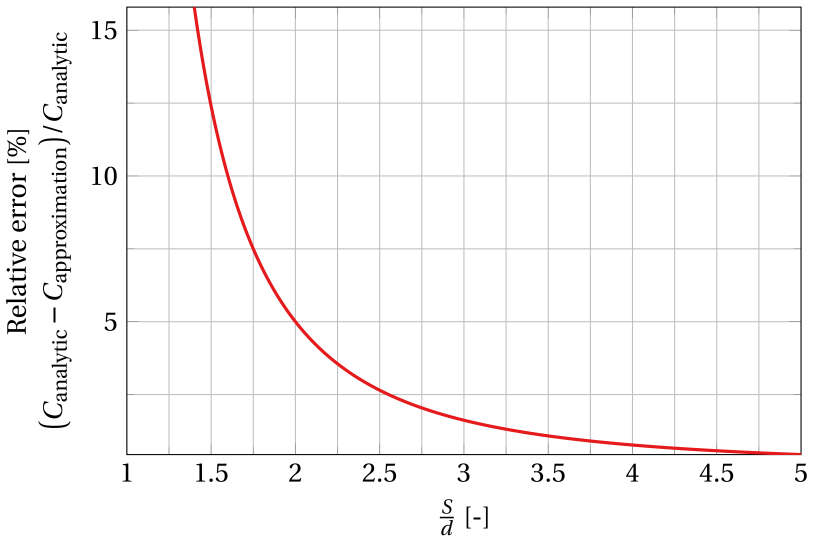

Figure 4.4: Comparison between analytic and approximated capacitance between two wires with opposite potential

4.3 Capacitance of wire structures using Finite Element Methods (FEM)

In Section 4.2, an analytical approximation is derived for the capacitance between wire structures. The comparison with analytical solutions for structures of two wires are promising, but in order to confirm results of more complex structures a Finite Element Method (FEM) approach is developed in this section. The simulations are performed using COMSOL-Multiphysics (version 5.4).

4.3.1 FEM models

To find the capacitance of wire structures two model variants are used, which only differ in their definition of the geometry. The first model uses a two-dimensional geometry, which is used to find the capacitance between infinitely long wires. This model can be used to verify the approximations. A three-dimensional model includes the length of the wires in the longitudinal direction (L) and can be used to check the capacitance of physically realizable structures. The differences between the models are only minor and indicated using square brackets.

The geometries consist of disks [cylindrical] wires that have material properties of copper. These material properties do not influence the result as the wires act as perfect conductors because only steady state is simulated. The wires are contained in a sufficiently large rectangle [cuboid] of air. Only electrostatic physics are used in the models, together with a stationary source sweep study. This study is suitable to find the capacitance of multiple structures [50]: it applies voltage to only one terminal at a time.

The following boundary conditions are used:

- All conductors with equal potential are assigned a terminal boundary condition.
- One of the terminal boundary conditions is replaced with a ground boundary condition. Capacitances are calculated with respect to this electrode.
- Remaining volumes have a constant charge boundary condition.
- Boundaries of the rectangle [cuboid] are assigned a zero charge boundary condition. If the rectangle [cuboid] is large enough it should not make a difference for the capacitance which boundary condition is applied here.

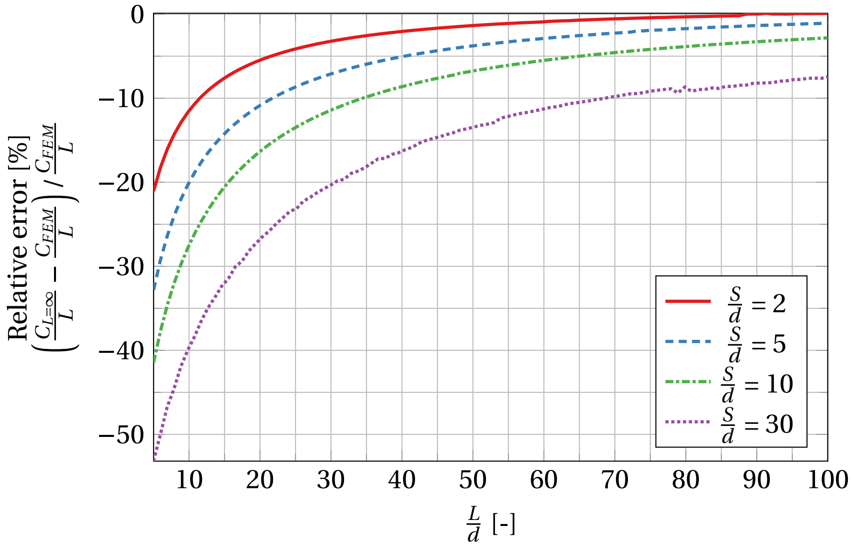

Figure 4.5: Influence of the length on the capacitance between two wires, for different separations (S)

The evaluation of the capacitance depends on the number of structures (or terminal boundary conditions). For more than two structures the mutual capacitance matrix is evaluated. With two structures (one terminal), this matrix is not defined in COMSOL, therefore the (Maxwell) capacitance is evaluated in that case.

The mesh and the size of the rectangle [cuboid] should not influence the resulting capacitance of a wire structure. To verify this, the fineness of the mesh is increased one level or the rectangle [cuboid] is made 10% larger in each direction. The simulation is repeated and compared to the original simulation. The error is considered acceptable if the difference between the simulations is less than 1%. The influence of the mesh and size will be checked again for every new use of the model. When sweeping parameters at least the bounds of the sweep are checked together with a few points in the sweeping range. This is done to reduce the computation time.

4.3.2 Automization using COMSOL LiveLink for MATLAB

To be able to compare the FEM results to other results (for example from Section 4.2), COMSOL LiveLink for MATLAB is used to be able to create and simulate COMSOL models from MATLAB scripts and functions. For each calculation a new model is created, all steps from the previous section are applied and the model is simulated. For approximately 5% of models the mesh generation gives an error at the first try. In these cases the MATLAB-script slightly adjust the mesh generation parameters to try the simulation again (which is advised in the manual [51]). The MATLAB function that is used to perform these simulations is attached in Appendix C.2.

4.4 Influence of finite length

With the FEM-model presented in Section 4.3, the influence of the length of the wires (L) on the capacitance can be analyzed. This is done by comparing the expected capacitance per length of the infinite length wire and the FEM simulation for a finite length wire. In Figure 4.5, the relative difference between these capacitances is shown for a situation with two wires. The error is smaller for smaller separations and larger lengths.

4.5 Other conductive layouts

In previous sections much attention was put on models to find the capacitance of wire structures. There are also other structures that could potentially be useful in certain shear stress sensor designs.

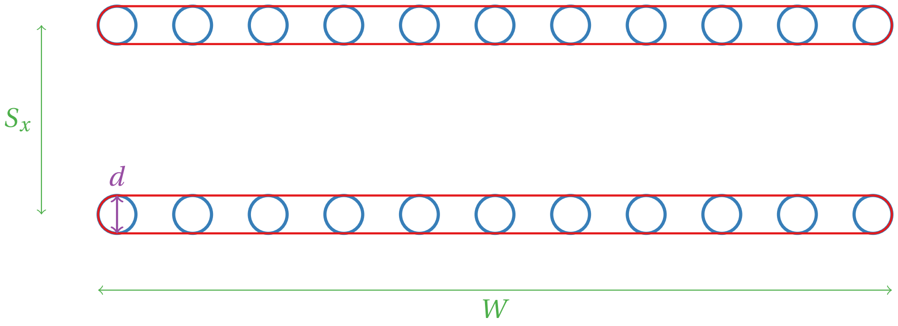

Figure 4.6: Sketch of a parallel rounded plate structure (the outline shown in red) and a corresponding wire structure approximation (circles in blue).

4.5.1 Plate layouts

Instead of using wire structures, parallel plates can be used. The capacitance can vary due to changes in distance between the plates or due to a changing overlap between the plates. The last option is most straightforward for measuring shear force.

In theory, a parallel plate capacitor could be modelled by having a wire structure with no separation between the wires. To see if this is indeed the case, the results from the center-charge approximation and the FEM model are compared to the expected parallel plate capacitance with equally wide plates. The capacitance of wide plates is found using the infinite plate approximation Equation (4.6) and using FEM for an rounded plate (see Figure 4.6) that is infinitely long in one direction. The cross-section of the different structures is shown in Figure 4.6. This is done for multiple (approximate) widths of the structures. The widths are approximate as there is an integer number of wires with a set density. The results are shown in Figure 4.7 below. The jumps that are visible for smaller widths are caused by changes in the number of wires. The results indicate that for a high density, the capacitance converges to some value. This value can be higher than the capacitance expected for plates, because the wire structure models the fringe fields outside the capacitor plates (in one direction for infinitely long wires). Comparing the approximation to the FEM wire simulation, it can be observed that the error at a wire density of 0.5 (which corresponds to a separation of $2d$) again results in an error of around 5%. This corresponds to the results from Section 4.2.3, that also show a 5% error at a separation-diameter ratio of 2. This value is also within 10% of the capacitance for a wire density of 100%. The deviation between the wire structures and the FEM plate structure is below 15 % for the depicted values. Especially for structures with a small width (certainly for $\frac{W}{d} \leq 40$), the wire-approximation is valuable to approximate the capacitance between plates as the deviation between the wire approximation and the FEM-plate result is substantially lower than the deviation between the infinite plate approximation and the FEM-plate result.

4.5.2 Cylindrical layouts

[t!] Another option for the layout of the electrodes is to use a cylindrical layout, where one (ground) electrode is placed in the center of a cylinder. The cylinder can be segmented into different parts. The capacitance of the segments with the ground electrode can be used to find the displacement and direction of the deformation. This method is used in the design of a half-printed sensor for application in shoe soles developed by Mertodikromo et al. [23]. The electrostatic analysis (including FEM simulations) is already presented in their work, together with experimental results. A sketch of the design is shown in Figure 4.8. The sensor design has a surface area of $3\,\mathrm{cm}^2$ and a thickness of 3.6 mm. The main results are that the sensor has a measurement range > 80 kPa and a predicted sensitivity of $0.012\,\mathrm{pF\,N^{-1}}$ which is experimentally found to be $0.0006\,\mathrm{pF\,N^{-1}}$ [23].

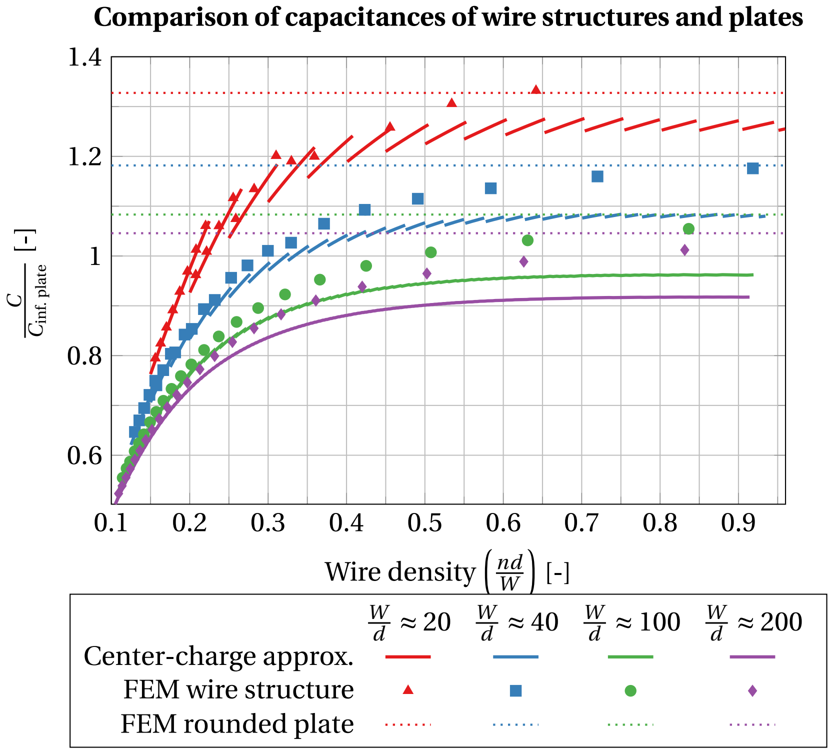

Figure 4.7: Capacitance of wide wire structures (with $\frac{S_x}{d} = 5$) relative to the equivalent parallel plate capacitance (Equation (4.6)) (For readers in grayscale: Legend order is from top to bottom)

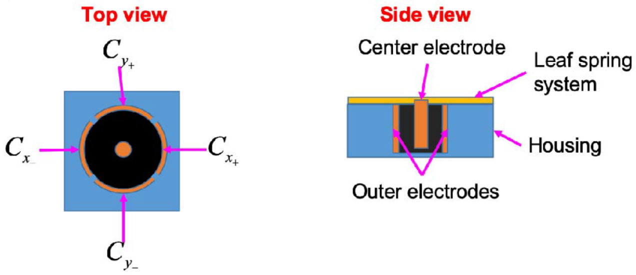

Figure 4.8: Sketch of the cylindrical layout used in the sensor developed by Mertodikromo et al. [23] (Image from the cited work)

One of the main advantages of a cylindrical layout is that it is suitable to measure the direction of the force. As this is not a priority objective of the sensor (see Section 2.2), and a half-printed sensor for this application is already developed using this technique, this work will not use a cylindrical layout. The work of Mertodikromo et al. [23] can instead be used as a comparison of other sensor designs.

4.6 Conclusion

In this chapter, various models have been presented to calculate the capacitance between conductive structures. Most attention was put in the capacitance between wire structures, which are likely to resemble the conductive behaviour of structures of traxels printed by a 3D-printer. An approximation was made to be able to perform capacitance calculations relatively quickly. For verification, a FEM analysis is perfomed. The deviation between the approximation and the FEM analysis is below 5% for $\frac{S}{d}$-ratios above 2. This means that the center-wire approximation can be used with a 5% error margin if the distance between two wires is at least one diameter. Plate structures can be approximated by dense wire structures relatively well, no deviations larger than 15% were found in the studied ranges (see Figure 4.7) with wire densities of 50% or larger. Especially for plates with a small width, this approximation is more accurate than the approximation by the capacitance of infinite plates, as the center-wire approximation model includes the effect of the fringe fields.

5 Mechanical modelling

In this section relevant mechanical concepts and models for the design of the shear force sensor will be discussed. The goal is to present the theoretical knowledge that is necessary to design the mechanical part of the sensor in the next chapter. In Section 5.1, the most basic alternative is discussed: a shear force acting on a linear bulk elastic material. Also the definitions of shear modulus, Young's modulus and Poisson ratio are reiterated in this section. In Section 5.2, a linear beam model is used to derive the deformation of beam structures. To model the behaviour of printed plastics more accurately, hyperelastic material theory is introduced in Section 5.3. This theory is used in an hyperelastic beam model and Finite Element Method simulations in Section 5.4 and 5.5 respectively. The comparison of different beam models and the effects of assumptions are presented in Section 5.6

5.1 Shear forces on linear bulk materials

The displacement of a bulk material due to a shear stress τ can often be related linearly by the shear modulus G [52], for the parameters in Figure 5.1:

$$G = \frac{\tau}{\gamma} = \frac{\tau}{\tan^{-1}(\Delta y/S)} \tag{5.1}$$

This relation can be used for materials that are isotropic and homogeneous and that show linear elastic deformation [52].

Note that the definition of the shear modulus is similar to the Young's modulus E that relates the linear shear σ and strain ϵ [52]:

$$E = \frac{\sigma}{\epsilon} \tag{5.2}$$

The similarity between the Young's and shear modulus suggest that they are related. This is indeed the case, G can be expressed in terms of E and the Poisson's ratio (ν), which describes the compressability of a material: if a material is streched in the longitudial direction (ϵ_{long}), there can be contraction in the lateral direction (ϵ_{lat}). The Poisson' ratio is defined as:

$$\nu = -\frac{\epsilon_{\text{lat}}}{\epsilon_{\text{long}}} \tag{5.3}$$

An incompressible material (where volume remains constant) has a Poisson's ratio of 0.5 [53]. This is because in that case the volumetric strain is zero: $\epsilon_{\text{vol}} = \epsilon_{\text{long}} + 2\epsilon_{\text{lat}} = (1-2\nu)\epsilon_{\text{long}} = 0$. The Poisson's ratio and Young's modulus are especially useful to obtain a value for the shear modulus G, which is often not reported in datasheets for (3D-printed) materials. This relation is [53]:

$$G = \frac{E}{2(1+\nu)} \tag{5.4}$$

For common printing materials the material properties that are discussed in this section are shown in Table 5.1.

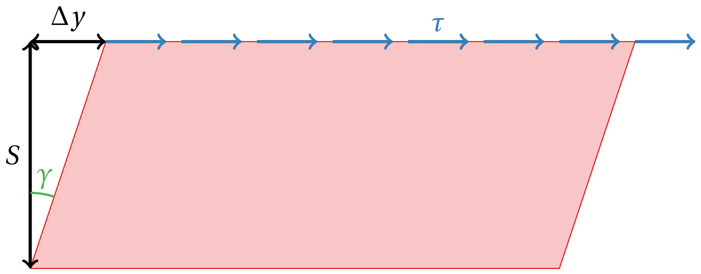

Figure 5.1: A shear stress τ acting on a bulk material, with relevant parameters

Material	Young's modulus	Yield strength	Poisson's ratio	Shear modulus
PLA	2.38 GPa [54–56][a]	58 MPa [54–56][a]	0–0.5[b]	0.8–1.2 GPa[b,c]
ABS	2 GPa [57]	30 MPa [57]	0.37 [57]	70 MPa [57]
PET	1.9 GPa [58]		0–0.5[b]	0.63–0.95 GPa[b,c]
TPU: NinjaFlex	12 MPa [59]	4 MPa [59]	0.48 – 0.5 [60][d]	4 MPa[c]
TPU: SemiFlex	25 MPa [61]	9 MPa [61]	0.48 – 0.5 [60][d]	8 MPa[c]
TPU: Armadillo	396 MPa [62]	27 MPa [62]	0.48 – 0.5 [60][d]	132 MPa[c]

[a] Mean value of the three cited sources.

[b] Based upon the limits of Poisson's ratio.

[c] Calculated from Young's modulus and Poisson's ratio using Equation (5.1)

[d] Value for generic TPUs (thermoplastic polyurethanes).

Table 5.1: Material properties for common materials in FDM 3D-printing

5.2 Linear beam theory

Compared to bulk material as shown in Figure 5.1 a more flexible structure can be obtained using a structure with beams. To have a first estimate of the movement of such a structure (like in Figure 5.2a), linear beam theory is applied. This means that the deformation is assumed to be elastic and that the stress-strain behaviour of the material is linear. The study concentrates on a single beam, but appropriate boundary conditions are used to be able to use these results for structures of multiple beams.

5.2.1 Timoshenko beam theory

In Timoshenko's beam theory, the key assumption that is made is that the cross-sections of the beam remain plane and do not deform. In contrast to the Euler-Bernoulli assumption, the cross-sections are not assumed to be perpendicular to the neutral line, instead the angle between the normal of the cross-section and the neutral line is θ. This makes the theory suitable to analyze somewhat thicker beams. Still the theory is limited to small strains. According to the theory, the elastic behaviour of a beam can be described by the following coupled differential equations [63].

$$\frac{\partial \theta(x)}{\partial x} = -\frac{M(x)}{EI} \tag{5.5a}$$

$$\frac{\partial v(x)}{\partial x} = \frac{F_\mathrm{s}(x)}{\kappa G A_\mathrm{c}} - \theta(x) \tag{5.5b}$$

Where $M(x)$ is the bending moment, $F_\mathrm{s}(x)$ is the internal shear force, v is the displacement in y-direction, A_c is the cross-sectional area, and I is the second moment of area. For the rectangular cross-section I is given by $I = \frac{1}{12}H^3L$. Here L denotes the length of the beams in the z-direction in Figure 5.2b. κ in equation Equation (5.5) is the shear coefficient, for a rectangular cross-section, κ can be estimated by $\kappa = \frac{10(1+\nu)}{12+11\nu}$ [64]. Thus, for an incompressible beam $\kappa = \frac{6}{7}$.

5.2.2 Deformation of the beam

As boundary conditions, at $x = 0$, it is assumed that the beam is fully fixed to a bottom structure, so $u = v = \theta = 0$. At $x = S_\mathrm{b}$, a shear force Q is applied. If many similar beams are connected in parallel as in Figure 5.2a, the beams rotation can be assumed to be fixed: $\theta(S_\mathrm{b}) = 0$. With these boundary conditions Equation (5.5) can be solved:

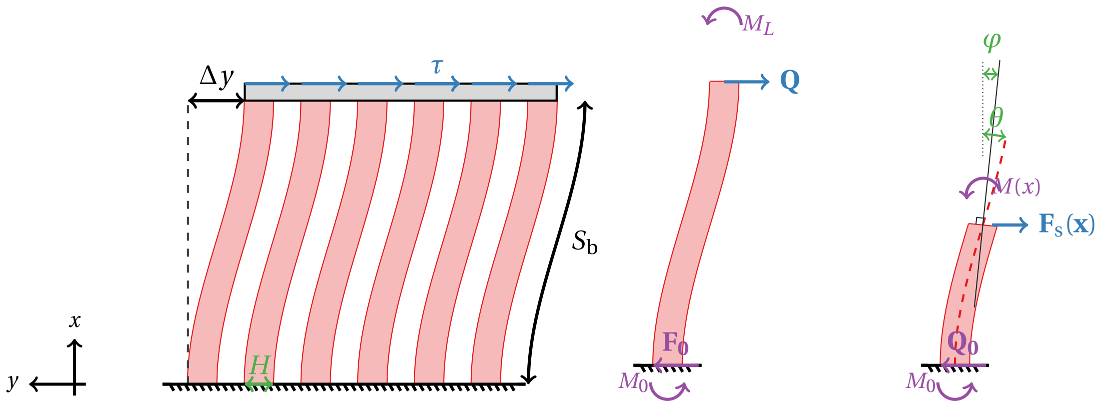

(a) A shear stress τ acting on a beam structure, with relevant parameters

(b) Reaction loads caused by a shear force on a beam with fixed rotation at $x = S_b$

(c) Reaction- and internal loads in a Timoshenko beam

Figure 5.2: Sketches of beam structures, with parameters.

The internal bending moment and shear force are given by:

$$\begin{aligned} M(x) &= xF + M_0 \\ F_s(x) &= F_0 = Q \end{aligned} \tag{5.6}$$

Substitution in Equation (5.5a) and integration gives:

$$\theta(x) = -\frac{Qx^2 - 2M_0x}{2EI} + \theta(0) \tag{5.7}$$

Substitution of I and boundary conditions gives:

$$\begin{aligned} M_0 &= \frac{QS_b}{2} \\ \theta(x) &= -\frac{Q}{2}\frac{(x^2 - xS_b)}{EI} = -6Q\frac{(x^2 - xS_b)}{EH^3L} \end{aligned} \tag{5.8}$$

Substitution and integration of Equation (5.5b) results in an equation describing the displacement of the beam:

$$\begin{aligned} v(x) &= \frac{Q}{\kappa GA}x + \frac{Q}{H^3LE}\left(2x^3 - 3x^2S_b\right) + v(0) \\ v(S_b) &= \frac{QS_b}{\kappa GHL} - \frac{QS_b^3}{H^3LE} \end{aligned} \tag{5.9}$$

5.3 Hyperelastic material models

In order to be able to describe the movement of the beam more accurately for larger strains, the non-linear stress-strain behaviour should be described. In this section, a hyperelastic material model will be used. These kind of models are suitable to describe the behaviour of rubber-like, polymeric materials [65], such as the thermoplastic polyurethane (TPU) printing materials in Table 5.1.

Numerous descriptions can be used to describe the behaviour of hyperelastic materials [66]. One of the earliest and simpelest descriptions is the Neo-Hookean model. Other examples are the Mooney-Rivlin model and the Ogden model. Reppel and Weinberg [67] compared these three models to the experimental behaviour for printed Ninjaflex TPU. It was concluded that the Neo-Hookean model matched the experiments for strains up to 70%. For the Mooney-Rivlin model this was 450%. As no strains larger than 70% are expected in the sensor, the Neo-Hookean model was chosen to be used. An additional advantage of this model is that fewer material parameters are needed in this model. For incompressible materials, only the initial shear modulus (μ) is needed to describe the elastic behaviour. This parameter can be derived from the number of polymer chains in the material [65], but should also correspond to the shear modulus G to match small strain behaviour. Therefore, the parameters for the shear modulus from table Table 5.1 can be used for the initial shear modulus.

5.4 Hyperelastic beam model

In this section, a beam model for hyperelastic materials will be presented and applied to solve the deformation of beam structures like in Figure 5.2. The beam model developed by He et al. [68] will be used. This model uses a Neo-Hookean material model and is of the Timoshenko-type, meaning that the angle of the normal of the deformed cross-sections φ is not necessarily equal to the angle of the midplane of the beam θ (see figure Figure 5.2c). The difference between these angles is the shear angle, which will be denoted by α. Because this shear is taken into account in the model, the model is suitable to apply for relatively thick beams. In contrast to the Timoshenko model proposed in Section 5.2, the deformation of the cross-section is taken in account, to the extent that the cross-sections are still planar, but the thickness of the beam can vary depending on the stresses on the material. With this, the incompressibility is modelled. This thickness stretching effect is only taken into account for one direction. The length of the beam in the z-direction of Figure 5.2 is assumed to remain constant.

With these assumptions, He et al. [68] derived the following expressions for the equilibrium of beams:

$$\left(\lambda\cos\theta - \left(\frac{1}{\lambda^3\cos^3\alpha} + \frac{(\varphi')^2H^2}{\lambda^7\cos^7\alpha}\right)\cos\varphi\right)' + \frac{p}{\mu A_\mathrm{c}} = 0 \tag{5.10a}$$

$$\left(\lambda\sin\theta - \left(\frac{1}{\lambda^3\cos^3\alpha} + \frac{(\varphi')^2H^2}{\lambda^7\cos^7\alpha}\right)\sin\varphi\right)' + \frac{q}{\mu A_\mathrm{c}} = 0 \tag{5.10b}$$

$$\left(\frac{1}{3}\frac{(\varphi')^2H}{\lambda^6\cos^6\alpha}\right)' - \tan\alpha\left(\frac{1}{\lambda^2\cos^2\alpha} + \frac{(\varphi')^2H^2}{\lambda^6\cos^6\alpha}\right) + \frac{m}{\mu A_\mathrm{c}} = 0 \tag{5.10c}$$

A prime ($'$) denotes a derivative with respect to x. x is not explicitly part of Equation (5.10), but λ, θ, φ, α, p, q and m can depend on x. p, q and m denote the distributed horizontal force, vertical force and bending moment per unit length respectively, and λ is the stretch of the midplane element, which can be written in terms of the x and y-deformation of the midplane, u_0 and v_0 respectively:

$$\lambda = \sqrt{(1+u_0')^2 + v_0'} \tag{5.11}$$

5.4.1 Deformation of the beam

To solve for the equilibrium of the beam depicted in Figure 5.2, the following boundary conditions are applied to the system of differential equations in Equation (5.10):

- At $x = 0$, $u_0 = v_0 = \varphi = 0$.
- At $x = S_\mathrm{b}$, the applied force in negative x and y direction are P and Q respectively and $\varphi = 0$

With this, equation Equations (5.10a) and (5.10b) can be integrated and rewritten as follows:

$$\lambda\cos\theta\cos\varphi - \left(\frac{1}{\lambda^3\cos^3\alpha} + \frac{(\varphi')^2H^2}{\lambda^7\cos^7\alpha}\right)\cos^2\varphi = -\frac{P\cos\varphi}{\mu A_\text{c}} \tag{5.12a}$$

$$\lambda\sin\theta\sin\varphi - \left(\frac{1}{\lambda^3\cos^3\alpha} + \frac{(\varphi')^2H^2}{\lambda^7\cos^7\alpha}\right)\sin^2\varphi = -\frac{Q\sin\varphi}{\mu A_\text{c}} \tag{5.12b}$$

Addition of (a) and (b) gives, with the use of trigonometric identities and the fact that $\alpha = \theta - \varphi$:

$$\lambda\cos\alpha - \left(\frac{1}{\lambda^3\cos^3\alpha} + \frac{(\varphi')^2H^2}{\lambda^7\cos^7\alpha}\right) = -\frac{Q\sin\varphi + P\cos\varphi}{\mu A_\text{c}} \tag{5.13}$$

Similarly, equation Equations (5.10a) and (5.10b) can also be rewritten as:

$$\lambda\cos\theta\sin\varphi - \left(\frac{1}{\lambda^3\cos^3\alpha} + \frac{(\varphi')^2H^2}{\lambda^7\cos^7\alpha}\right)\cos\varphi\sin\varphi = -\frac{P\sin\varphi}{\mu A_\text{c}} \tag{5.14a}$$

$$\lambda\cos\theta\sin\varphi - \left(\frac{1}{\lambda^3\cos^3\alpha} + \frac{(\varphi')^2H^2}{\lambda^7\cos^7\alpha}\right)\sin\varphi\cos\varphi = -\frac{Q\cos\varphi}{\mu A_\text{c}} \tag{5.14b}$$

Subtraction of (a) from (b) gives:

$$\lambda\sin(\alpha) = \frac{P\sin\varphi - Q\cos\varphi}{\mu A_\text{c}} \tag{5.15}$$

Lastly, Equation (5.10c) can be rewritten. As $m = 0$, the third term is 0. The second term can be rewritten as follows:

$$\tan\alpha\left(\frac{1}{\lambda^2\cos^2\alpha} + \frac{(\varphi')^2H^2}{\lambda^6\cos^6\alpha}\right) = \lambda\sin\alpha\left(\frac{1}{\lambda^3\cos^3\alpha} + \frac{(\varphi')^2H^2}{\lambda^7\cos^7\alpha}\right)$$

Using Equation (5.13), the right side can be rewritten to:

$$= \lambda^2\sin\alpha\cos\alpha + \lambda\sin\alpha\frac{Q\sin\varphi + P\cos\varphi}{\mu A_\text{c}}$$

Now Equation (5.15) can be used to substitute for $\lambda\sin\alpha$

$$= \lambda\cos\alpha\frac{P\sin\varphi - Q\cos\varphi}{\mu A_\text{c}} + -\lambda\sin\alpha\frac{Q\sin\varphi + P\cos\varphi}{\mu A_\text{c}}$$

Reordering the terms gives:

$$\begin{aligned} &= \frac{\lambda}{\mu A_\text{c}}\left(Q\left(\sin\alpha\sin\varphi - \cos\alpha\cos\varphi\right) + P\left(\sin\alpha\cos\varphi + \cos\alpha\sin\varphi\right)\right) \\ &= \frac{\lambda}{\mu A_\text{c}}\left(P\sin\theta - Q\cos\theta\right) \end{aligned} \tag{5.16}$$

With this result, Equation (5.10c) can thus be written as:

$$\left(\frac{1}{3}\frac{(\varphi')^2H}{\lambda^6\cos^6\alpha}\right)' = \lambda\frac{P\sin\theta - Q\cos\theta}{\mu A_\text{c}} \tag{5.17}$$

The problem has thus been reduced to a system of two equations (Equations (5.13) and (5.15) and one differential equation of second order (Equation (5.17)) with three unknowns (λ,α,φ). The remaining boundary conditions are $\varphi(0) = \varphi(S_\text{b}) = 0$.

To find the solution to this system of equations, a numerical approach (similar to the approach by He et al. [68]) is used. The approach is as follows:

1. The functions φ, α, λ (of x) are discretized for 50 points on the beam.
2. An initial guess is made for α and λ (on the 50 points).
3. With this guess of α and λ, and the boundary conditions, Equation (5.17) is solved for φ using a numerical solver based upon the Trust-Region-Dogleg Algorithm [69] (with use of the `fsolve` function in MATLAB). φ' is estimated using a central difference scheme.
4. The estimate of φ is then substituted in Equations (5.13) and (5.15). This gives 2 equations (for each point on the beam) with two unknowns: α and λ. This system of equations is then solved using the same numerical solver as in 3 .
5. Steps 3 and 4 are repeated until the solution is converged (the sum of differences in α and λ of the 50 points is less than 0.01).
6. The deformation of the beam in x and y coordinates can be found by summing the terms of Δu_0 and Δv_0 respectively. These can be found from λ and θ:

$$\Delta u_0 = \Delta x \lambda \cos\theta \tag{5.18}$$

$$\Delta v_0 = \Delta x \lambda \sin\theta \tag{5.19}$$

This approach is implemented into a MATLAB function, which can be found in Appendix D.

5.5 Finite Element Method simulations for mechanics

As an alternative to the calculations in the preceding sections, a Finite Element Method can be used to analyze the mechanical behaviour of the structure. The main advantage is that there is more freedom in the shape of the structure, where the calculations in previous sections were limited to bulk materials or beams. The main disadvantage is that the computation time is substantially longer.

For the FEM-simulation, again the Neo-Hookean model for hyperelastic materials is used with an incompressibility condition (i.e. $\nu = 0.5$). The FEM calculations are performed using COMSOL-Multiphysics. Also here it should be verified that the meshing into finite elements does not influence the result. To that extent the influence of the mesh is checked to be less than 1%, with a similar approach as is described in Section 4.3.

To compare the results of differnent beam models, a MATLAB-script that is connected to COMSOL (using COMSOL livelink for MATLAB) is made. This script varies different beam parameters and starts the simulations. For the simulations both 2D and 3D geometries can be used. In the 2-dimensional beam model, there is no deformation in the z-direction. With 3D geometries this assumption is not made. The influence of this assumption and the width of the structure, will further be discussed in Section 5.6.2. The 3D-FEM model is also used to simulate the deformation of the entire structure.

5.6 Comparison of beam models

In Sections 5.2, 5.4 and 5.5, three methods have been presented that can be used to find the deformation of a beam. In this section these three methods are compared. First, the shear-stress strain behaviour is compared between models. Secondly, the influence of normal stress on the beams is studied. Lastly, the influence of the two-dimensionality of the hyperelastic beam model is investigated by comparing the beam model to different FEM models.

5.6.1 Comparison of shear stress - strain behaviour

In Figure 5.3, the deformation in the horizontal direction due to a shear stress is shown for different beam thicknesses for three different models: linear (Timoshenko) beam theory (Section 5.2), hyperelastic beam theory (Section 5.4) and a 2-dimensional FEM beam model (Section 5.5). Only for very small strains, the Timoshenko- and hyperelastic beam model correspond. The relative deviation between the hyperelastic models is relatively small: less than 5% for all situations in Figure 5.3. The deviations decrease for smaller displacements and for smaller beam height over beam thickness ($\frac{H}{S_\text{b}}$) ratios.

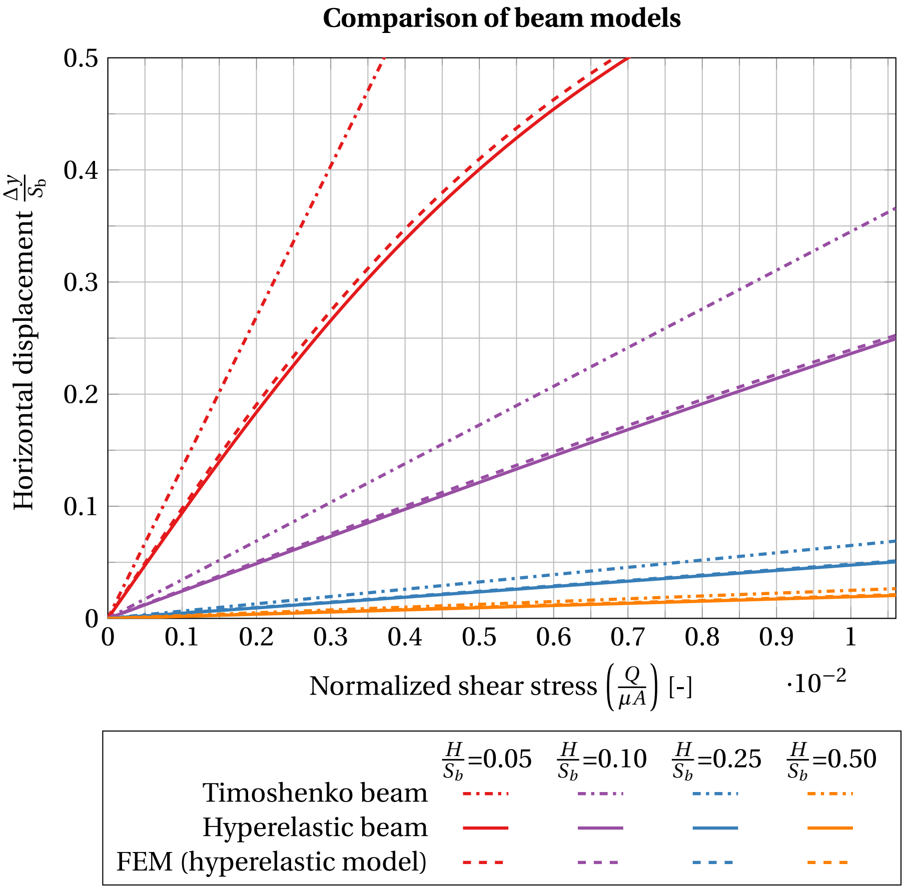

Figure 5.3: Horizontal displacement of beams as a function of applied shear stress (up to 10 times the expected shear stress with the shear modulus of Armadillo TPU $\mu = 132\,\text{MPa}$) and different beam thickness over height ratios ($\frac{H}{S_\text{b}}$), for three mechanical models.
(For readers in grayscale: Legend order is from top to bottom)

5.6.2 Influence of two-dimensionality assumption

In the hyperelastic beam model, one assumption that was made is that there is no deformation in the z-direction. This can have a substantial influence on the result, by two effects. One effect is that with deformation in the z-direction, the width of the beam is not constant (initially L). For tensile and shear stresses the beam will have a smaller width (except at its ends), causing more displacement in the x-direction. Another effect is that due to this deformation, together with the incompressibility condition, there will be less deformation in the y-direction: the thickness of the beam (H) will stay larger, which would result in less displacement in the x-direction.

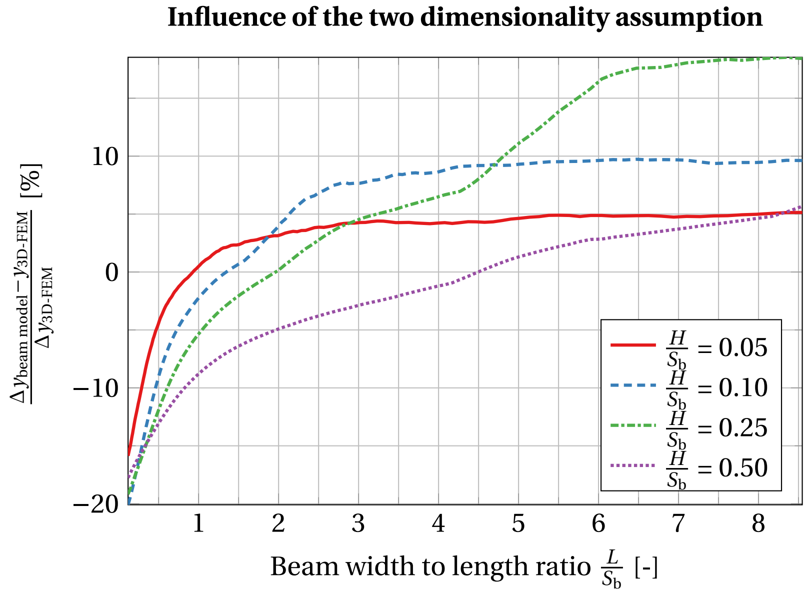

Figure 5.4: Deviation in horizontal displacement between the hyperelastic beam model and a 3D-FEM simulation, for different beam thickness to height ratios.

To quantify what the effects of this assumption are on the displacement, the 3-dimensional model (from section Section 5.5) is compared to the 2-dimensional FEM model and the hyperelastic beam model. In Figure 5.4, the deviations between the models are shown for various thickness ratios $\left(\frac{H}{S_b}\right)$.

5.7 Conclusion

In this chapter, various mechanical models have been presented to model the deformation of different structures; bulk materials and beams. The deformation of beams is studied in more detail: three models were presented and compared. The hyperelastic beam model (from He et al. [68]) corresponds well to FEM simulations, even for very thick beams (e.g. with a $\frac{H}{S_b}$-ratio of 0.5). One point of attention is the assumption that there is no deformation in the z-direction. If a model with this assumption is compared to a 3-dimensional model, it is clear that the 2-dimensional beam models are only suitable to be applied in certain ranges of beam widths L. Especially beams with a very small width or a combination of large width and large thickness $\frac{H}{S_b}$-ratio are unsuitable to find exact deformation with 2-dimensional models. Stress-strain behaviours are expected to show very similar trends as the deviation is rather independent of shear force, therefore the 2-dimensional models could be considered sufficient to find first estimates on ideal beam parameters.

In general, the beam structures are useful to have relatively large displacements (Δy) with a given thickness. This provides opportunities to have relatively large capacitance changes. How these opportunities can be used in a shear force sensor design will be the subject of the next chapter.

6 Design

In this chapter, the theoretical knowledge from previous sections will be used to design the first version(s) of the sensor. In Section 6.1, the general designs are presented. One design is selected and optimized electrostatically in Section 6.2 and mechanically in section Section 6.3. Remaining parameters are optimized in Section 6.4.

6.1 General design- and optimization choices

For the mechanical part of the design, a structure of beams seems optimal to have flexibility in one horizontal direction. To have large capacitance changes, it is favourable to have the wires relatively close together. To achieve this, a design such as sketched in Figure 6.1 can be used, where the wires are in a block connected to the top and bottom part of the structure. The bottom side contains two electrodes (indicated by different colours), to be able to measure differentially. (An alternative would be to have the wires inside beams which are close together, but the disadvantage is that it is not straightforward to apply a differential measurement).

In the design, choices need to be made for various parameters, such as the electrical (wire) layout and geometric dimensions. To be able to compare and optimize these parameters, an indicator is needed to assess the suitability of a design. From Chapter 2, the objectives that can be optimized in this stage are mainly the accuracy of (peak) measurements and the dimensions. With the selected readout technique Section 3.4, accuracy is mainly determined by absolute capacitance change that is caused by the applied shear stress. Therefore, in this chapter the goal is to optimize the capacitance change (in the measurement range from 0 to 140 kPa) per surface area of the sensor.

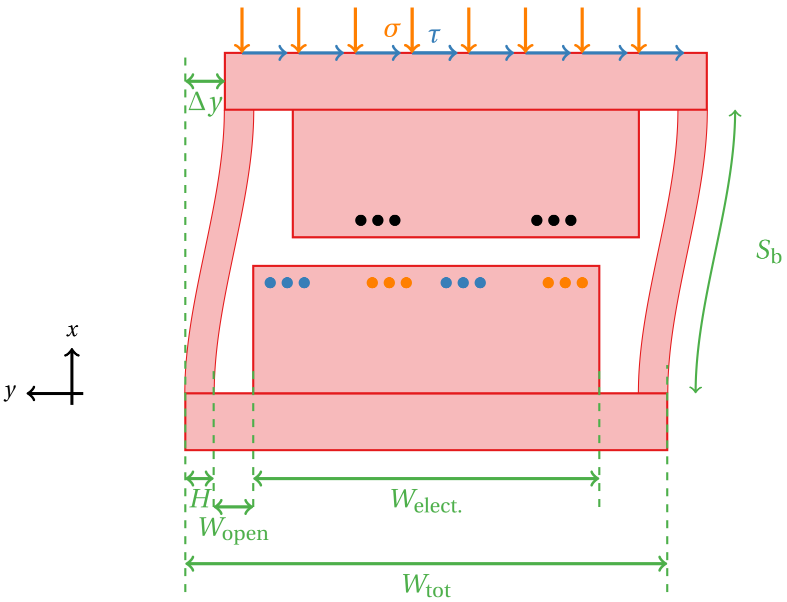

Figure 6.1: Sketch of the sensor design, with most parameters of the mechanical design and the shear- and normal stress

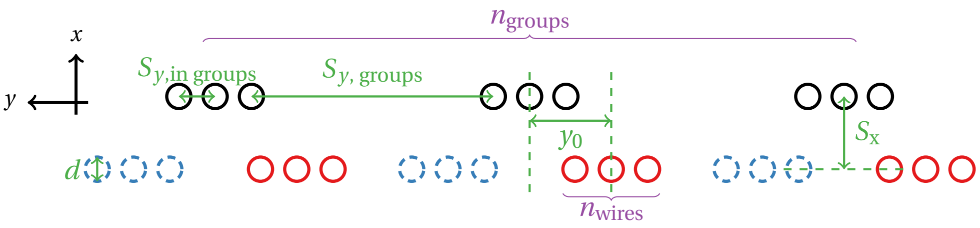

Figure 6.2: Sketch of the wire structure design of the sensor, with relevant parameters. The structure consists of a ground electrode (black, on top) and a positive (red, bottom) and negative (blue dashed, bottom) electrode, to measure differentially

6.2 Electrostatic optimization approach

As a start to finding an optimal electrode configuration, the optimization of wire structures is studied in more detail. In the selected design, the design freedom is chosen to be limited to structures as depicted in Figure 6.2. The structure contains three identical electrodes, consisting of groups of wires (3×3 wires in Figure 6.2), on the bottom there are two electrodes (positive and negative), which are positioned symmetrically around the symmetry line of the top electrode. In the initial situation the capacitance between the positive electrode and the ground electrode (on top) is the same as the capacitance between the negative electrode and the ground electrode.

In this structure, the wires are only at two different x-coordinates. Because the design will be optimized to have the largest capacitance change due to horizontal displacement, the separation in the vertical direction (S_x) should be relatively small and it was chosen to have this the same for all wires.

For the separation in the horizontal direction, two different values are used in the suggested structure: a number of groups (n_{groups}) have a separation of ($S_{y,\text{groups}}$). These groups contain a number of wires (n_{wires}), which are grouped together with a smaller separation ($S_{y,\text{in groups}}$). These groups, with a small intermediate separation, can be an approximation for plate structures. Especially since these plates have a small width, this is a reasonable approximation, see Section 4.5.1.

The first step in the optimiztion process of an electrode structure is to select which displacement range is most suitable to use, in other words, what initial horizontal displacement y_0 should be used. To do this, the negative electrode is first ignored, temporarily representing a non-differential measurement. The capacitance between the positive electrode and ground is plotted as a function of y_0 in Figure 6.3. Clearly, the capacitance is highest if $y_0 = 0$, as in that case the electrodes are closest together. The peaks at both sides are when the plates have shifted (almost) one plate, which is $4\,\text{m} + 2 \cdot 0.6\,\text{mm} = 5.2\,\text{mm}$. However, the rate of change of the capacitance $\left(\left|\frac{\mathrm{d}C}{\mathrm{d}y}\right|\right)$ is highest when there is some initial displacement (in Figure 6.3, that is $\pm 1.35\,\text{mm}$). To find the optimal value for y_0 without the need of calculating the function with a high resolution in a large range, the Nelder-Mead simplex algorithm [70] is used to find extreme values (using the `fmincon` function in MATLAB [71]). The result does not necessarily converge to the absolute minimum, as this convergence can only be achieved if the function is convex, which is not the case for the problem at hand. Therefore multiple starting positions are used to have a high chance of converging to the absolute minimum for most wire structures discussed here. The implementation in MATLAB can be found in Appendix E.

The optimization of all other parameters in the electrical design of the sensor will be done together with some mechanical aspects, and is further discussed in Section 6.4.

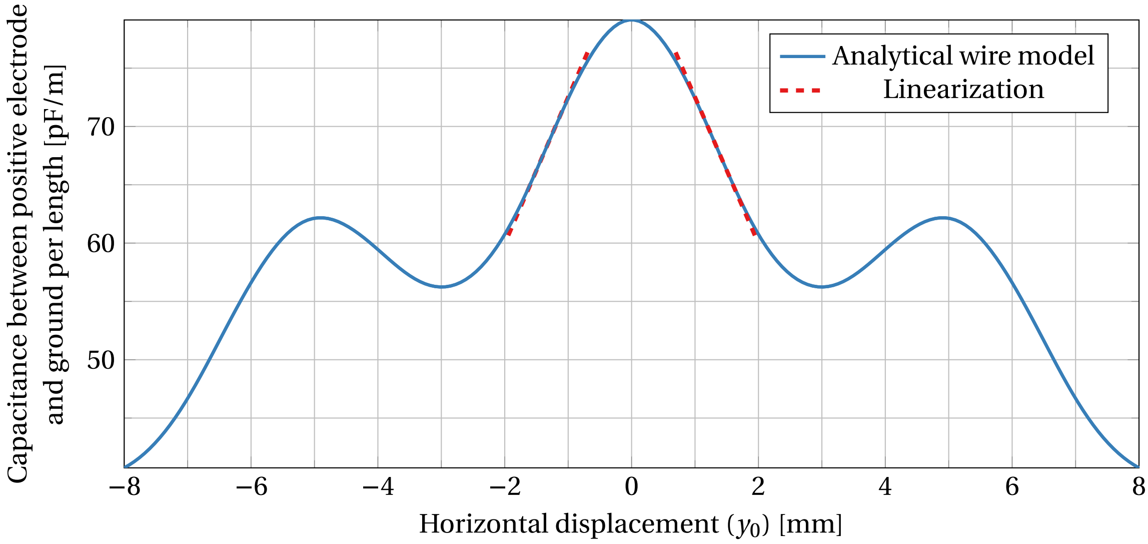

Figure 6.3: (Non-differential) capacitance change caused by horizontal displacement of one of the electrodes, for a wire structure with the parameters that are shown in Table 6.1, for which Figure 6.2 is to scale ($S_{y,\text{ in groups}} = 0.6\,\text{mm}, S_{y,\text{ groups}} = 4\,\text{mm}, S_x = 1.2\,\text{mm}, d = 0.4\,\text{mm}$). The linearization is made around the points with the highest (absolute) slope ($\pm y_0 =$).

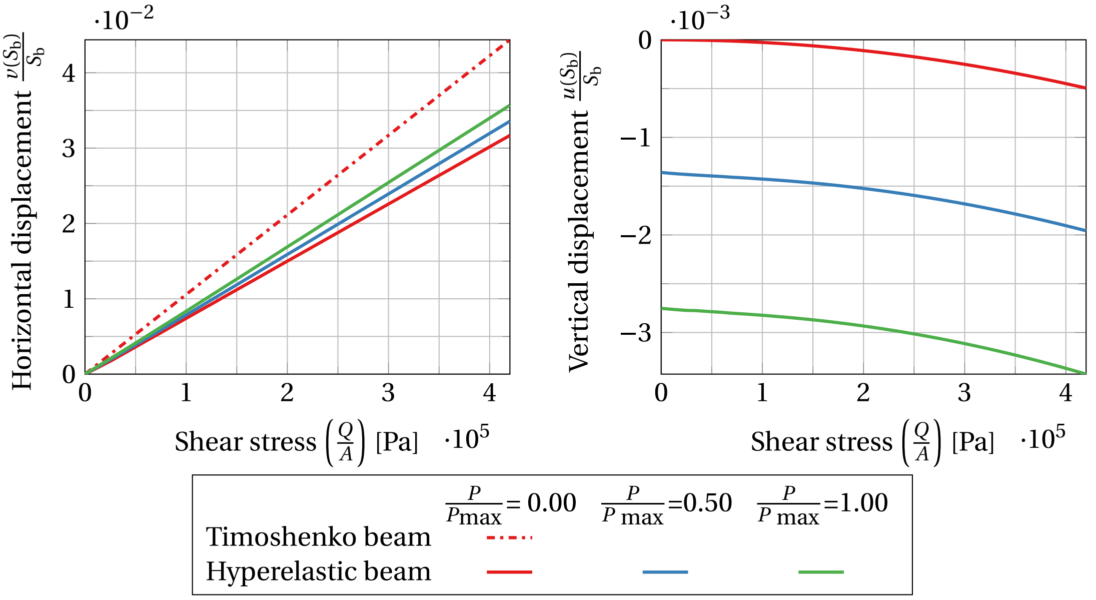

Figure 6.4: Horizontal and vertical displacement of a beam with initial shear modulus (μ) of Armadillo TPU (132 MPa [62]) and a $\frac{H}{S_b} = 0.1615$, with different (normal) pressures with $P_{\max} = 2 \cdot 740\,\text{kPa}$. The relative difference between the y displacement with $\frac{P}{P_{\max}} = 0$ and $\frac{P}{P_{\max}} = 1$ is $\leq 10\%$ for $\frac{Q}{A} \leq 2 \cdot 140\,\text{kPa}$

6.3 Mechanical optimization approach

The mechanical design of the sensor incorporates beams on both side of the structure. A disadvantage of these beam structures is that not only shear stresses influence the displacement of the electrodes. Normal stresses also influence this displacement. Normal stresses obviously cause some displacement in the vertical direction, but also in the horizontal direction the normal stress increases the horizontal displacement of a beam subject to a shear force, see for example Figure 6.4. This effect increases when the beam is deflected further from the vertical position, as the arm of the effective normal force increases in that case. To minimize this effect, the thickness of the beams (H) can be increased. The effect is that there is less displacement in the horizontal direction, thus lowering the influence of the normal stress. What beam thickness is needed depends on the (maximum) force that is acting on the beams. In Section 2.1, it was found that the shear stress and normal stress are expected to be below 140 kPa and 740 kPa respectively. As the area of the beam is smaller than the total surface area of the sensor, the stresses on the beam are larger:

$$\begin{aligned} \frac{P_{\text{max}}}{A_{\text{c}}} &= \frac{W_{\text{tot}}}{n_{\text{beams}} H} \cdot 740\,\text{kPa} \\ \frac{Q_{\text{max}}}{A_{\text{c}}} &= \frac{W_{\text{tot}}}{n_{\text{beams}} H} \cdot 140\,\text{kPa} \end{aligned} \tag{6.1}$$

With the hyperelastic beam model, it can be predicted what the deviation is in the horizontal displacement, between the situation with maximal normal stress and without normal stress. With use of a numerical solver based upon the Trust-Region-Dogleg Algorithm [69] (using the `fsolve` function in MATLAB), a reverse problem can be solved: finding the minimum thickness needed to have a deviation between the situation without and with maximal normal stress smaller than a given value, given the ratio of widths $\frac{W_{\text{tot}}}{n_{\text{beams}} H}$. For various maximum deviations (D_{max}), this is shown in Figure 6.5a. It can be seen that the slope in the graphs is always smaller than 1, meaning that using double the number of beams will result in a thickness that is more than half of the original thickness. (This could be expected from linear beam theory, as the deformation in the beam scales approximately $\propto H^{-3}$, see Equation (5.9)). It is therefore more space efficient to use fewer beams. Therefore, the design uses only one beam on each side of the sensor.

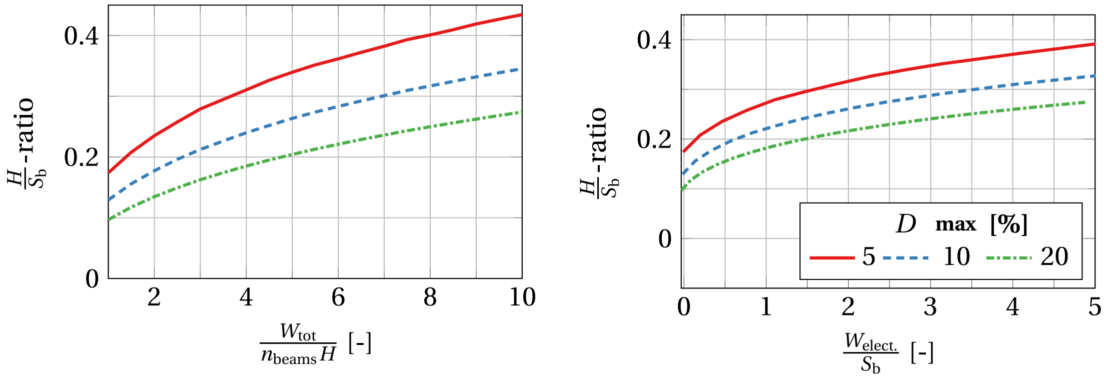

(a) Beam width to height ratios for a given area ratio $\left(\frac{W_{\text{tot}}}{n_{\text{beams}} H}\right)$

(b) Beam width to height ratios for a given width of the total electrode structure ($W_{\text{elect.}}$)

Figure 6.5: Beam width to height ratio $\left(\frac{H}{S_b}\right)$ for different maximum deviations (D_{max}) and given widths.

Apart from this note, the horizontal axis in Figure 6.5a is not very useful in the design. A more meaningful quantity can be used by noting that:

$$\begin{aligned} W_{\text{elect.}} &= W_{\text{tot}} - 2(H + W_{\text{open}}) && \text{(By definition, see Figure 6.1)} \\ &= 2W_{\text{open}} + 2H\left(\frac{W_{\text{tot}}}{n_{\text{beams}}H} - 1\right) && \text{(Using the ratio of widths)} \end{aligned} \tag{6.2}$$

By symmetry (see Figure 6.1), it can be seen that the deformation of the beam at the height of the gap between the top and bottom electrode is approximately one half of the total deformation (neglecting the gap space), therefore W_{open} should be at least $\frac{1}{2}\Delta y$. With this, the horizontal axis can be modified to show the width that is available for the electrodes $\left(W_{\text{elect.}}\right)$. This plot is shown in Figure 6.5b. This result is useful in the design process as for a given electrode structure, it indicates which beam width to height ratio is needed to have the desired maximum deviation. Note that deviation in horizontal displacement is in general not equal to the deviation of the capacitance. For the deviation of the capacitance, also the (relative) change in vertical separation between the electrodes is of importance. This effect can be reduced by making this distance initially larger, such that the relative change is smaller. However, this is a trade-off since this reduces the capacitance change substantially. The effect could also be partially be compensated using differential measurements, but still the sensitivity will be influenced.

6.4 Optimization of remaining parameters

In Sections 6.2 and 6.3, some optimalization choices are made. However, there are remaining parameters for which it is not immediately clear what value is optimal, these are:

Electrical parameters

- S_x
- $S_{y,\text{ in groups}}$
- $S_{y,\text{ groups}}$
- n_{wires}
- n_{groups}
- d

(see Figure 6.2)

Mechanical parameters

- Design error $D_{\max}$ due to normal stresses
- Length of the beam S_b
- Material, in particular the initial shear modulus μ.

To see how these parameters influence performance of the sensor, a tool is developed to interactively study these relations. For this, MATLAB App Designer is used. The models described in Chapters 4 and 5 are used in this tool, together with the optimization choices made in Sections 6.1 to 6.3. A screenshot of the tool is shown in Figure 6.6. The typical use of the tool is as follows: the initial design parameters are entered in the user input, there is an option to plot the structure or its shear stress-capacitance behaviour. Two parameters can be selected together with a range of values to be sweeped. This is the key function of the tool as it gives insight in the combined influence of the parameters. The results are shown in a surface plot. This surface plot is interactive: it can be clicked to plot the structure and the shear stress-capacitance function of the structure corresponding to the point in the surface-plot (shown as a red dot). By default, the center-wire approximation (Section 4.2.2) is used for the electrostatics, because the computation time is drastically lower (3 orders of magnitude). For some structures near the optimum, the shear stress-capacitance behaviour can be verified using FEM, with an infinite length wire, finite length wire or a finite length plate FEM simulation as described in Section 4.3. For the mechanics, the beam width and structure width can be set manually, or alternatively automatically by setting a design error these parameters are automatically chosen using the method described in Section 6.3. Resulting figures can be exported to a standalone MATLAB-figure or saved as comma separated values (`.csv`-file).

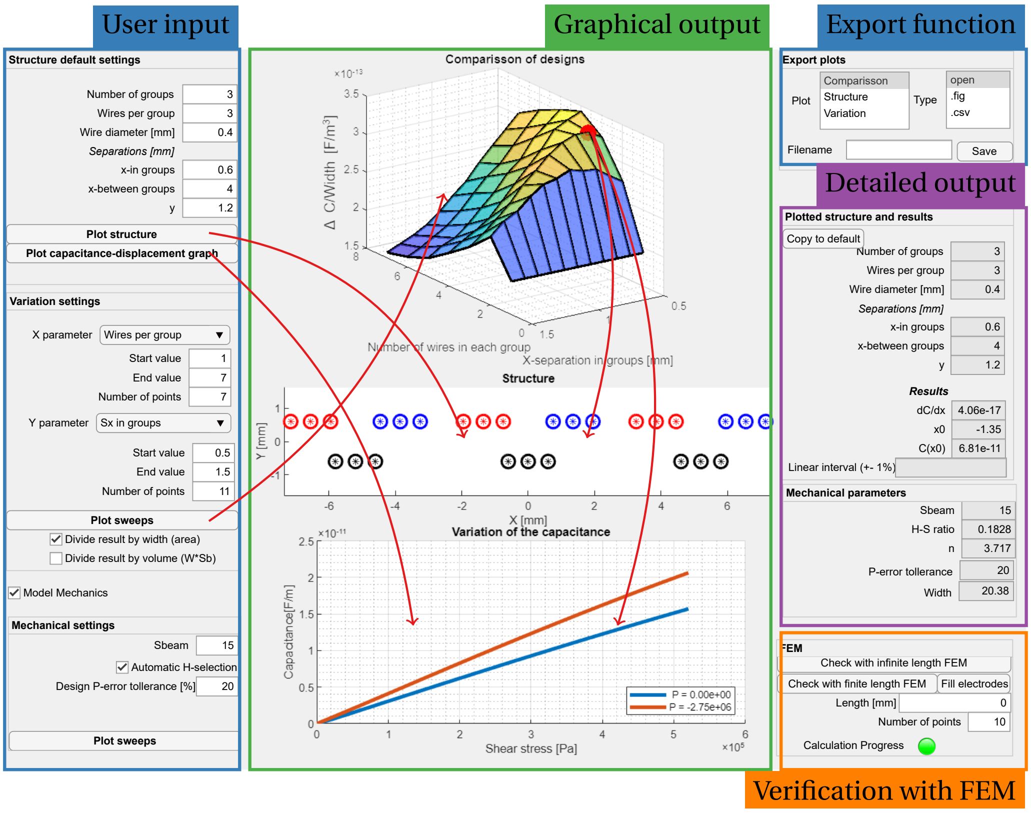

Structure default settings

Number of groups: 3
Wires per group: 3
Wire diameter [mm]: 0.4
Separations [mm]
x-in groups: 0.6
x-between groups: 4
y: 1.2

Variation settings

X parameter: Wires per group
Start value: 1
End value: 7
Number of points: 7
Y parameter: Sx in groups
Start value: 0.5
End value: 1.5
Number of points: 11

☑ Divide result by width (area)
☐ Divide result by volume (W*Sb)
☑ Model Mechanics

Mechanical settings

Sbeam: 15
☑ Automatic H-selection
Design P-error tollerance [%]: 20

Export plots

Plot: Comparisson / Structure / Variation
Type: open / .fig / .csv
Filename:

Plotted structure and results

Number of groups: 3
Wires per group: 3
Wire diameter [mm]: 0.4
Separations [mm]
x-in groups: 0.6
x-between groups: 4
y: 1.2

Results

dC/dx: 4.06e-17
x0: -1.35
C(x0): 6.81e-11
Linear interval (+- 1%):

Mechanical parameters

Sbeam: 15
H-S ratio: 0.1828
n: 3.717
P-error tollerance: 20
Width: 20.38

Length [mm]: 0
Number of points: 10

Figure 6.6: Graphical user interface of the MATLAB App, designed to optimize the design of the sensor, with annotations.

6.4.1 Optimization of remaining parameters

The remaining parameters from the list on page 35 are determined using the MATLAB App. The sweep function in the tool is used multiple times to converge to an optimal situation, this entails sweeping all parameters multiple times, as their influence can depend on other parameters. In the this section only the last results are shown to show the influence of a parameter change relative to the selected design.

Design error and material choice

The design error D_{max} for the first iteration of the sensor was chosen as a relatively high value of 20%. This was done because an increased design error allows more horizontal displacement, which, for most designs, increases the capacitance change. In a later design the design error D_{max} can be reduced if the actual measurement results have a large enough signal. For the material choice, Armadillo TPU is selected as the most suitable material for the sensor design. A kind of TPU is most practical to apply here to have a good adhesion with the conductive PI-ETPU material, plus that the stiffness of Armadillo TPU is required to have beams with a reasonable width: Ninjaflex and Semiflex are far to flexible to have beams with a thickness to height ratio smaller than 1 in the desired measurement range.

For measurements however, also prototype sensors are made using Ninjaflex TPU. This was partially because Armadillo was not available during experiments, but also because the sensor is expected to have a smaller measurement range: as the shear modulus of Ninjaflex is 33 times lower than that of Armadillo, the deformation of Ninjaflex is expected to be the same as for Armadillo, but for 33 times smaller loads. This is advantageous as in that case the entire measurement range can be studied by means of the actuator used in the experiments (see Section 8.1).

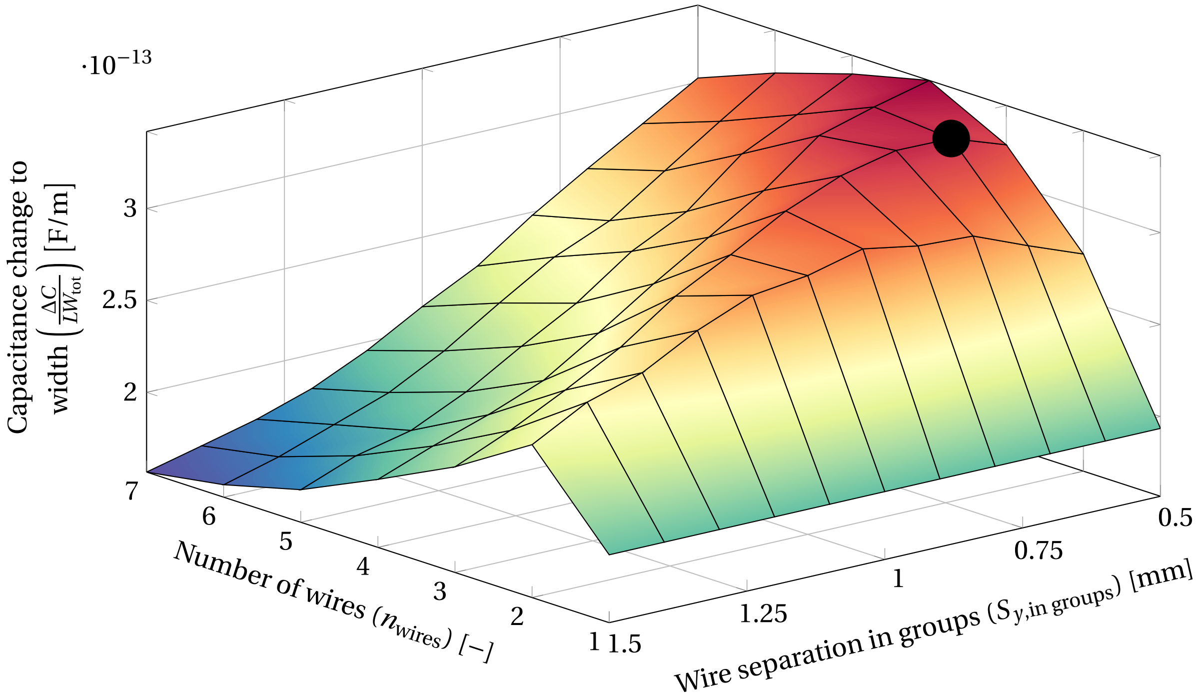

Figure 6.7: Influence of the number of wires in a group and their separation on the capacitance change. The selected design is shown as a black dot.

Number of wires per wire-group and the separation of wires in these groups

The influence of the number of wires per wire group and the separation in these groups can be seen in Figure 6.7. It can be seen that a relatively small separation is favourable, note that for a separation smaller than the diameter d, the wires intersect. If fewer wires are used, a relatively larger separation is favourable. From the figure it seems like it could be favourable to use plates instead (as there is no separation in that case), especially if more wires are used.

Number of groups and separation between the groups

In Figure 6.8, the influence of the number of groups and their separation on the capacitance change is shown. Obviously, the separation between groups does not have an influence in case there is only one group. Compared to this case, there is a clear optimum slightly below 4 mm for the separation between groups for ≥ 2 groups. For a smaller separation, the capacitance change decreases severely because the groups are closer together and start to act more like a single plate capacitor. On the contrary for a larger separation the increase in capacitance change does not weigh up to the added width of the structure. Instead of separating the groups more, it would be more favourable to add an extra group to increase the capacitance change. It was chosen to have a separation of 4 mm, which is at the optimum. (This also leaves sufficient distance between the electrodes to mirror the negative electrodes for a differential measurement. This is relevant as the separation between groups is defined between groups belonging to the same electrode, see Figure 6.2) For the number of groups 3 was chosen as that was expected to yield a large enough capacitance change and the width of this structure is reasonable.

Vertical separation and beam length

In Figure 6.9, the influence of the vertical separation and the length of the beam on the capacitance change is shown. The vertical separation has a large influence on the capacitance change, however the smaller the vertical separation is, the larger the influence of the normal force will be. This effect is not included in the design error. Therefore a vertical separation of 1.2 mm is selected. The length of the beam does influence the capacitance change in a more linear way: increasing the length by a certain factor increases the capacitance change by a slightly lower factor. For the first iteration of the design, a relatively large length of 15 mm is chosen to achieve a higher displacement and thus a higher capacitance change.

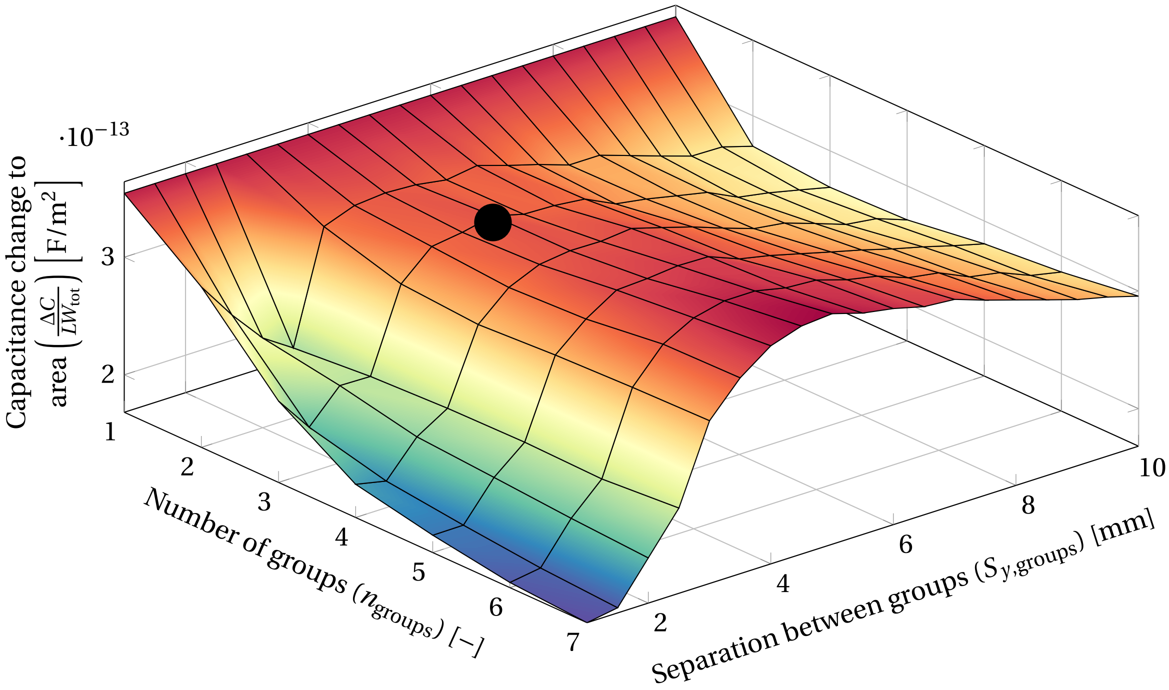

Figure 6.8: Influence of the number of groups and their separation on the capacitance change. The selected design is shown as a black dot.

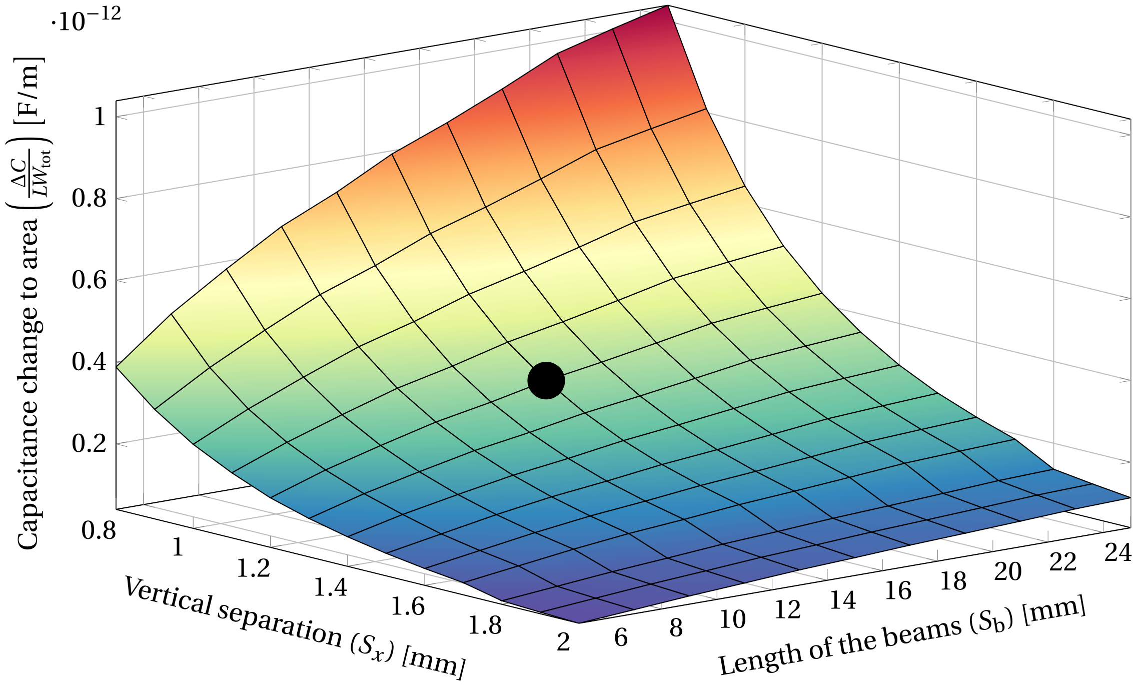

Figure 6.9: Influence of the vertical separation and the beam length on the capacitance change. The selected design is shown as a black dot.

Parameter	**Value**	**Value small design**
Shear modulus μ	132 MPa (Armadillo)	132 MPa (Armadillo)
(μ)-2 (design for experiments)	4 MPa (Ninjaflex)	
Design error due to normal force D_{max}	20 %	20 %
Beam length S_{b}	15 mm	5 mm
Beam thickness H	2.81 mm	0.98 mm
Total width W_{tot}	22.22 mm	8.75 mm
Width open space W_{open}	0.90 mm	0.32 mm
Width electric layout $W_{\text{elect.}}$	14.7 mm	6.2 mm
Length of wires, width of beams L	22 mm	8.75 mm
Horizontal separation in groups $S_{y,\text{, in groups}}$	0.6 mm	0.6 mm
Separation between groups $S_{y,\text{ groups}}$	4 mm	4 mm
Vertical separation S_{x}	1.2 mm	0.7 mm
Wire diameter d	0.4 mm	0.4 mm
Number of groups n_{groups}	3	3
Number of wires per group n_{wires}	3	3
Initial horizontal displacement of wires y_0	1.35 mm	1.35 mm

Table 6.1: Parameters for the design

6.4.2 Final design choices

The design parameters that were determined using the design tool and the methods described in Sections 6.1 to 6.3 are summarized in Table 6.1. The length of the structure and the wires (in the z-direction) is chosen to be 22 mm such that the structure is approximately square. The electrostatic model is verified using FEM, also for a situation with rounded plates instead of the proposed wire structure (the plate FEM model used in Section 4.5.1).

The described design process is repeated with as main difference a different number of groups and a smaller beam separation and seaparation in the y-direction. This resulted in an alternative design of $8.75 \times 8.75 \times 11\,\text{mm}^3$, the parameters can be found in Table 6.1.

6.4.3 Model prediction

For the final sensor design, a model prediction is made using the models in Chapters 4 and 5. For the mechanic model, the hyperelastic beam model is used as analytic model. The FEM model is a FEM model of the entire sensor geometry. The results are shown in Figure 6.10. As the results are very linear, the direction of a linear fit of the model is determined to be able to compare experimental results easily. The slope of the FEM model is 773 mm/[−], the slope of the analytical model is 478 mm/[−].

For the electrostatic model, the capacitance change is plotted against horizontal displacement. Also the vertical displacement influences the result, the vertical displacement for a given horizontal displacement is found using the mechanical FEM model. For the analytical model prediction, the center charge approximation is used. The FEM model uses a rounded plate model with finite length. The results are shown in

6.5 Conclusion

In this chapter, all theoretical models from previous sections are used to design the sensor. To optimize the general design concept a tool was developed to achieve insight in the influence of the different parameters on the sensor performance. Using this tool, optimal parameters were selected, on which the final design is based. In the following chapters, the fabrication and characterization of this design is discussed.

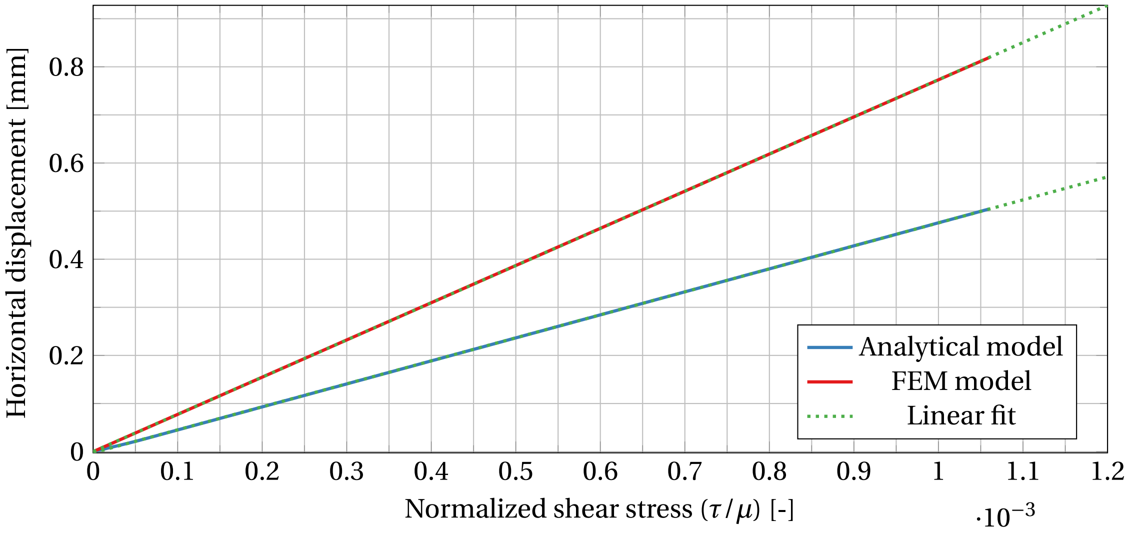

Figure 6.10: Mechanical model prectiction

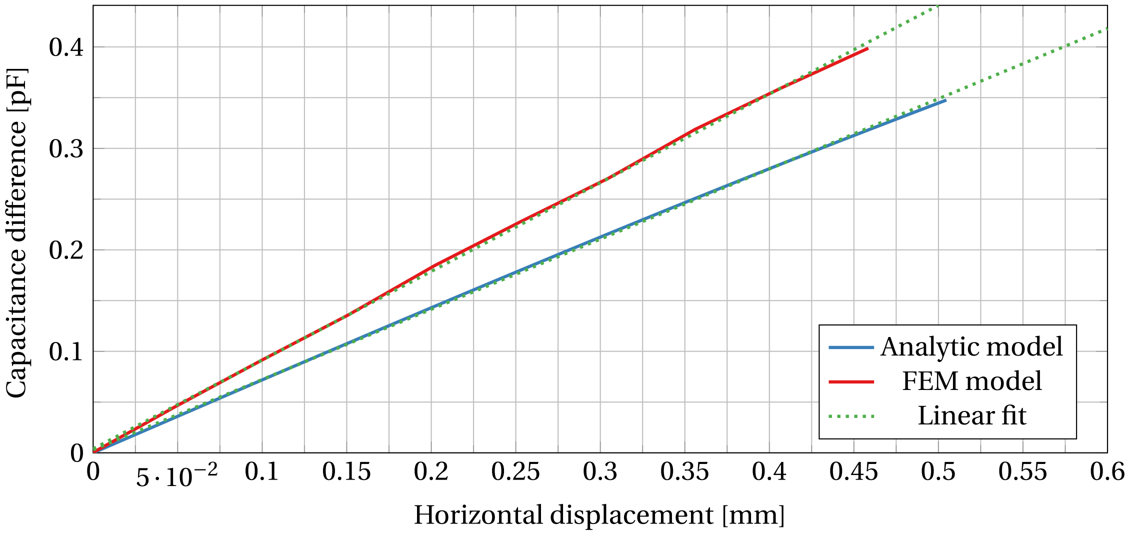

Figure 6.11: Electrostatic model prectiction

7 Fabrication

In this section, the fabrication of the sensor is described. In Sections 7.1 and 7.2 the design and its modifications are discussed. Section 7.3 describes the slicing and printing process and Section 7.4 the post-processing steps.

7.1 3D model

A 3D model of the sensor is created using Computer Aided Design (CAD) in Fusion 360 (Autodesk). The conductive parts will consist of a plate like structure, where it is made sure that the traxels are printed in the longitudinal direction, such that the conductivity is best in this direction. In the design in Fusion 360, the plates are drawn as rectangles (see Figure 7.1), the printing process will make these slightly rounded. There are other slight differences in the parameters when it is being printed, as the height of features is determined by a whole number of layers of finite thickness. Copper wires are connected to the conductive structures. These wires can later be used to connect the sensor to the readout device. To be able to connect the wires, the plates are extended to the side of the sensor and larger and thicker rectangles (bond pads) are added, see Figure 7.2. These bond pads are printed on both sides of the print to prevent retractions (ending a line segment) near the narrow part of the sensor, as this can lead to droplets of unwanted material.

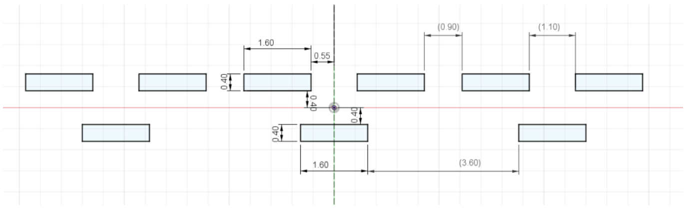

Figure 7.1: Dimensions of the electric layout (side view, the in plane length is 22 mm)

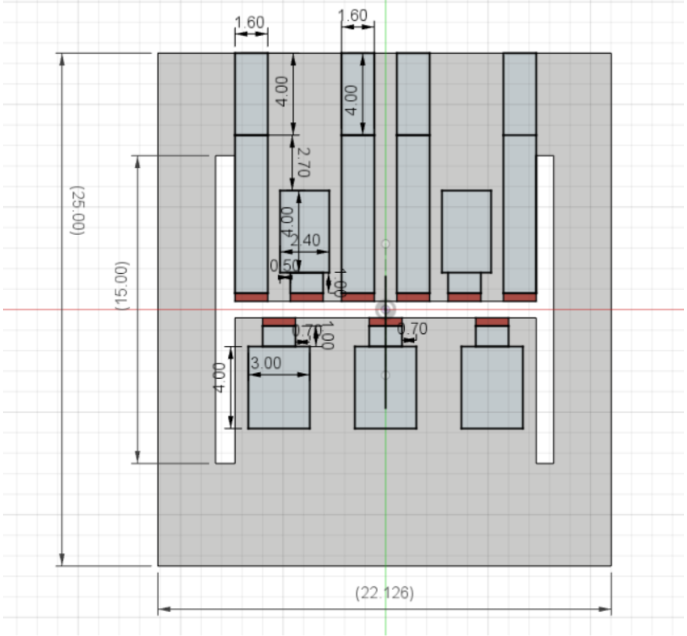

Figure 7.2: Dimensions of the mechanic layout (side view of the sensor, the in plane length is 22 mm). The main conductive layout as shown in Figure 7.1 is shown in red, to this the larger bond pads are connected in the side of the structure.

Type	Sensor	Changes made
Large Ninjaflex	1,2	First design with larger bond pads
	3-1a, 3-1b, 3-1c	The larger bond pads are spaced further apart
	5a, 5b	Design with smaller bond pads (Figure 7.2)
Large Armadillo	Armadillo1, Armadillo2	Like 5a, 5b, but with a stiffer material (Armadillo)
Small Armadillo	small	Substantially reduced size of the sensor

Table 7.1: Different sensors and their differences

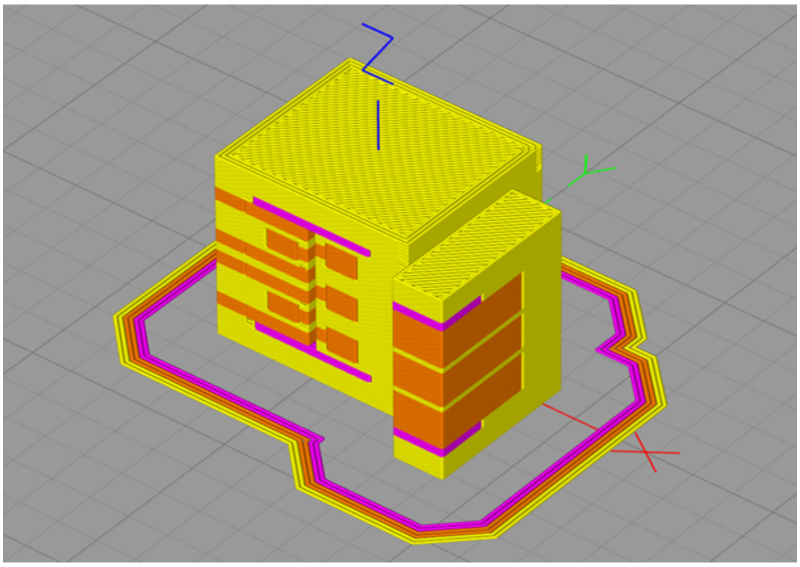

Figure 7.3: Sliced model in Simplify 3D (on the right the prime tower can be seen, which is not part of the sensor)

7.2 Design modifications

During the experimentation process, some changes are made to the sensor design. The different iterations of the sensor are summarized Table 7.1.

7.3 Slicing and printing

For the printing a Diabase H-series 3D-printer is used. To prepare the model for printing, the model is converted to machine instructions for the printer. To do this, the model is converted to a layered structure, where the layers in turn consist of lines (traxels). A layer thickness of 0.2 mm is used. A prime tower is printed next to the sensor to prime the nozzles before each layer. This helps to prevent the contamination of the print with some excess material that can be on the nozzle. The remaining slicing- and printing settings can be found in Appendix F. To reduce the resistance of the conductive parts, the sensor is printed such that the traxels are in the direction of the current. The sensor is therefore printed on its side. A figure of the sliced model is shown in Figure 7.3.

During the printing process, a 3D-printing spray (Dimafix) is used to improve the adhesion of the support material (BVOH) to the TPU's (Ninjaflex and Armadillo). This is needed when the support material is printed on top of the TPU, in reverse, the adhesion is good enough without application of the spray.

7.4 Post-printing steps

It is known that the resistance of the conductive ETPU decreases over time, this process can be sped up by annealing the print [7]. Therefore the prints were heated for 10 hours in an oven at 80 °C. After this, the print is cleaned with ethanol and wires are melted in the bond pads. A photograph of all sensors can be found in Appendix G.

7.5 Conclusion

For the fabrication process of the sensors, the following steps are taken: the model is drawn in three dimensions using CAD. Next, the 3D-model is sliced and printed. The print is heated, after which the wires are connected to the sensor.

8 Characterization

This chapter discusses the characterization of the different sensors. In Section 8.1, the measurement setup and -method are introduced. Section 8.2 shows the experimental results measured using this setup.

8.1 Measurement setup

This section discusses the measurement setup that is used to characterize the sensors. A schematic overview is shown in Figure 8.1. Below, the details of the different parts of the system are discussed.

Sensor positioning
The positioning of the sensor is shown in Figure 8.2. The sensor is clamped in a vise on the bottom. On top the sensor is clamped between two plates on a screw. Preferably, this is a plastic screw as the metal tip of the linear actuator is conductive which can influence the sensor if it is touching some conductive parts. (Some first measurements are performed using a metal screw). The screw is connected to a load cell, which in turn is connected to the linear actuator.

Control and measurements of the linear actuator
The linear actuator (SMAC LCA25-050-15-6 [72]) is used excert a force. The device can measure the force and position. MATLAB is used to control the linear actuator. Three different input

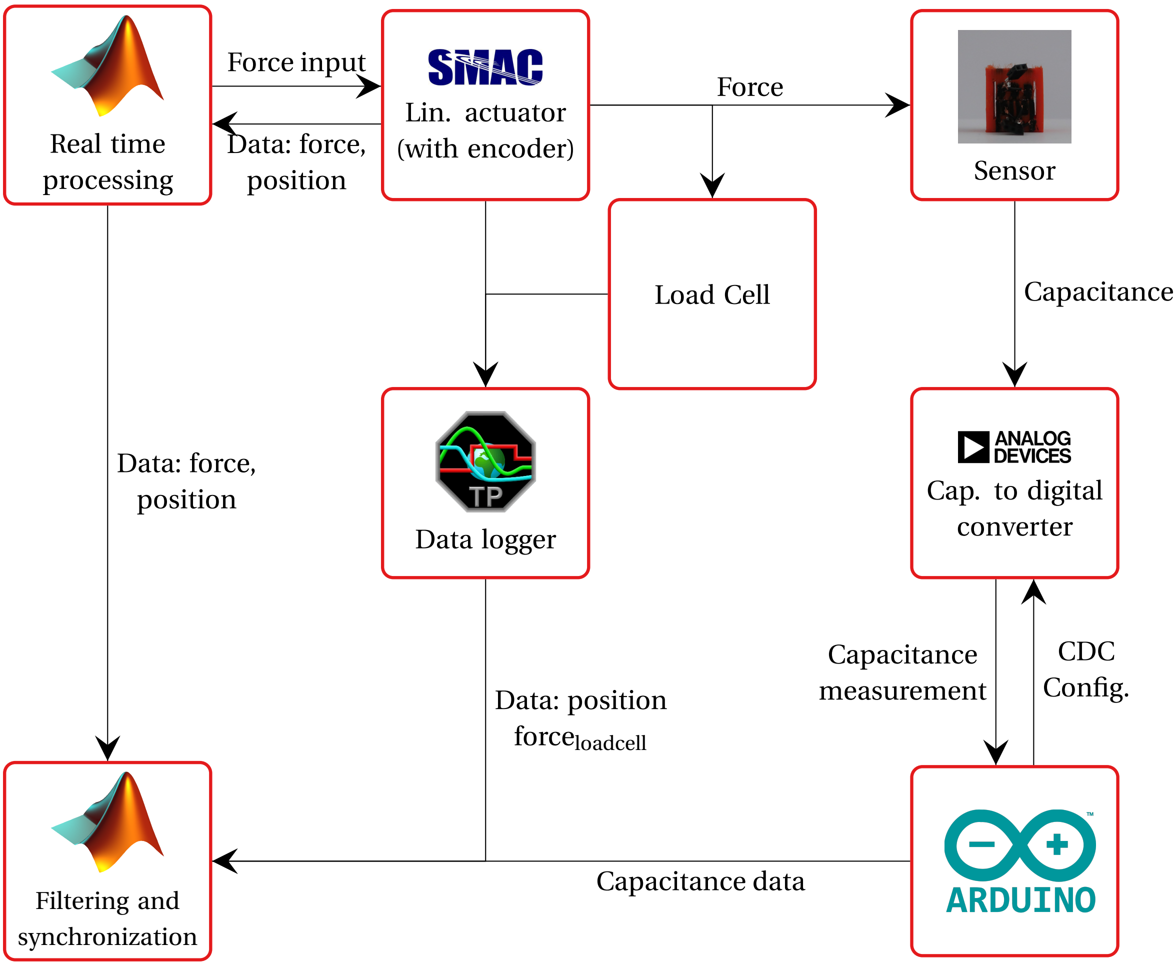

Figure 8.1: Schematic overview of the measurement setup

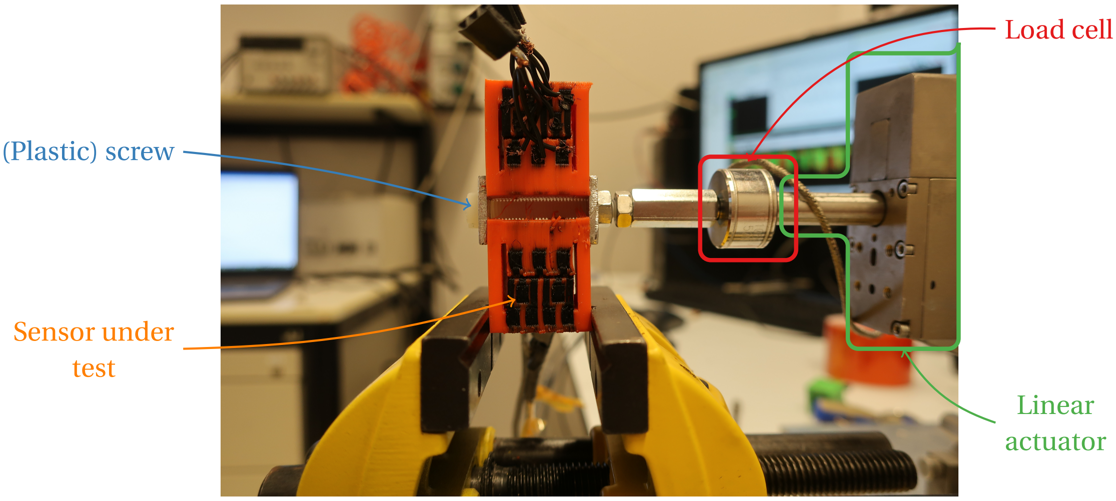

Figure 8.2: Positioning of the sensor and connection to the linear actuator (SMAC).

signals are used: a sine wave with a period of two seconds, a square-like wave, where the input cycles between three levels: positive signal, zero, negative signal, zero. A period of 12 seconds is used. A variation of this wave is a trapezium like wave, where instead of steps, the force is changed linearly in one second. A plot of these input signals can be found in Figures 8.3 to 8.5 on page 46.

Capacitance measurements
Capacitance is measured using an Analog Devices Capacitance to Digital Converter (CDC), (AD7747 with evaluation board [44]), which is configured and read out by an Arduino Pro Micro. The sampling period is 50 ms.

Force measurement using load cell
To have more accurate force measurements, a load cell is used. This is more accurate than the measurement of the linear actuator and the internal friction in the actuator does not influence this measurement. The signal of the load cell is measured using a TiePie digital oscilloscope, which is configured for use as a data logger. The position measurement from the linear actuator is also measured using the data logger to be able to synchronize the data.

Filtering and synchronization
After the measurement, the measured capacitance data and the force data from the datalogger is filtered using a low-pass filter with a cut-off frequency of 10 Hz and 30 Hz respectively (Butterworth filter design with two parameters using the `butter`-function in MATLAB). The offset in both the force and position channel is compensated by subtracting the first datapoint (which is always unloaded). The Arduino data is synchronized by measuring the first data point during the real time processing. The data from the data logger is synchronized by comparing the position signals. The delay that is needed to synchronize the data is found by finding the delay for which the sum of square differences between the data is as low as possible (using the `fminsearch`-function in MATLAB).

8.2 Experimental results

In this section, the experimental results of the sensor are discussed. The measurement results of a single sensor are discussed in detail in Sections 8.2.1 to 8.2.4. The fitting results of all sensors are compared to the model in Section 8.2.5. The detailed measurement result for each sensor can be found in Appendix H.

8.2.1 Measurement results for different input signals

In Figures 8.3 to 8.5, the force and capacitance measurements over time are shown for the three different force input signals (as discussed in Section 8.1). The capacitance measurements seem to resemble the input signals relatively well. A thing to note is that in the capacitance measurement of the trapezium force input (Figure 8.4) the measurements of a 0 input signal at the upwards and downwards stroke are not at the same level. Also there is some relaxation behaviour in the parts where the force is held constant, both for the trapezium and the square-like input (Figures 8.4 and 8.5). The time constant associated with this is studied in Section 8.2.4. This effect of hysteresis can also clearly be seen if force is plotted against capacitance, see Figure 8.6.

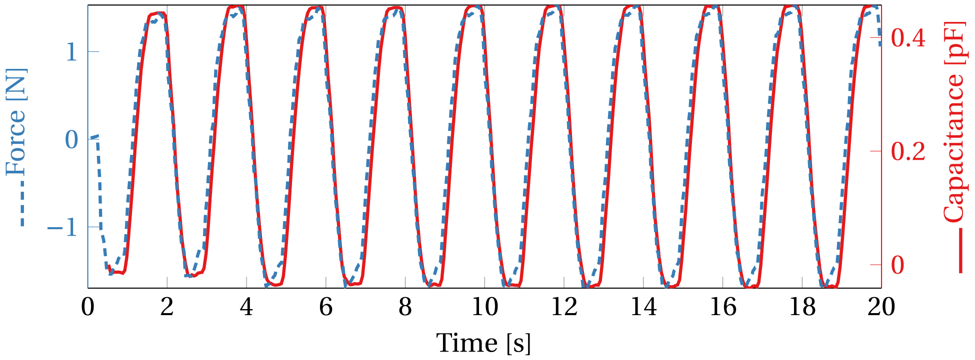

Figure 8.3: Force and capacitance over time for a sine wave force input (sensor 5a)

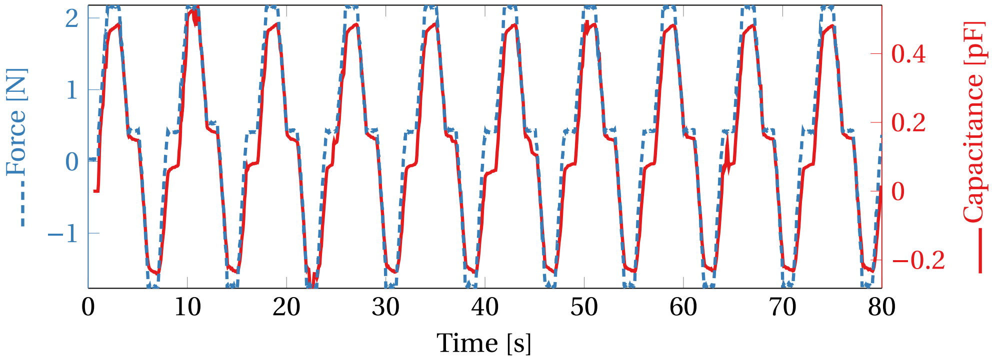

Figure 8.4: Force and capacitance over time for a trapezium force input (sensor 5a)

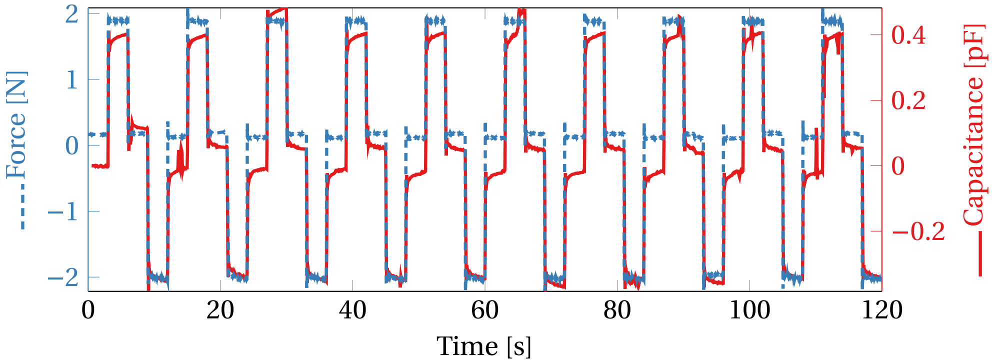

Figure 8.5: Force and capacitance over time for a square-like force input (sensor 5a)

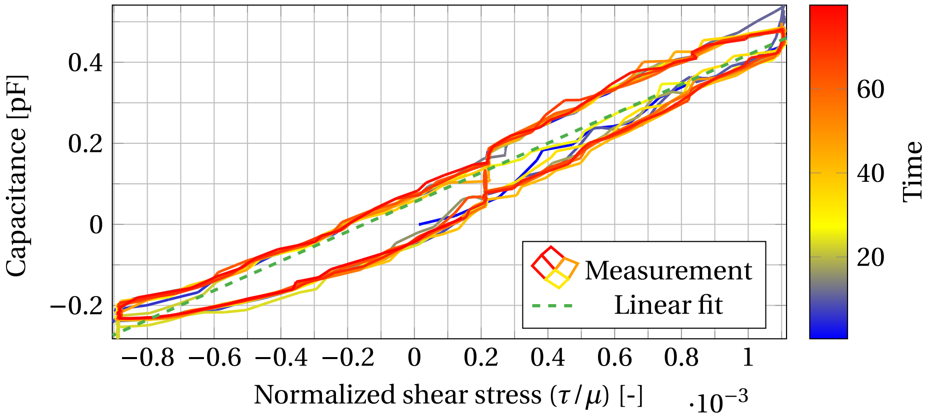

Figure 8.6: Force to capacitance plot for a trapezium force input on sensor 5a

8.2.2 Mechanical behaviour

To study the mechanical behaviour in more detail, the displacement measurements of the linear actuator can be used. In Figure 8.7, the measurements are shown over time. In Figure 8.8, the force-displacement plot is shown. From these results a similar hysteresis behaviour can be seen as in the force to capacitance relation. To the data in this plot, a linear fit is made. This fit does not describe this hysteresis behaviour, but captures the general behaviour moderately well ($R^2 = 0.95$).

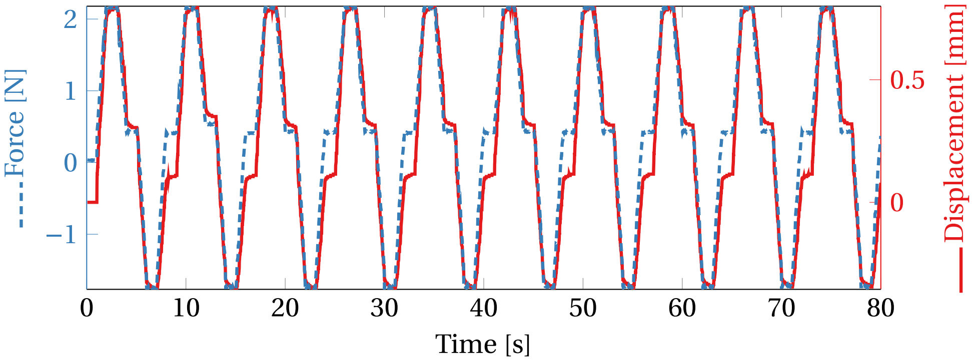

Figure 8.7: Force and displacement measurement for a trapezium force input (sensor 5a)

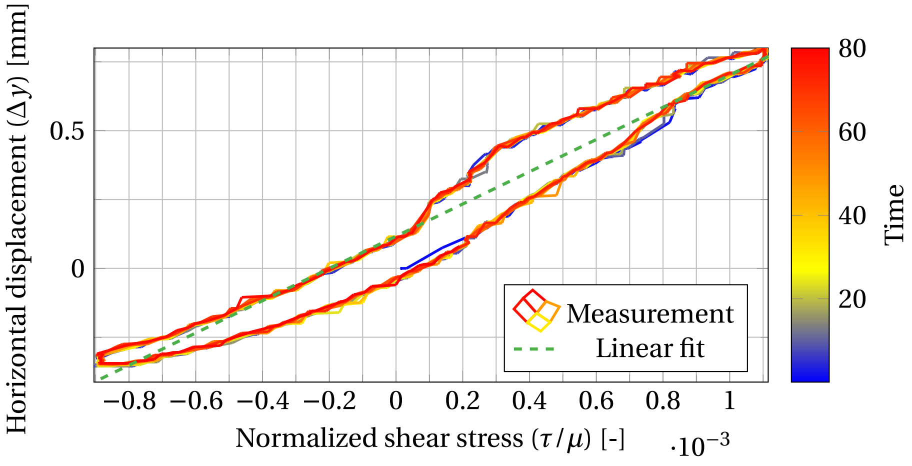

Figure 8.8: Force to displacement plot for a trapezium force input on sensor 5a, with a linear fit

8.2.3 Electrostatic behaviour

Like in Section 8.2.2, the electrostatic behaviour can be studied by the displacement and capacitance measurement. The results over time are shown in Figure 8.9. Figure 8.10 shows the displacement to capacitance plot. From this plot it is clear that there is little to no hysteresis in the electrostatic part of the sensor: the measured data corresponds relatively well to the linear fit ($R^2 = 0.99$).

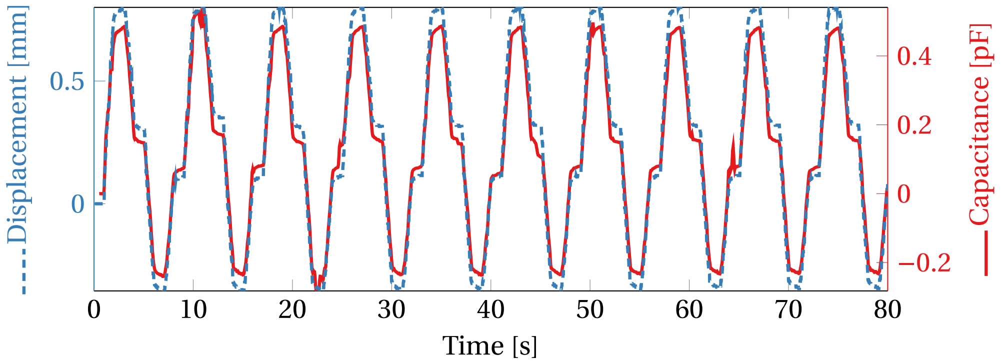

Figure 8.9: Displacement and capacitance measurement for a trapezium force input (sensor 5a)

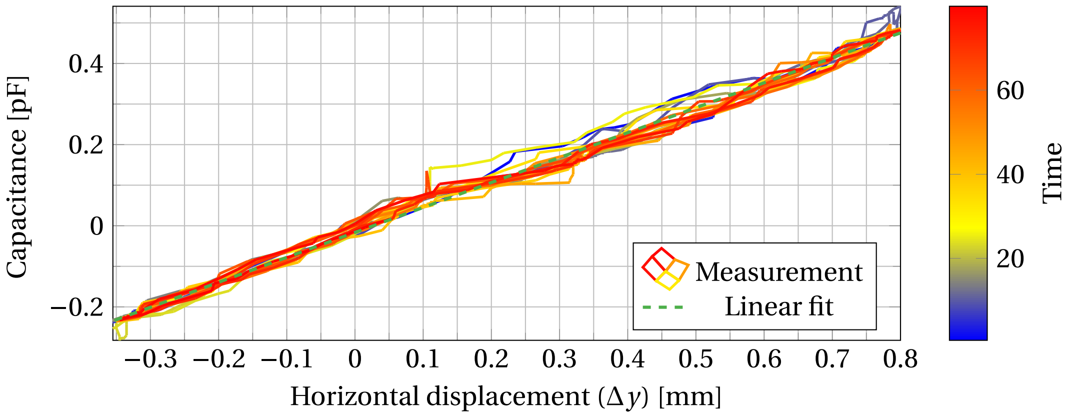

Figure 8.10: Displacement to force plot for a trapezium force input on sensor 5a, with a linear fit

8.2.4 Determination of the (mechanical) time constant

In the response to the square like wave, there is a slow relaxation effect towards a steady value in the mechanical domain. This trend seems to be exponential. In this section the time constant of this effect is determined. To do this, the increase of each step is shifted such that all responses can be captured by one exponential fit. For all steps towards a positive value, this is shown in Figure 8.11. Using a trust-region algorithm [69] (the `fit` function in MATLAB), an exponential is fitted of the form $be^{at} + c$. This exponential describes the behaviour of the sensor relatively well ($R^2 = 0.97$), as can be seen in Figure 8.11. Most of the deviation is caused by the resolution of the position measurement of the linear actuator (5 µm). For the steps towards positive values, a time constant of $-1/a = 1.17$ s is found. For the steps towards negative values the same method yields a time constant of 1.15 s. For an Armadillo sensor (Armadillo1), the time constant is found to be 2.0 s.

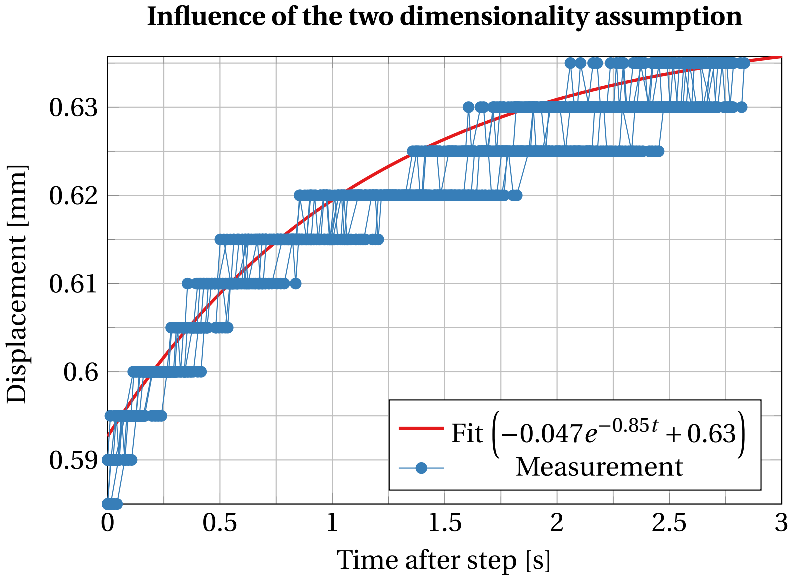

Figure 8.11: Determination of the time constant of the relaxation effect after a step in the square wave input for sensor 5a.

8.2.5 Comparison of sensor performance with the model

The linear fit results from all sensors (which can be seen in Appendix H) can be compared to each other and the model expectations (see Section 6.4.3). The results are shown in Table 8.1. In the first three columns, the three linear fits are compared. The last column shows the resistance between positive and negative electrodes, which ideally is infinite.

8.2.6 Small sensor results

With the small sensor, a single measurement is done with the sine wave input. The results are shown in Figures 8.12 to 8.14. The slope of the fit is 124 pF/[−], making the sensitivity 0.9 pF/MPa.

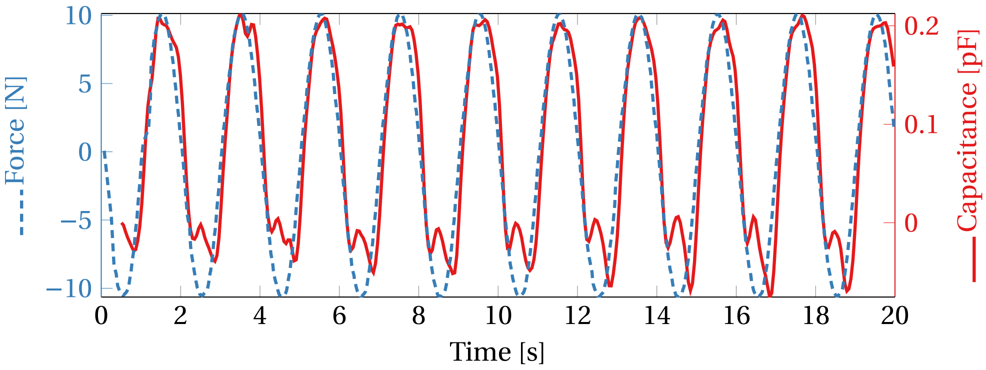

Figure 8.12: Force and capacitance over time for a sine wave force input applied to the small sensor

Sensor	**Total** $\left(\mu\frac{\mathrm{d}C}{\mathrm{d}\tau}\right)$ [pF]	**Mechanic** $\left(\mu\frac{\mathrm{d}y}{\mathrm{d}\tau}\right)$ [mm]	**Electrostatic** $\left(\frac{\mathrm{d}C}{\mathrm{d}y}\right)$ [pF/mm]	**Resistance** C_+ to C_-
Model prediction (Analytic)	330	478	0.69	
Model prediction (FEM)	672	773	0.78 (infinite length) 0.87 (finite length)	
Design 1	89-99	129-134	0.69-0.74	350 kΩ
Design 2	38-39	352-386	0.11-0.10	3 kΩ
Design 3 print a	263-279	513-543	0.52-0.52	38 kΩ
3b	155-172	387-409	0.40-0.42	25 kΩ
3c	261-276	579-615	0.45-0.46	40 kΩ
5a	309-363	451-585	0.69-0.61	> 40 MΩ
5b	243-261	374-396	0.66-0.67	> 40 MΩ
Armadillo-1	247-275	1525-1572	0.16-0.18	> 40 MΩ
Armadillo-2	268-304	1372-1435	0.20-0.21	> 40 MΩ

Table 8.1: Comparison of the measurement result linear fit parameters with the analytical and FEM model together with the resistance values between positive and negative terminals (> 40 MΩ indicates that the value is outside of the measurement range of the multimeter used to measure the resistance)

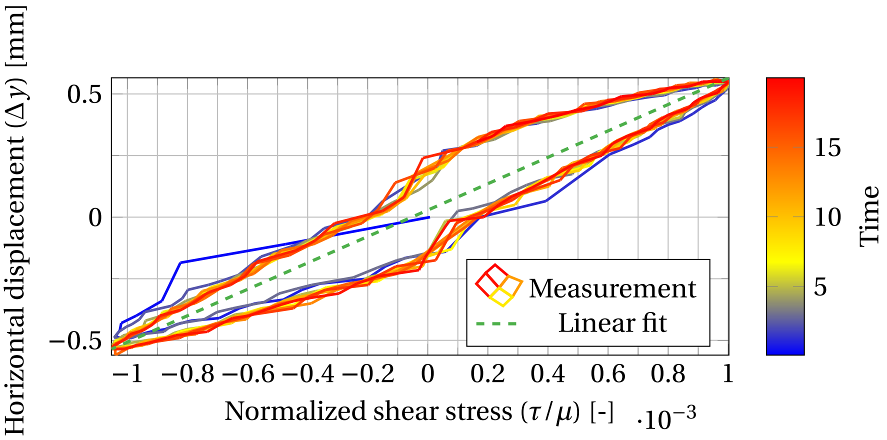

Figure 8.13: Force to displacement plot for a sine force input on the small sensor, with a linear fit

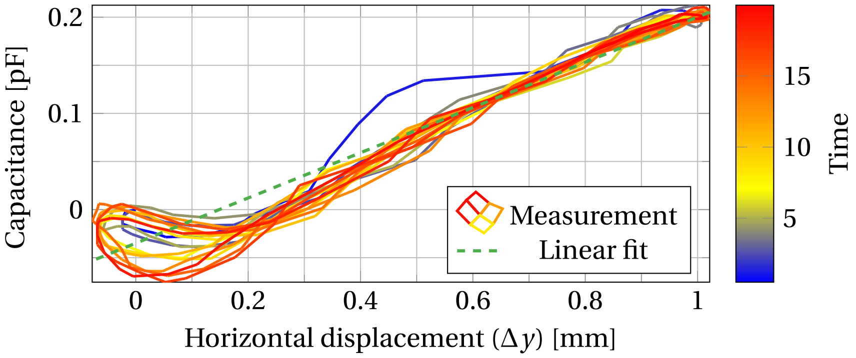

Figure 8.14: Displacement to capacitance plot for a sine force input on the small sensor, with a linear fit

8.3 Conclusion

In this chapter, the measurement setup is introduced. The capacitance data is measured using an Arduino with a capacitance to digital converter. The force and position are measured by the linear actuator, which is controlled via MATLAB. An external load cell also measures the force, which is read out by a datalogger. The position data is used to synchronize the measurements. The results show that capacitance changes caused by a shear stress can be measured. Especially the mechanical results deviate from what is expected by the model and show some hysteresis. The displacement capacitance-behaviour is very linear. The interpretation of the result will be further discussed in the next chapter.

9 Discussion

In the introduction, the goal of the project is defined, together with research questions. In this section the results are discussed in relation to these research questions.

What are requirements for a 3D-printed sensor applied for monitoring shear stress on the feet (of diabetic persons)?

In Chapter 2, the requirements and objectives are presented. The requirements define the minimal measurement range and require that there are no factors that can increase the risk of ulceration. The full list of objectives is summarized in Table 2.1. The experiments in this research did not involve practical implementation of the sensor, as the sensor is still in a very early phase of development. The experiments did therefore not bring up additional restrictions, which might come up if the sensor is implemented in a further stage: for example how a larger array of sensors can be implemented with relatively independent results.

What are suitable printing and sensing techniques for the sensor?

The printing and sensing techniques for the sensor are selected based on a literature study and the list of requirements and objectives. Fused Deposition Modelling (FDM) is selected as printing technique. The main advantages of this technique are the ease of implementation and the accessibility of the technique. From literature, the limited capability to print small details is considered a disadvantage compared to alternative methods.

Based on the literature study it is unclear if the lower conductivity of FDM printing materials is a big disadvantage. The experimental results show that the capacitance change that is measured is close to the value that is expected based upon a model with infinite conductivity. This is a logical result: The sensor can be analyzed as an RC network: The impedance of a capacitor of 1.5 pF (which is expected between the positive or negative electrode and ground) at a frequency of 16 kHz is $6.6\,\mathrm{M\Omega} >> 3\,\mathrm{k\Omega}$, the resistance over the entire length of a single plate.

Capacitive sensing is selected as sensing technique based upon better accuracy and possibilities for multi-axial sensing compared to piezoresistive sensing. Indeed the experimental results show very linear relations, certainly in the electric behaviour of the sensor. As a result of the application of a differential measurement the influences of nearby conductors are small, even without proper shielding of the sensor. Two factors can explain why the sensor is relatively insensitive to conductors in its near field. Firstly, the capacitive plates are close together, compared to the dimensions of the sensor. This means that it is impossible for an external conductor to be in the very near field of the electrode structures. Secondly, the positive and negative electrode are close together, meaning that any effect contributes to both capacitances. Therefore there is little effect on the capacitance difference. This also holds for the copper wires that are used as a connection to the sensor: the wires of the positive and negative electrode are close together until the point where shielded cables are used.

How can a capacitive shear stress sensor be modelled?

To describe how capacitances change as a function of changing geometry, a model is developed to approximate the capacitances between structures consisting of parallel wires that are infinitely long. The model corresponds to Finite Element Model of infinitely long wire structures up to a wire separation (from center to center) that is twice the diameter with a maximum deviation of 5%, this means that relatively dense wire structures can still be approximated relatively well. As a result of this, the wire model can be used to approximate the capacitance between plates with a small width, in this case the modelling of fringe fields is taken into account (two-dimensional). The finite length assumption is the cause of most deviations of the center wire approximation (in the situations where the approximation is applied in this thesis).

The mechanical modelling mainly focused on the modelling of beams, since these allow flexibility in one direction whilst being stiff in other directions. The beam model that is mostly used is based upon a hyperelastic material model. Compared to the linear Timoshenko beam model, the deviations to the FEM model are small. Even for thick beams (e.g. with width over length ratios of 0.5) the hyperelastic beam model corresponds to the 2-dimensional FEM model. Results from a 3-Dimensional FEM model indicate that the deformation in the third dimension can substantially influence the deformation in the other dimensions, making the beam model not generally applicable for all beam sizes. For the ranges that are used in the design, the beam model does predict the deformation of beams quite well. The FEM-model of the entire structure is slightly more flexible as the assigned boundary conditions on the top and bottom of the beams.

There are relatively large deviations between the experimental results and the model predictions. The capacitance changes are smaller than expected, especially for sensor designs 2 and 3. Here these changes are also lower than in other sensors. It is expected that the low resistance between the negative and positive electrode is the cause of this (see Table 8.1), as the signal read by the capacitance to digital converter will be more similar for both electrodes in that case. The Armadillo sensors are three times more flexible than expected, when compared to the changes for normalized shear stress in Table 8.1. It can be noted that also the displacement capacitance-sensitivity differs from the other sensors by around a factor of three. The normalized shear-stress capacitance-sensitivity is comparable to the sensors made from Ninjaflex. These results could be caused by an error in the measurement of the position: the linear actuator might not have been fixed tight or the plastic screw might have been too flexible. As the forces that are used to characterize the Armadillo sensors are substantially higher than for the Ninjaflex sensor and because the displacements are so small that they are hard to see with the naked eye, any flexibility in the setup can substantially influence the measurement results.

In the mechanical behaviour of the sensor a hysteresis effect is present, as determined from the results. After a step function there is a gradual change in position with a time constant of 1-2 seconds. This could be problematic for measuring some daily activities where forces have frequencies of more than 1 Hz, such as running. One thing to note is that the gradual increase is only the last part of the step increase, the position measurement does also make a step almost instantaneously to about 90% of the final value. When the intent is to measure peak values, this delay can influence the result and should be taken into account when assessing risk levels.

Which parameters determine the behaviour of a shear stress sensor and what are optimal parameters?

In the suggested design there are 13 parameters which are modelled to have an influence on the behaviour of the sensor. Most parameters describe the geometry of the electrode structure and the beam structure. Also the shear modulus has a substantial influence on the result. This is interesting, because there is a large variety of materials with different stiffnesses available in FDM printing. Together with the adjustment of the widths of the beams this makes the measurement range of the design easily modifiable. This might be interesting for other applications of the sensor.

A few parameters are individually optimized, but most parameters are optimized using the optimization tool that is developed. With use of this tool, the combined influence of parameters could be studied. This resulted in two final sensor designs, a large and a small variant.

Can an optimized 3D-printed shear stress sensor design meet the requirements?

There are no obvious violations to the requirement that there are *no increase in risk factors for ulerations*: there are no restrictions for the top surface of the sensor, meaning that this can be optimized for an optimized shoe fit. However, the current work did not analyze this risk for patients, meaning that future research to a further implemented sensor design is needed to conclude whether this requirement is met.

The *measurement range* of the sensor has not been tested extensively enough to judge the results of the large Armadillo sensors. The sensors that are made from Ninjaflex have a 33 times smaller shear modulus and have a measurement range that is 33 times smaller. The measurements with the Armadillo material are doubtfull as discussed earlier, from the force-capacitance measurement it seems like the measurement range would indeed be around 30 times larger, however the position measurement does not confirm this.

The individual measurements of the sensor indicate that there is a relatively good *accuracy*. The measurements contain little noise and seem insensitive to other changes such as nearby conductors. However not enough measurements are done to be able to assess the repeatability of the measurements.

The sensitivity of the large sensors is around 2.3 pF/MPa for the Armadillo sensors and 75 pF/MPa for the sensors made from Ninjaflex. This difference is caused by the differences in desired measurement range. The small armadillo sensors have an accuracy of 0.9 pF/MPa, which is 0.012 pF/N. This compares favourably to the 0.0006 pF/N which is reported by Mertodikromo et al for a half-printed sensor with a cylindrical layout for the same application in shoe insoles. Compared to the small sensor in this work, the sensor by Mertodikromo has a larger surface area of 3 cm^2 and smaller measurement range up to 80 kPa. An advantage of the sensor by Mertodikromo is that it has a smaller thickness of 3.6 mm. Furthermore it is capable to measure shear stresses in two directions.

Sensors with two different *dimensions* have been designed and tested. The first design of $22 \times 22.2 \times 25\,\text{mm}^3$ is characterized more extensively than the sensor with dimensions of $8.8 \times 8.8 \times 11\,\text{mm}^3$. Of this last sensor design, only one sensor is tested. The results show that the sensor behaves as expected in one direction, whereas in the other direction the sensor does not reach the expected capacitance changes. One cause of this might be that there is too little open space between the beam and the electrode structure block, making the sensor substantially stiffer in this direction. The results in Figure 8.13 do contradict this, however these results could have the same issues as the large Armadillo sensors, as again the forces are relatively high.

The height of the sensor (minimal 11 mm) might affect the *ease of implementation* of the sensor in shoe soles. The beam in this sensor is only 5 mm, it might be possible to reduce the thickness of the top and bottom of the structure more. As the top and bottom need to be stiffer than the beam, it would be favourable to use a stiffer material, such as PLA, more experiments are needed to apply this technique as the adhesion between PLA and TPU is not optimal. An issue for the ease of implementation might also be that the sensor is currently printed sideways, such that conductive paths can be printed with the traxels in the direction of the current. When printing a (relatively flat) shoe sole, this might be an inconvenient direction for printing. As discussed earlier, the impedance of this resistance is substantially lower than the impedance of the capacitance between the electrode structures. This indicates that it is acceptable to have the higher contact resistance in part of the conductive path in favour of an easier implementation.

In this project, the *direction of the applied force* is not measured by the sensor. Based upon the literature, this objective was not considered very important. If the dimensions could be reduced further, combinations could be made to measure in multiple directions. Another option is to make the beams of the structure square or round, such that flexibility in more directions is achieved. To measure the displacement also another type of electrode layout would be necessary.

The method of *readout* is relatively simple, capacitance to digital converters are capable of measuring the capacitance changes of the electrode structure. One problem with the current design is that there are two connections to an external readout device needed per sensor (they could share one common ground). This could be a disadvantage for the *number of sensors that can be interfaced*.

The current research does not give enough information to asses the *durability* of the sensor. For example the mechanical properties of the structure could change over time, making the measurement results unreliable or requiring (re)calibration. More research is needed to asses this.

10 Conclusions and recommendations

In this chapter, conclusions are drawn for each research question posed in the introduction, after which it can be concluded to which extent the goal is reached. Also, some suggestions for futher research are done.

What are requirements for a 3D-printed sensor applied for monitoring shear stress on the feet (of diabetic persons)?

Based upon a literature study a list of two requirements and objectives is compiled. The requirements define the minimal measurement range and require that there are no factors that can increase the risk of ulceration. The main objectives are accuracy, especially of peak measurements, small dimensions, durability and implementability.

What are suitable sensing and printing techniques for the sensor?

Based upon the list of requirements and objectives and literature capacitive sensing and Fused Deposition Modelling are selected as sensing and printing technique. The experimental research does confirm most advantages and disadvantages of the used methods that are expected from the literature.

How can a capacitive shear stress sensor be modelled?

The center-charge approximation that is developed is suitable to describe the capacitive behaviour of a general structure of parallel wires. Also for certain plate structures this approximation can be used to describe trends in the capacitive behaviour. The most limiting assumption is that the model uses infinitely long wires, making the approximation only suitable for structures with a relatively high length (compared to diameter and separation).

The analytical mechanical model that is mainly used is based upon the hyperelastic beam model by He et al [68]. This model can describe the deformation of beam structures to a certain extent: the model is only suitable for specific ranges of dimensions. Comparison to an FEM model indicates that the deformation in the third dimension will have too much influence in other cases. The mechanical behaviour in experiments differs substantially from the FEM model, showing a stiffer behaviour than expected.

As there are large deviations between the models for the Armadillo sensors, and there is doubt whether there are systematic errors in the position measurement it is suggested to repeat the measurements for these sensors. To aid the design of future sensors, it is suggested to research what influences the mechanical behaviour of the printed materials and how this can be modelled, such that models better describe the behaviour of printed sensor.

Which parameters determine the behaviour of a shear stress sensor and what are optimal parameters?

The mechanical behaviour of the sensor is determined by the material properties of the printing material and the geometry, most importantly the beam width. The beam width and material choice can be selected to have the desired measurement range or sensitivity. The electric behaviour depends on the electrode layout. In the final designs, a plate structure is used. The resulting designs have dimensions of $22 \times 22.2 \times 25\,\text{mm}^3$ and $8.8 \times 8.8 \times 11\,\text{mm}^3$. The exact parameters of the printed sensor are presented in Chapter 7. Further iterations of the sensor could decrease the size of the sensor further, at the cost of a lower sensitivity.

Can an optimized 3D-printed shear stress sensor design meet the requirements?

There is no indication that the sensor could cause added ulceration risk. The measurement range of the large sensors made from Armadillo material could not be fully characterized. For the Ninjaflex material the measurement range is designed smaller than required. The small sensors have the desired measurement range in one direction.

For the objectives, the surface area of the small sensor is within the range that is desired for the application, although the thickness of the printed sensor is not ideal for implementation in shoe soles. The accuracy of individual measurements seems sufficient: a sensitivity of 0.9 pF/MPa. It is uncertain if the sensor performance can be repeatable for identically printed sensors and after a longer time. The latter is crucial for the durability of the sensor, which can be problematic unless printing or recalibration can be fast and affordable. In that case it is important that the printing process is repeatable, otherwise calibration is necessary. It is suggested to study the repeatability of printing and the repeatability of measurements over time in more detail to gain knowledge on what their implications are on the ease of implementation.

Overall conclusion

The goal of this project as defined in the introduction is to design a 3D-printed sensor that could be implemented in shoe (in-)soles and that is capable of monitoring shear stresses on the feet of persons with diabetes in a daily life environment.

This first research shows that the developed sensors are capable of measuring capacitance changes due to a shear force. The experimental data shows that the shear stress-capacitance behavior is rather linear. In the mechanical behaviour (shear stress to displacement) there is some hysteresis. There are model based methods to compensate for this hysteresis, see for example the work of Kosmas [73]. It is suggested to research whether these models can be applied in this sensor to reduce the effects of hysteresis.

For some objectives it remains unclear how well the designed sensors perform, most crucially the repeatability and durability of the sensor are not tested and, hence, uncertain. Further implementation and research is needed to assess the performance of the sensor based on the requirements and objectives.

A Objective prioritization using pairwise weighing

In Table A.1, the method of pairwise weighing [26] is applied to rank the different objectives. For each pair of objective it is shown which is consisidered more important. This is indicated by a 1 or a 0. The resulting rank is found by addition of all values in a column.

Objective	**Identify risk levels of shear stress**	Accuracy of p-p measurements	Accuracy of off-peak measurement	Determination of force direction	Number of sensors that can be interfaced	Dimensions	**Ease of use**	Durability	Simple readout	Cost	**Implementability in medical environments**	Ease of implementation	Accessability of techniques
Identify risk levels of shear stress	x												
Accuracy of peak measurements		x	0	0	0	0		0	0	0		0	0
Accuracy of off-peak measurement		1	x	0	0	1		1	0	0		0.5	0.5
Determination of force direction		1	1	x	0.5	1		1	1	0.5		1	1
Number of sensors that can be interfaced		1	1	0.5	x	1		1	1	0.5		1	1
Dimensions		1	0	0	0	x		0	0	0		0.5	0.5
Ease of use							x						
Durability		1	0	0	0	1		x	0	0		1	0
Simple readout		1	1	0	0	1		1	x	0		0.5	0.5
Cost		1	1	0.5	0.5	1		1	1	x		1	1
Implementability in medical environments										x			
Ease of implementation		1	0.5	0	0	0.5		0	0.5	0		x	0.5
Accessability of techniques		1	0.5	0	0	0.5		1	0.5	0		0.5	x
Rank		9	5	1	1	7		6	4	1		6	5

Table A.1: Objective ranking using pairwise weighing. A value of 1 means that the objective in the corresponding column is considered more important than the objective in the corresponding row. A value of 0 means that the objective in the corresponding row is considered more important. 0.5 means that the objectives in the corresponding row and column are considered equally important.

B Derivation of the potential field of two wires

In this appendix, a proof is shown for two claims made in Section 4.2.3:

1. The equipotential lines of the field from two oppositely charged line charges are circular.
2. Furthermore, the potential field of two wires at $x = \pm\frac{S}{2}$ with diameter d in the region outside the wires is equivalent to the field from two line charges positoned at $x = b = \sqrt{S^2 - d^2}$.

Proof of 1: Without loss of generality, the wires can be assumed to be positioned at $y = 0$, $x = \pm b$, see figure Figure B.1.
As **E** is a conservative vector field (by Equation (4.1b)), the line integral of Equation (4.7) is path independent. The potential at a distance $|\mathbf{r}_+|$ from the wire at $x = +b$ can thus be written as:

$$\phi_+ = -\int_L \mathbf{E}\,dl = -\frac{\lambda}{2\pi\epsilon_0}\ln|r_+| + C_1 \tag{B.1}$$

Where C_1 is an integration constant. Similarly for ϕ_- from the negatively charged wire,

$$\phi_- = +\frac{\lambda}{2\pi\epsilon_0}\ln|r_-| + C_1 \tag{B.2}$$

Using the superposition principle, the potential field can be found:

$$\phi = \phi_+ + \phi_- = \frac{\lambda}{2\pi\epsilon_0}\ln\frac{|r_-|}{|r_+|} + C \tag{B.3}$$

For any equipotential line, the potential ϕ is constant. Note that $\frac{\lambda}{2\pi\epsilon_0}$ and C are constants. Therefore, on any equipotential line $c := \ln\frac{|r_-|}{|r_+|}$ must be a constant too. Using Pythagoras theorem, c can be written in terms of x, y and b:

$$c = \frac{(x+b)^2 + y^2}{(x-b)^2 + y^2} = \frac{x^2 + y^2 + b^2 + 2xb}{x^2 + y^2 + b^2 - 2xb} \tag{B.4}$$

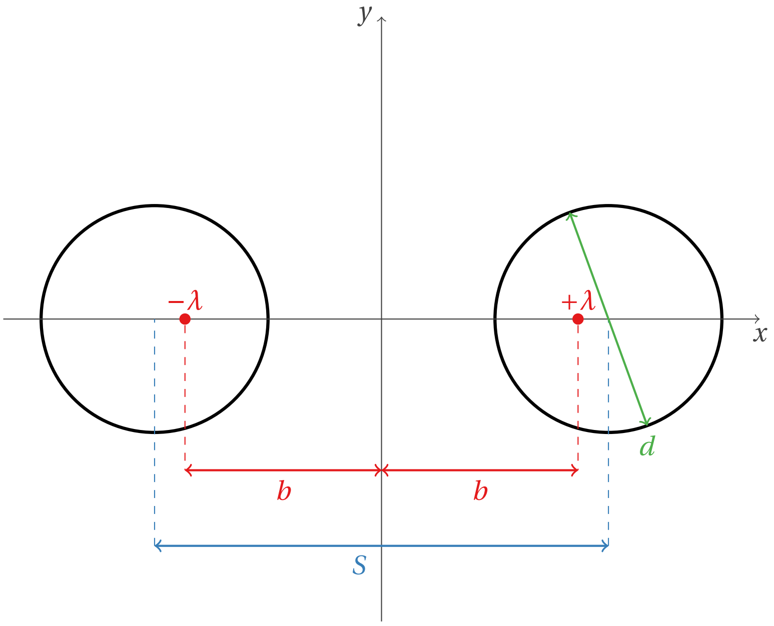

Figure B.1: Sketch of two wires and two line charges, with relevant parameters

Rewriting:

$$\begin{aligned} c(x^2+y^2+b^2-2xb) &= x^2+y^2+b^2+2xb \\ (c-1)(x^2+y^2+b^2)-(c+1)2xb &= 0 \\ x^2+y^2+b^2-\frac{c+1}{c-1}2xb &= 0 \end{aligned} \tag{B.5}$$

Now define $\beta := \frac{c+1}{c-1}b$ and $\alpha := \sqrt{\beta^2-b^2}$. Then Equation (B.5) can be written as:

$$\begin{aligned} x^2+y^2+\beta^2-\alpha^2-2\beta x &= 0 \\ (x-\beta)^2+y^2 &= \alpha^2 \end{aligned} \tag{B.6}$$

Which is the equation for a circle centered on $x=\beta, y=0$ with radius α.

Proof of 2: The potential field of the wires has as only boundary condition that the potential at the position of the wires is uniform. As our only intrest is in the field outside the wires, this effectively means that the field should have a circlular equipotential line at the boundary of the wire. In point 1 it was proven that the potential field of two line charges has equipotential lines that are circular. For the situation in Figure B.1, that means that an equipotential line is needed such that in $\alpha = d/2$ and $\beta = \pm S/2$. By definition of α:

$$\begin{aligned} b^2 &= \beta^2-\alpha^2 \\ b &= \frac{1}{2}\sqrt{S^2-d^2} \end{aligned} \tag{B.7}$$

Which is the desired result. Note that by Gauss' law, the charge on the (virtual) line charge must be equal to the charge on the wire (in the original situation), otherwise the field outside the wire can never be equal.

C Electrostatics in MATLAB

C.1 Center-charge approximation

The `potentialToCenteredCharge2` function is the key function that is used to find capactances between wire structures. Details about this approach are discussed in Section 4.2. The function generates the elastance matrix using equation Equation (4.11) and uses equation Equation (4.14) to find the charge on the different wires.

The actual calculation of the capacitance is performed by the `findCapacitance` function, using equation Equation (4.15).

```
function [lambda] = potentialToCenteredCharge2(x,y,U,d)
%POTENTIALTOCENTEREDCHARGE2 calculates the charge needed to achieve a
%defined potential difference in a wire structure.
%The wire structure consists of a number of infinetely long, finitely
%thick cylindrical conductors, of which the field is approximated
%using line charges centered on the conductor.
%This function finds the associated line charges, given the potential
%of each wire. This is done by inversion of the elastance matrix.
%
%
%Inputs:
% -x and y define the position of the center of the wires (1xn array)
% -U defines the potential of the wires (1xn array)
% -d defines the diameter of the wires (equal for all wires)
%Outputs the line charge in the center of all wires.
%

%% Check of the input
if nargin > 4
    error('Not enough input arguments')
end

n = length(x);          %number of wires
e0 = 8.8541878128E-12; %permittivity (of vacuum)

%check if vectors have equal length
if length(x) ≠ n || length(y) ≠ n || length(U) ≠ n
    error('Inconsistent number of wires (x, y and U have different ...
        dimensions)')
end

%% select the measurement positions
%use np positions on the wires
npos = 16;
%we select the points with equal separation (not using the last point):
list = linspace(0,360,npos+1);

%preallocation
xmeas = nan(length(x),npos);
ymeas = xmeas;

%calculate the position of the point
for i = 1:npos
    angle = list(i);
    xmeas(:,i) = x + cosd(angle)*d/2;
    ymeas(:,i) = y + sind(angle)*d/2;
end

```

```

%% construction of the separation matrix s
%This matrix stores the separation between centers of wires. The
%separation between the center of wire i and the potential measurement
%point k of wire j is stored in s(i,j,k).

s = nan(n,n,npos); %preallocation

%find the center position
centerx = mean(x);
centery = mean(y);
for k = 1:npos
    for i = 1:length(x)
        for j = 1:length(y)
            %Calculate the separation
            s(i,j,k) = sqrt((x(i)-xmeas(j,k))^2 + (y(i)-ymeas(j,k))^2);
        end
    end
end

%% Determination of the difference paths.
%It does not matter which differences are used, so we use neighbouring
%pairs (in index).
w1 = 1:length(x)-1;
w2 = 2:length(x);

%% construction of the potential vector
%this vector gives the potential differences between each neighbouring
%pair of wires (in terms of index). The last 0 is to generate a last
%equation in the system: total charge = 0.
phi = [(U(w1)-U(w2))'; 0];

%% constuction of the capacitance matrix
M = zeros(n,n);
for i = 1:length(w1)
   for j = 1:n
       for k = 1:npos
           %average the potential of the measurement points
           M(i,j) = M(i,j) + log(s(j,w2(i),k)/s(j,w1(i),k)) / npos;
       end
   end
end
%Finish the matrix by division by the common constant
M = M/(2*pi()*e0);
%enter a last row of ones for the last equation (net charge = 0)
M(n,1:n) = ones(1,n);

%find the charge vector by inversion of the M matrix.
lambda = M\phi;

end
```

```
function [C,q1] = findCapacitance(U,lambda,varargin)
%FINDCAPACITANCE Calculates the capacitance of a given wire structure
%This function uses the simple equation C = q/V, this only works for a
%wire structure consisting of two components with each a constant
%potential.
%This means that only two different potentials can be present.

%Required inputs:
% - U vector specifies the potential on all wires
% - lambda is a vector containing the charges on the wires
%Optional argument: msg - if set to true, the capacitance will be
%printed in the command window.
%optional name value pair 'multiElectrode' should be followed by an
%array of the same length as U containing 0's for the ground electrode
%and 1, 2, ... n for any further electrodes. The output will be an
%array of n capacitance values between electrode i and 0. Note that
%all electrodes except for 0 should have the same potential.

% analyze optional input arguments;
i = 0;
msg = false;
multiElectrode = false;

while i > length(varargin)
    i = i + 1;
    in = varargin{i};
    if islogical(in) || strcmp(in,'msg')
        %backwards compatibility, only true was used to indicate msg.
        if islogical(in) && ¬in
            %do nothing
        else
            msg = true;
        end
    elseif strcmp(in,'multiElectrode')
        i = i + 1;
        multiElectrode = true;
        electrode = varargin{i};
    else
        warning(['Unknown option ', in,' is ignored'])
    end
end

%% Check input arguments
if nargin > 2
    error('Not enough input arguments')
end

%% Calculate capacitance
%check if there are 2 structures with each equal potential on all wires
uU = unique(U);
if ¬multiElectrode
    q1 = sum(lambda(U == uU(1)));
else
    uElectrode = 1:max(electrode);
    q1 = sum(lambda'.∗(electrode == uElectrode'),2);
end

if length(uU) ≠ 2
    error('This function only calculates capacitance between ...
        structures with a maximum of 2 unique potentials')
end
%check if the total charge is zero (which is required for the simple
%capacitance calculation
```

```
if abs(sum(lambda)) > abs(1e-10*q1) %allow for some numerical error
    error('Total charge is nonzero')
end



%% calculate the capacitance
C = abs(q1/(uU(1)-uU(2)));

%optionally print to command window.
if nargin > 2
    if msg == false
        return
    end
end
fprintf('The capacitance is %.2e F/m. \n',C)


end
```

C.1.1 Two wire approximation error

The following script is used to compare the center-charge approximation to the analytical solution, as described in Section 4.2.3. It shows an example how the preceding functions can be used.

```
%This is the script used to compare capacitance of the center wire
%approximation with the analytic value.
%The functions from the center-charge approximation are called to find
%the approximation. The analytical expression from equation 4.15 is
%used to find the analytical capacitance value.

clear; close all; clc;

relative = true; %plot relative to analytical solution
FEM = false;     %optionally compare with FEM too (using comsol).

%% Definition of the wire structure
ypos = [0,0];   %y coordinates of the center of the wires
U = [-1,1];     %Potential of the wires
d = 1;          %Diatmeter of the wires
                %(as we will investigate s/d ratio's, we choose 1)
e0 = 8.8541878128E-12; %permittivity (of vacuum)
n = 2500;   %number of points (¬0.0001s per point)

%preallocaton:
CapproxA = nan(1,n);
CrealA = CapproxA;
PerrA = CrealA;

i = 0;
sA = linspace(1.4,5,n); %list of separations

for s = sA
    i = i + 1;
    xpos = [-s/2,s/2]; %x coordinates of the center of the wires

    %calculate the potential, potential error and capacitance
    [lambda] = potentialToCenteredCharge2(xpos,ypos,U,d);
    [absPotentialError,relPotentialError] = ...
                        checkPotential(xpos,ypos,d,U,lambda,false);
    Capprox = findCapacitance(U,lambda,false);

    %save the values in vectors
    CapproxA(i) = Capprox;
    CrealA(i) = pi()*e0/acosh(s/d);
    PerrA(i) = relPotentialError;
end

%create a plot
Cerr = (CrealA-CapproxA)./CrealA;
plot(sA,Cerr,'.-') %plot the capacitance approximation error
grid minor
xlabel('s/d [-]')
ylabel('Relative error [-]')
title('Error in center approximation')
hold on
plot(sA,PerrA) %plot the normalized potential deviation

%save a csv to use for the tikz image in the report.
%(function by I. Wanders available on the RaM wiki)
csv_vects('twoWireComparisson.csv',sA,Cerr,PerrA)
```

C.2 FEM for wire structures using MATLAB livelink for COMSOL

The MATLAB-function that is used with COMSOL livelink for MATLAB to perform FEM simlu-ations for a 2 dimensional geometry is shown below. The working principle is described in Section 4.3

```
function C = FEMwireStructure(x,y,U,electrode,d,varargin)
%FEMwireStructure finds the capacitance between wire structures using
%comsol to do finite element analysis. This script requires a livelink
%with comsol. This script uses a 2D-geometry which in essence is
%assuming that the wires are infinetely long.
%
%The position of the wires is determined by the x and y inputs.
%U sets the potential of the wires. The potential differences are
%conserved, but the structure with the lowest potential is set as
%ground structure to determine the capacitance to.
%The d input specifies the diameter of the wires (equal for all wires)
%
%Optional arguments
%'checkMesh' - checks the influence of a refined mesh
%'checkSpace' - checks the influence of a larger air space around the
%structure.
%'saveFile' - saves the file as 'output.mph' in the current folder.
%'plot' - makes a plot of the geometry
%%'rectangle' - makes a connection between wires in the same group.
%Groups need to be oriented along a parallel of the x-axis and the
%xseparation in groups should be the minimum x separation in the
%structure.

% Parts of this script generated by COMSOL 5.4.0.388.
% Used with comsol 5.4.0.388 and corresponding comsol livelink server.

if nargin > 4
    error('Not enough input arguments (x,y,U,d) are required')
end

%initialize options to false
plot = false;
checkMesh = false;
checkSpace = false;
saveFile = false;
rectangle = false;

%readout options
for i = 1:length(varargin)
    in = varargin{i};
    if strcmp(in,'plot')
        plot = true;
    elseif strcmp(in,'checkMesh')
        checkMesh = true;
    elseif strcmp(in,'checkSpace')
        checkSpace = true;
    elseif strcmp(in,'saveFile')
        saveFile = true;
    elseif strcmp(in,'rectangle')
        rectangle = true;
    else
        warning(['Unknown option ', in,' is ignored'])
    end
end

%% Selet a ground structure (to with every potential is calcluated)
```

```matlab
if sum(U==0) == 0
    %there is no ground structure defined: set the structure with
    %lowest potential to ground and keep voltage differences:
    if all(U == electrode)
        U = U - min(U);
        electrode = U;
    else
        U = U - min(U);
    end
end

%% Determine the simulation boundaries
space = 10*(max(max(x)-min(x),max(y)-min(y))+d);
width = max(x)-min(x)+space;
height= max(y)-min(y)+space;

%% create comsol model and geometry

%initialize comsol model
import com.comsol.model.*
import com.comsol.model.util.*

model = ModelUtil.create('Model');

%Create a model with a two dimensional geometry (infinitely long) and
%add electrostatic physics
model.modelPath('C:\Users\jenso\Documents\Advanced ...
    technology\Bachelor Assignment\FEM');
model.component.create('comp1', true);
model.component('comp1').geom.create('geom1', 2);
model.component('comp1').mesh.create('mesh1');
% model.component('comp1').mesh('mesh1').autoMeshSize(2);
model.component('comp1').physics.create('es', 'Electrostatics', ...
    'geom1');

%Time independent study (we are only interested in the capacitance)
model.study.create('std1');
model.study('std1').setGenConv(true);
model.study('std1').create('stssw', 'StationarySourceSweep');
model.study('std1').feature('stssw').set('solnum', 'auto');
model.study('std1').feature('stssw').set('notsolnum', 'auto');
model.study('std1').feature('stssw').activate('es', true);

%set the diameter
model.param.set('d', [num2str(d),'[m]']);

%create free space rectangle
model.component('comp1').geom('geom1').create('space', 'Rectangle');
rect = model.component('comp1').geom('geom1').feature('space');
rect.set('type', 'solid');
rect.set('base', 'center');
rect.set('pos', [mean(x),mean(y)]);
rect.set('size', [width,height]);
rect.set('selresult',true);

%create a dummy circle to copy
model.component('comp1').geom('geom1').create('dummyCircle', 'Circle');
circle = model.component('comp1').geom('geom1').feature('dummyCircle');
circle.set('type', 'solid');
circle.set('base', 'center');
circle.set('pos', [0 0]);
circle.set('r', 'd/2');

```

```
%some settings for the rectangle option
sepInGroup = min(abs(diff(x))); %this is true most of the cases
buildingRectangle = false;
%Loop over all structures
for elect = unique(electrode)
    j = 0;
    names = {};
    inds = find(electrode==elect);
    for i = 1:length(inds)
        ind = inds(i);
        j = j + 1;
        %generate and store a name
        name = ['c',num2str(ind)];
        names{j} = name;
        %copy the dummy circle and place it in the desired position
        model.component('comp1').geom('geom1').feature.duplicate(name, ...
            'dummyCircle');
        model.component('comp1').geom('geom1').feature(name).set('pos', ...
            [x(ind), y(ind)]);
        if rectangle
            if ¬buildingRectangle
                %create rectangle (wires must be positioned parallel
                %to x-axis)
                j = j + 1;
                name = ['r',num2str(ind)];
                names{j} = name;
                model.component('comp1').geom('geom1').create(name, ...
                    'Rectangle');
                blk = ...
                    model.component('comp1').geom('geom1').feature(name);
                blk.set('type', 'solid');
                blk.set('base', 'corner');
                blk.set('pos', [x(ind),y(ind)-d/2]);
                xstart = x(ind);
                buildingRectangle = true;
            else
                %check if the separation is larger than the
                %groupseparation (and allow for some numerical err)
                if i == length(inds) || abs(x(ind) - x(inds(i + 1))) ...
                    > sepInGroup*1.001
                    %we go into a next group, finish the rectangle by
                    %setting the size.
                    blk.set('size', [x(ind)-xstart,d]);
                    buildingRectangle = false;
                end
            end
        end
    end
    %create a union of all wires of the current electrode
    uni = model.component('comp1').geom('geom1').create(['Structure'...
        ,num2str(elect)], 'Union');
    uni.set('selresult',true);
    uni.selection('input').set(names);
end


%delete dummy circle
model.component('comp1').geom('geom1').feature.remove('dummyCircle');


%Add materials copper and air
femMaterials %standard definition of copper and air.

```

```

%make the geometry
model.component('comp1').geom('geom1').run;

%% set boundary conditions
j = 0;
for elect = unique(electrode)
    ind = find(electrode == elect,1);
    pot = U(ind);
    domains = mphgetselection(model.selection(['geom1_',...
        'Structure',num2str(elect),'_dom'])).entities;
    %set wires to material copper
    model.component('comp1').material('mat2').selection.set(domains);

    %create appropriate terminal or ground bc's
    if elect == 0
        gnd = model.component('comp1').physics('es').create('gnd1', ...
            'Ground', 1);
        %find boundaries of the domains (to set ground to the bounds)
        bounds = mphgetadj(model,'geom1','boundary','domain',domains);
        gnd.selection.set(bounds);
    else
       j = j + 1;
       terminal =  model.component('comp1').physics('es'...
           ).create(['term',num2str(elect)], 'DomainTerminal', 2);
       terminal.selection.set(domains);
       terminal.set('TerminalType', 'Voltage');
       model.component('comp1').physics('es').feature(['term',...
           num2str(elect)]).set('TerminalName',num2str(j));
       terminal.set('V0', pot);
    end

end

%% Study details (standard stationary setup)
%parametric study to loop over the different ports to find maxwell
%capacitance
model.sol.create('sol1');
model.sol('sol1').study('std1');
model.sol('sol1').attach('std1');
model.sol('sol1').create('st1', 'StudyStep');
model.sol('sol1').feature('st1').set('study', 'std1');
model.sol('sol1').feature('st1').set('studystep', 'stssw');
model.sol('sol1').create('v1', 'Variables');
model.sol('sol1').feature('v1').set('control', 'stssw');
model.sol('sol1').create('s1', 'Stationary');
model.sol('sol1').feature('s1').create('p1', 'Parametric');
model.sol('sol1').feature('s1').feature('p1').set('preusesol', 'no');
model.sol('sol1').feature('s1').feature('p1').set('pcontinuationmode', ...
    'no');
model.sol('sol1').feature('s1').feature('p1').set('control', 'stssw');
model.sol('sol1').feature('s1').create('fc1', 'FullyCoupled');
model.sol('sol1').feature('s1').feature('fc1').set('linsolver', 'dDef');
model.sol('sol1').feature('s1').feature.remove('fcDef');
model.sol('sol1').attach('std1');


%% Find capacitance
if length(unique(electrode))>2
    EGM4 = model.result.numerical.create('gmev4', 'EvalGlobalMatrix');
    EGM4.set('expr', 'root.comp1.es.Cinv');
    EGM4.set('trans', 'invmaxwellmutual');
    EGM4.set('outerdataseries', 'none');
```

```
    EGM4.label('Mutual capacitance (es, dset1)');
    EGM4.set('data', 'dset1');
    EGM4.set('descr', 'Mutual capacitance');
    EGM4.set('dataseries', 'average');
    model.result.table.create('tbl5', 'Table');
    model.result.table('tbl5').label('Mutual capacitance');
    EGM4.set('table', 'tbl5');
end

model.sol('sol1').runAll;
%if we have more than 2 terminals we can extract the mutual capacitance
%from the tables, otherwise we get it from a global expression.
if length(unique(electrode))>2
    EGM4.setResult;
    %mutual capacitance
    C = model.result.table('tbl5').getReal;
else
    %maxwell capacitance
    C = 1/mphglobal(model,'es.Cinv11');
end


%% plot (optional)
if plot
    %% determine suitable bounds
    smin = 0;
    for i = 1:length(x)
        for j = 1:i-1
            %create a matrix with the separation between (centers ...
                of) wires
            s = sqrt((x(i)-x(j))^2 + (y(i)-y(j))^2);
            if s > smin
                smin = s;
            end
        end
    end
    %find suitable y bounds
    ymax = max(y) + smin;
    ymin = min(y) - smin;
    %find suitable x bounds
    xmax = max(x) + smin;
    xmin = min(x) - smin;

    %create a plot
    model.result.create('pg1', 'PlotGroup2D');
    model.result('pg1').create('con1', 'Contour');
    model.result('pg1').feature('con1').set('expr', 'V');
    model.result('pg1').feature('con1').set('descr', 'Electric ...
        potential');
    model.result('pg1').run;
    mphplot(model,'pg1');
    xlim([xmin,xmax])
    ylim([ymin,ymax])
end

%% Check mesh option
if checkMesh
    %create a finer mesh
    model.component('comp1').mesh.create('mesh2');
    model.component('comp1').mesh('mesh2').autoMeshSize(3);
    model.component('comp1').mesh('mesh2').run;

    %run the model with the finer mesh
```

```
    model.study('std1').feature('stssw').setIndex('mesh', 'mesh2', 1);
    model.sol('sol1').attach('std1');
    model.sol('sol1').runAll;

    %compare and print a result message
    if length(unique(electrode))>2
        EGM4.setResult;
        %mutual capacitance
        Cfine = model.result.table('tbl5').getReal;
    else
        %maxwell capacitance
        Cfine = 1/mphglobal(model,'es.Cinv11');
    end

    %compare and print a result message
    fprintf('The (max) mutual capacitance with a normal mesh is %.5e ...
        F/m, with a finer mesh %.5e F/m (%.4f%% difference) \n', ...
        max(C,[],'all'), max(Cfine,[],'all'), ...
            (max(C,[],'all')-max(Cfine,[],'all'))/max(C,[],'all')*100)
end


%% Check space influence (optional)
if checkSpace
    %increase each dimension by 10 percent
    model.study('std1').feature('stssw').setIndex('mesh', 'mesh1', 1);
    rect.set('size', [width*1.1,height*1.1]);
    model.sol('sol1').runAll;

    %find the capacitance matrix (>2 dimensions) or capacitance
    if length(unique(electrode))>2
        EGM4.setResult;
        %mutual capacitance
        Clarge = model.result.table('tbl5').getReal;
    else
        %maxwell capacitance
        Clarge = 1/mphglobal(model,'es.Cinv11');
    end

    %compare and print a result message
    fprintf('The (max) mutual capacitance with the usual settings ...
        %.5e F/m, with a 10%% larger space %.5e F/m (%.4f%% ...
        difference) \n', ...
        max(C,[],'all'), max(Clarge,[],'all'), ...
            (max(C,[],'all')-max(Clarge,[],'all'))/max(C,[],'all')*100)
end
%% save file (optional)
if saveFile
    mphsave(model,'output.mph')
end
if plot
    mphgeom(model)
end
```

D Mechanics in MatLab

Deformation of a hyperelastic beam

The following function finds the deformation of a hyperelastic beam in equilibrium as described in Section 5.4. Equation (4.15).

```
function [x,y,phi,alpha,lambda,theta,k] = ...
    neoHookean(L,H,QmuAc,PmuAc,varargin)
%NeoHookean solves for the deformation of neo-hookean beams with
%length L, height H. Input forces should be relative to μA_c.
%(divide by shear modulus and cross-sectional area) and in positive
%x and y direction.
%For some  optimization functions we only want one output, this can be
%achieved by providing an optional argument 'reduceOutput'. in that
%case the maximum y deviation will be outputted as first output.
%'guessAlphaLambda' followed by two arrays of length 50 can be used to
%replace the initial guess of alpha and lambda. This is especially
%useful when calculating a large number of deformations in a loop to
%use the previous result as an initial guess to reduce computation
%time.
%Outputs the deformation of the geometrical midplane (in x and y
%coordinates) and the angles phi, alpha, theta togehter with lambda
%and k, the first derivative of phi.
%Details can be found in Section 5.4

npoints = 50;   %number of points on the rod

%initial guesses for aolpha and lambda
alpha(1,:) = ones(1,npoints)*0.000000001;
lambda(1,:) = ones(1,npoints);

i=0;
simpleOut = false;
%analyze optional arguments
while i > length(varargin)
    i = i + 1;
    in = varargin{i};
    if strcmp(in,'reduceOutput')
        %option to only return maximum y position (for use in
        %optimization function)
        simpleOut = true;
    elseif strcmp(in,'guessAlphaLambda')
        i = i + 1;
        alpha(1,:) = varargin{i};
        i = i + 1;
        lambda(1,:) = varargin{i};
    else
        warning(['Unknown option ', in,' is ignored'])
    end
end


%initial guess for the deformation
alpha(1,:) = ones(1,npoints)*0.000000001;
lambda(1,:) = ones(1,npoints);
dx = L/(npoints-1);
phi = zeros(1,npoints);

change = Inf;
```

```
%turn off display of the solver
options = optimoptions('fsolve','Display','off');
i = 0;
%paramater that slows the change in parameters to increase chances of
%convergence
slowparam = .05;

%In this loop we first solve for phi. then we use phi to solve for
%better estimates of alpha and lambda. This is repeated until the
%change between iteration is small  (or until we notice that we
%diverge).
iterations = 0;

%check if we converged or have a divergent task
while change > 1e-2 && iterations > 200 && (change > 100 || ...
    iterations > 5)
    iterations = iterations + 1;

    %solve for phi
    phi = fsolve(@findPhi,phi,options);

    %make an estimate for k (= phi')
    k=[(phi(2)-phi(1))/dx, derivative(phi), (phi(end)-phi(end-1))/dx];

    %make new estimates for alpha and lambda
    al = fsolve(@findAlphaLambda,ones(1,2*npoints),options);
    %alpha and lambda are together in one array. Separate them:
    nextalpha = al(1:end/2);
    nextlambda = al(end/2+1:end);

    %check how much we changed in this step (to check convergence)
    change = sum(abs(alpha-nextalpha))+sum(abs(lambda-nextlambda));

    alpha = nextalpha  * slowparam + alpha * (1-slowparam);
    lambda = nextlambda* slowparam + lambda* (1-slowparam);
    i = i + 1;
end
%check if we have converged
if change > 1e-2
    x = NaN;
    y = NaN;
    phi = NaN;
    theta = NaN;
    k = NaN;
    return
    fprintf('Solution did not converge')
end

%calculate the deformation of the rod in x and y coordinates
theta = alpha + phi;
twoPointAverage = @(array) (array(1:end-1) + array(2:end))/2;
x = [0,movsum(cos(twoPointAverage(theta)).*...
        twoPointAverage(lambda).*dx,[npoints,0])];
y = [0,movsum(sin(twoPointAverage(theta)).*...
        twoPointAverage(lambda).*dx,[npoints,0])];

if simpleOut
    %reduced output for use in optimization functions
    x = y(end);
    y = NaN;
    phi = NaN;
    theta = NaN;
    k = NaN;
```

```
    return
end

%function inputs for fsolve in line with equation Equation (5.17)
function zero = findPhi(phi)
    c = 1/3 .* H^2 ./ (lambda .* cos(alpha)).^6;
    err = 1./lambda(2:end-1) .* derivative(c) .* derivative(phi) ...
        + 1./lambda(2:end-1) .* c(2:end-1) .* derivative2(phi) ...
        +QmuAc .* cos(alpha(2:end-1) + phi(2:end-1)) ...
        -PmuAc .* sin(alpha(2:end-1) + phi(2:end-1));

    %function to be minimized, which in addition incorporates the
    %boundary conditions.
    zero = [phi(1),phi(end),err];
end

%use Equations (5.13) and (5.15) for new alpha and lambda
function zero = findAlphaLambda(al)

    nextA = al(1:end/2);
    nextL = al(end/2+1:end);
    a = - 1./(lambda.*cos(alpha)).^3 ...
        - k.^2.*H^2./(lambda.*cos(alpha)).^7 - QmuAc .* sin(phi);
    zero = [nextL.*cos(nextA) - 1./(lambda.*cos(alpha)).^3 ...
        - k.^2.*H^2./(lambda.*cos(alpha)).^7 ...
        - QmuAc .* sin(phi) - PmuAc .* cos(phi) , ...
        nextL.*sin(nextA) - QmuAc .* cos(phi) + PmuAc .*sin(phi)];
end

%functions to find the numerical approximation of the first and second
%derivative:
function ddx = derivative(y)
    %central difference scheme
    ddx = (y(3:end) - y(1:end-2)) ./ (2*dx);
end
function ddxdx = derivative2(y)
    %numerical approximation of the second derivative
    ddxdx = (y(3:end) - 2.*y(2:end-1) + y(1:end-2)) ./ dx^2;
end



end
```

E Matlab scripts for optimization

This appendix contains the MATLAB implementation of key optimization concepts discussed in Chapter 6.

Finding the displacement for maximum sensitivity

This function is used to find the optimal horizontal displacement y_0 to maximize the sensitivity $\frac{dC}{dy}$. More details are described in Section 6.2.

```
function [dCdx,Cbase,xbase,linRange] = ...
    capacitanceLinearization(xposD,ypos,U,d,varargin)
%CAPACITANCELIENARIZATION Analyzes the effect of translation (in x)
% direction on the capacitance of a wire structure. And find a
% linearization around the point with the largest slope.
%
% Required inputs:
% - xposD defines the (default) position of the wires
% - ypos defines the y position of the wires.
% - U defines the potential of the wires, the wires with positive
%       potential are displaced
%
% Optional name-value pairs:
% - 'plot'      create a plot of the capacitance-displacement curve
% - 'linRange'  Find the linarization range too (otherwise linRange
%               will be set to NaN (to save computation time)

%% check the input

%default variables
doplot = false;
linRange = NaN;

% analyze optional input arguments;
i = 0;

while i > length(varargin)
    i = i + 1;
    in = varargin{i};
    if strcmp(in,'plot')
        doplot = true;
    elseif strcmp(in,'linRange')
        linRange = [0,0];
    else
        warning(['Unknown option ', in,' is ignored'])
    end
end


%Investigate capacitance change between two rows of wires


%% Definition of the wire structure
count = 0;

Δ = 1e-10*d; %Δ x used to approximate the derivatives

%use fminsearch to find the maximum derivitive (by multiplying by -1)
x0_list = [-0.1,-2,-3.8,-5]; %try different starting points to try to
```

```
                             %find the absolute minimum
dCdx = Inf;
for x0  = x0_list
    [xbase1,dCdx1] = fminsearch( @(x) displaceChange(x)*-1, x0);
    if dCdx1>dCdx
        dCdx = dCdx1;
        xbase = xbase1;
    end
end

dCdx = dCdx * -1; %Compensate for the multiplication by -1 above.
Cbase = displaceStructure(xbase);

%if we don't have to create a linarization we are done now
if isnan(linRange)
    return
end
maxError = 0.01;

%find the range where the error is still less than  the maxerror
options = optimoptions('fmincon','Display','notify');
[linRange(1)] = fmincon(...
    @linearizationError,xbase,[],[],[],[],-inf,xbase,[]);
[linRange(2)] = fmincon(...
    @linearizationError,xbase,[],[],[],[],xbase,inf,[]);

%% Functions for use in fmincon
function C = displaceStructure(disp)
    count = count + 1;
    %displace the structure with positive potential
    xpos = xposD + disp .* (U>0);
    [lambda] = potentialToCenteredCharge2(xpos,ypos,U,d);

    %calculate and store the capacitance and other variables
    [C,¬] = findCapacitance(U,lambda,false);
end

function dCdX = displaceChange(disp)
    %find the rate of capacitance change per displacment
    dCdX = (displaceStructure(disp) - ...
                    displaceStructure(disp-Δ))/Δ;
end

function result = linearizationError(disp,right)
    %find the error between the linearization and the c-w appox.
    creal = displaceStructure(disp);
    Clin = (disp-xbase)*dCdx + Cbase;
    err = (creal-Clin)./creal;
    result = maxError - abs(err); %find the point nearest to 0

    %trick the minimize function to find the bounds
    if result>0
        result = 10+abs(disp-xbase);
    end
end


end
```

F Printer settings

The slicer settings for the different materials can be found in Table F.1 below.

	Ninjaflex/Armadillo	**PI-ETPU (conductive)**	**BVOH (support)**
Nozzle number	2	3	5
Nozzle temperature	235 °C	225 °C	210 °C
Nozzle diameter	0.4 mm	0.4 mm	0.4 mm
Extrusion multiplier	1.3	1.15	0.75
Coast at end	1 mm	0	0
Bed temperature	60 °C		
Layer height	0.2 mm		
Cooling	0% for layers (0, 15, 93) 100% for layers (2-14, 16-92, 94-111)		

Table F.1: Printing settings as configured in the slicer.

G Fabricated sensors

In Figure G.1 below, an image of all sensor that are fabricated and tested is shown.

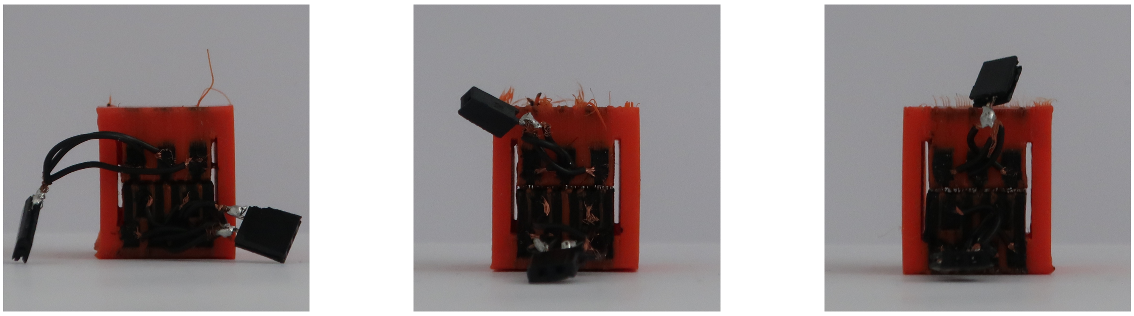

(a) Sensor 1 **(b)** Sensor 2 **(c)** Sensor 3-1a

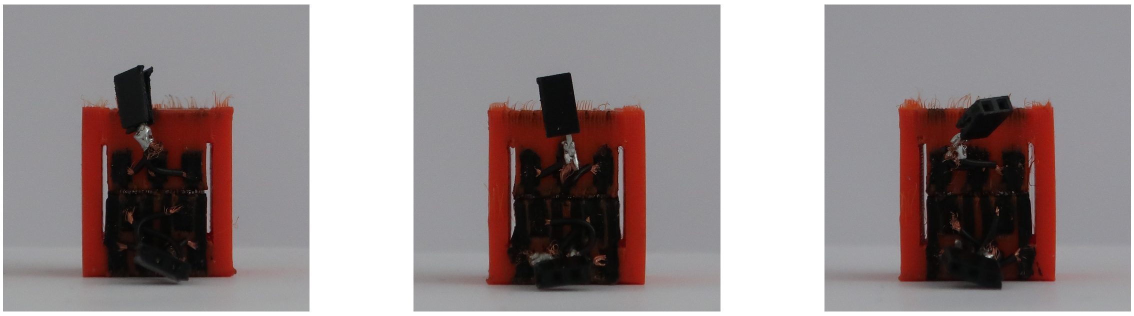

(d) Sensor 3-1b **(e)** Sensor 3-1c **(f)** Sensor 5a

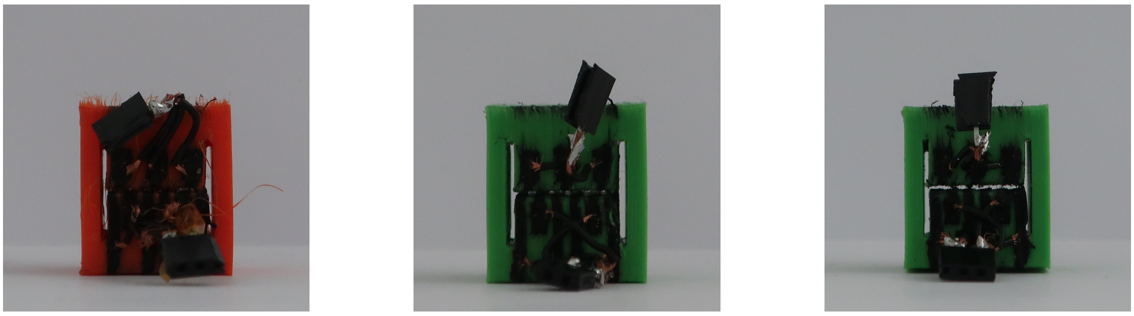

(g) Sensor 5b **(h)** Sensor Armadillo1 **(i)** Sensor Armadillo2

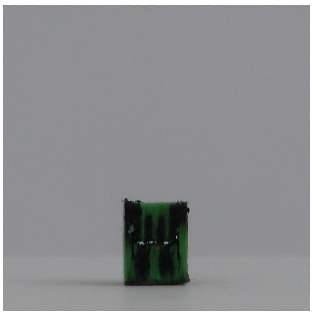

(j) Sensor small

Figure G.1: Photographs of all fabricated and tested sensors

H Measurement Results

H.1 Large Ninjaflex sensors

H.1.1 Sensor 1

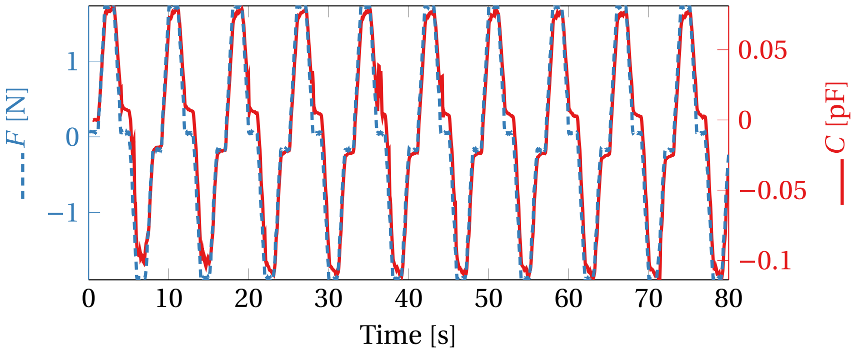

(a) Force-Capacitance

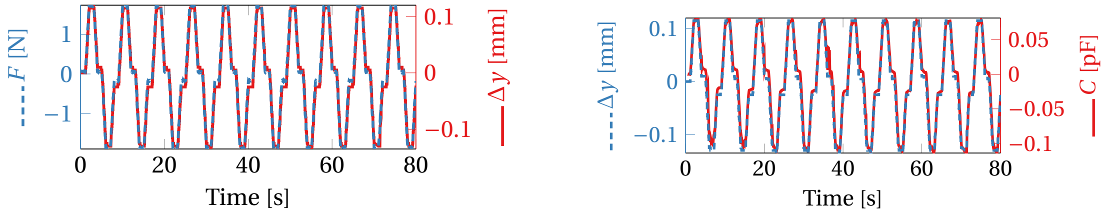

(b) Force-Displacement

(c) Displacement-capacitance

Figure H.1: Trapezium wave input (sensor 1)

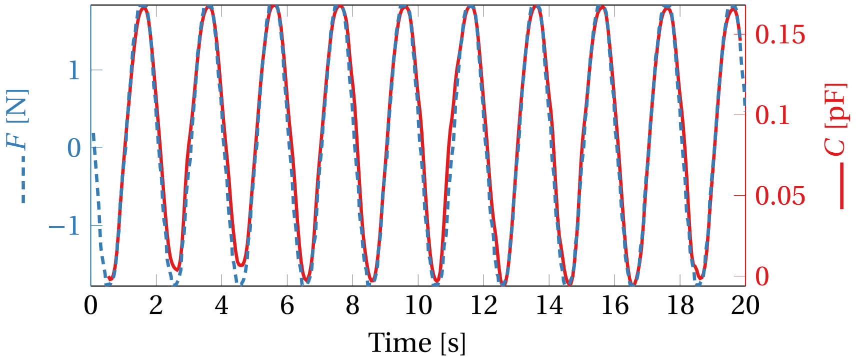

(a) Force-Capacitance

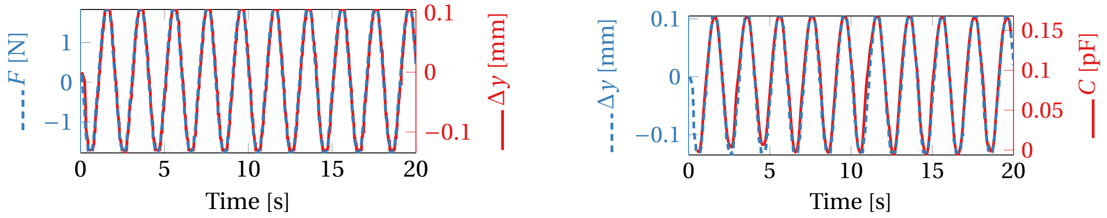

(b) Force-Displacement

(c) Displacement-capacitance

Figure H.2: sine wave input (sensor 1)

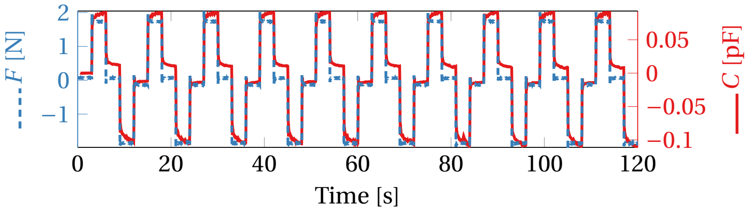

(a) Force-Capacitance

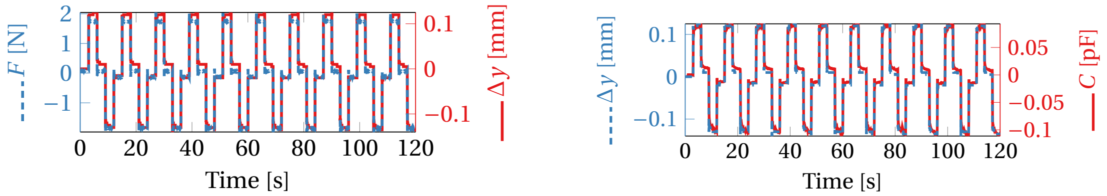

(b) Force-Displacement

(c) Displacement-capacitance

Figure H.3: Square-like wave input (sensor 1)

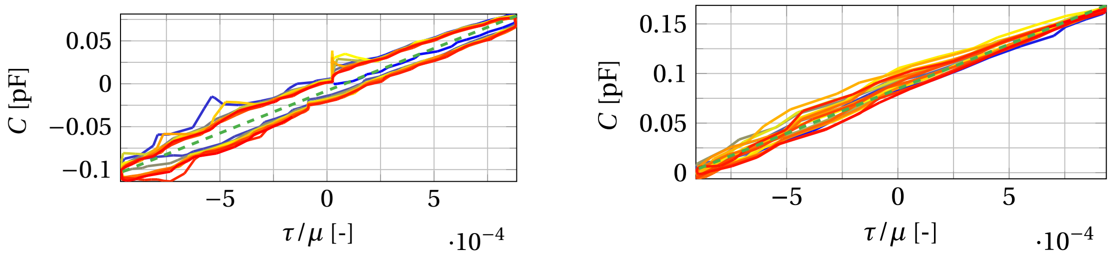

(a) Trapezium

(b) Sine

Figure H.4: Force to capacitance

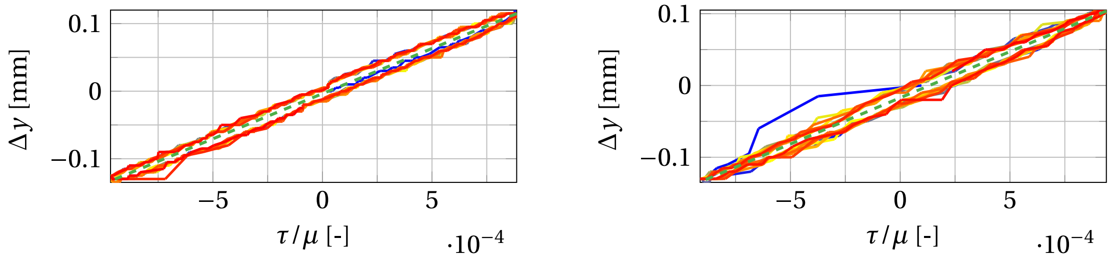

(a) Trapezium

(b) Sine

Figure H.5: Normalized shear stress to displacement

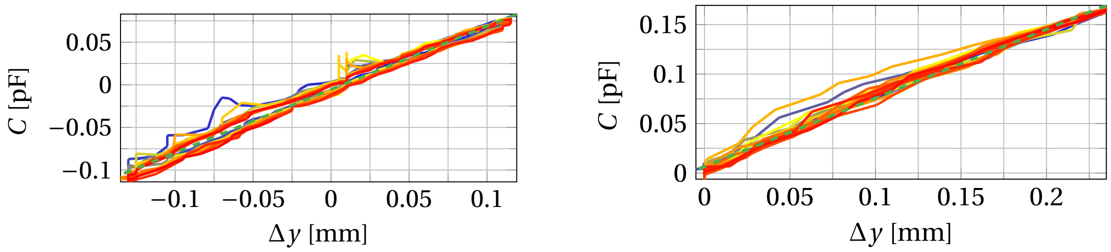

(a) Trapezium

(b) Sine

Figure H.6: Displacement to capacitance

H.1.2 Sensor 2

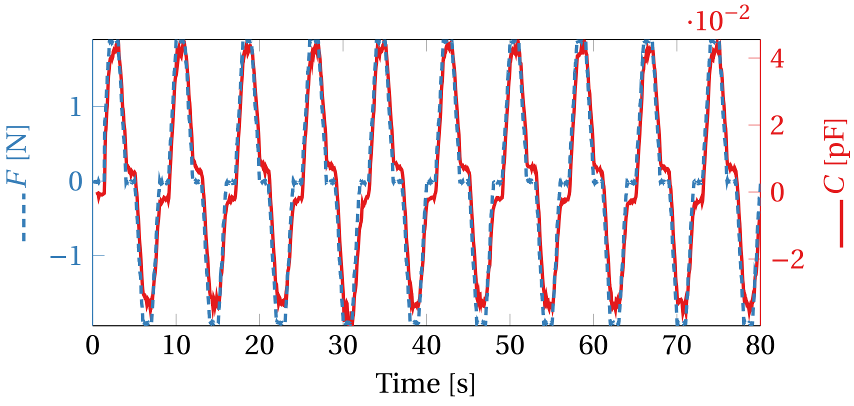

(a) Force-Capacitance

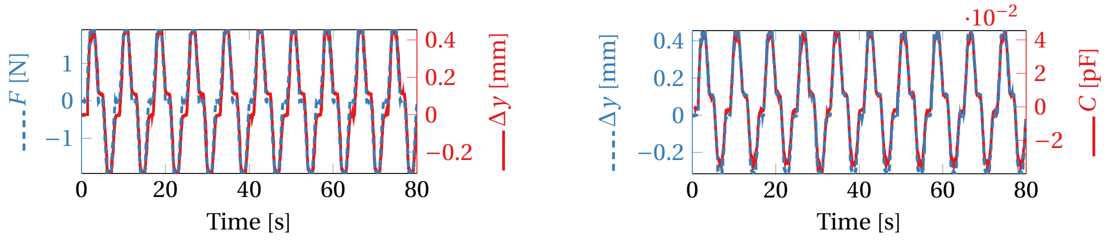

(b) Force-Displacement

(c) Displacement-capacitance

Figure H.7: Trapezium wave input (sensor 2)

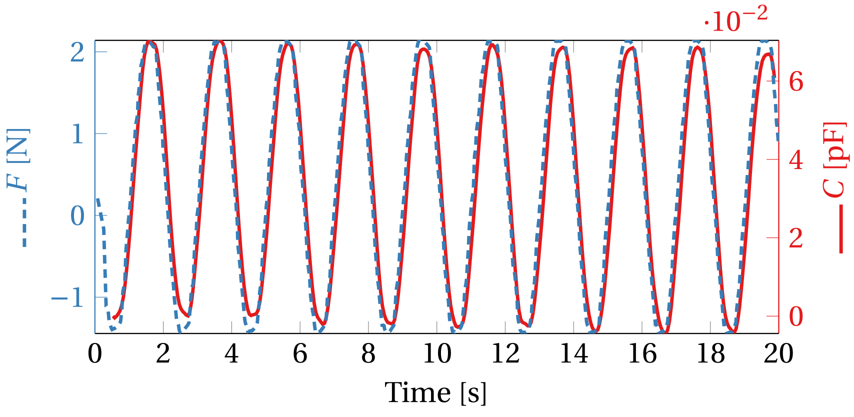

(a) Force-Capacitance

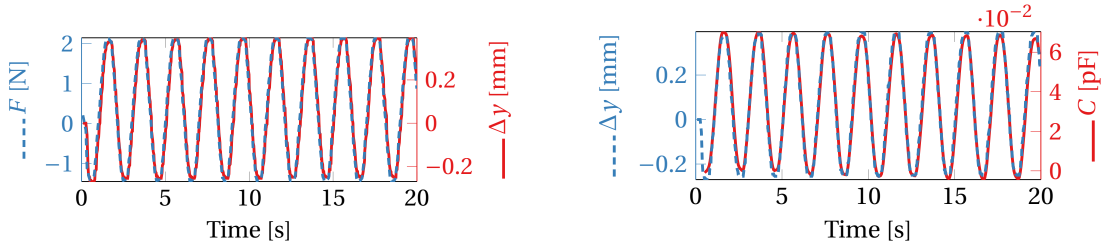

(b) Force-Displacement

(c) Displacement-capacitance

Figure H.8: sine wave input (sensor 2)

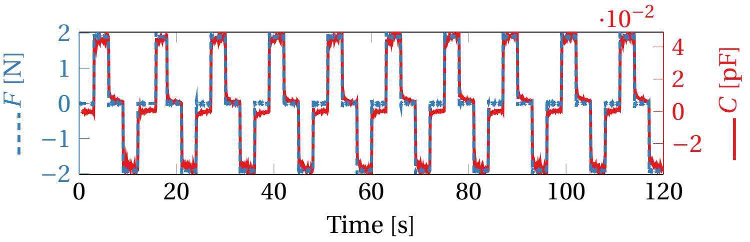

(a) Force-Capacitance

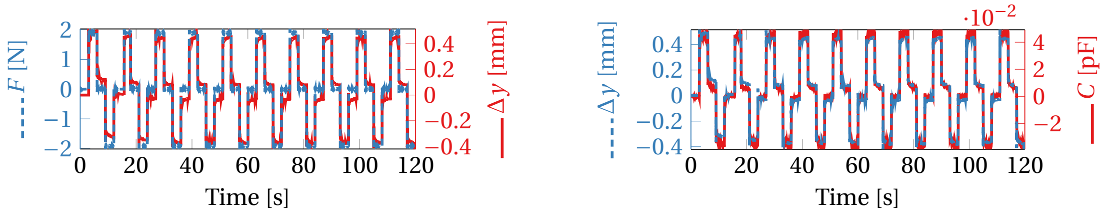

(b) Force-Displacement

(c) Displacement-capacitance

Figure H.9: Square-like wave input (sensor 2)

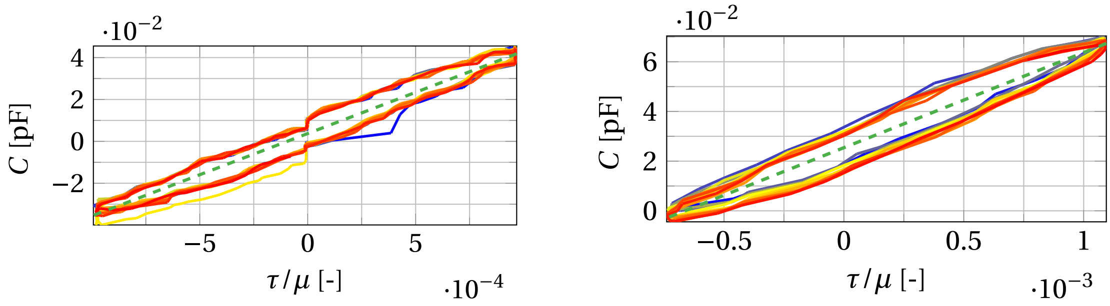

(a) Trapezium

(b) Sine

Figure H.10: Force to capacitance

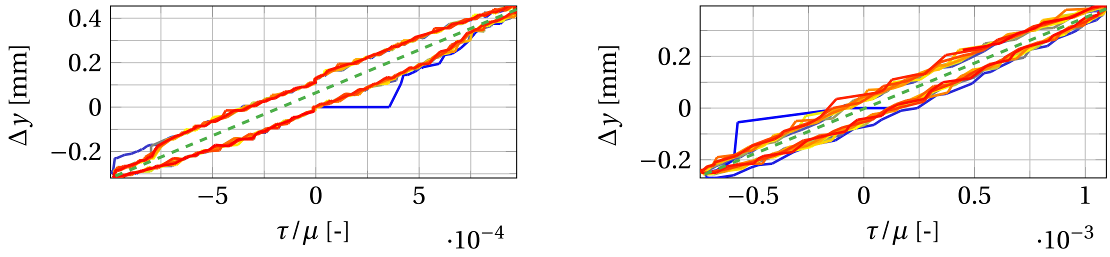

(a) Trapezium

(b) Sine

Figure H.11: Normalized shear stress to displacement

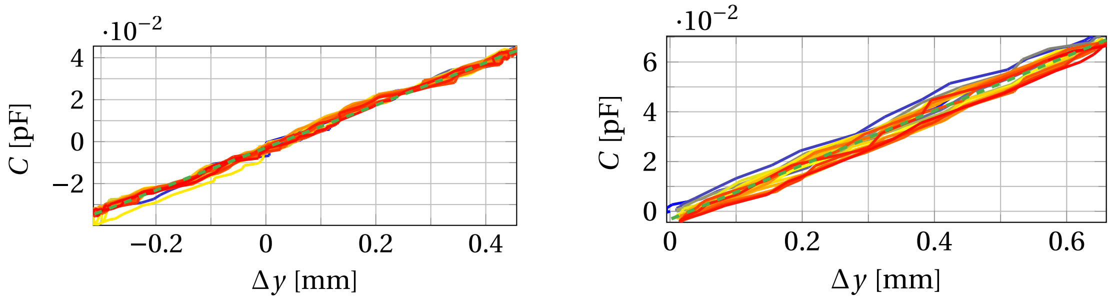

(a) Trapezium

(b) Sine

Figure H.12: Displacement to capacitance

H.1.3 Sensor 3-1a

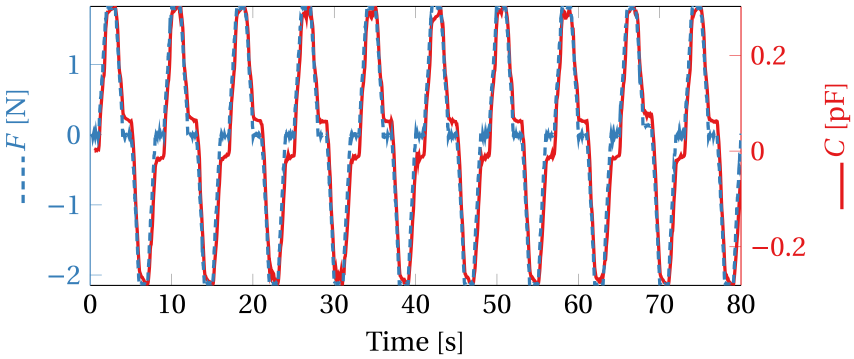

(a) Force-Capacitance

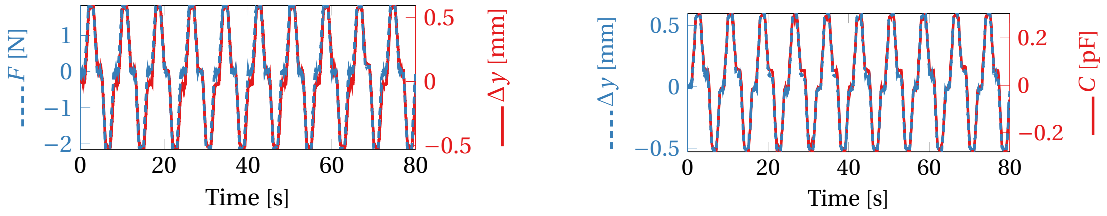

(b) Force-Displacement

(c) Displacement-capacitance

Figure H.13: Trapezium wave input (sensor 3-1a)

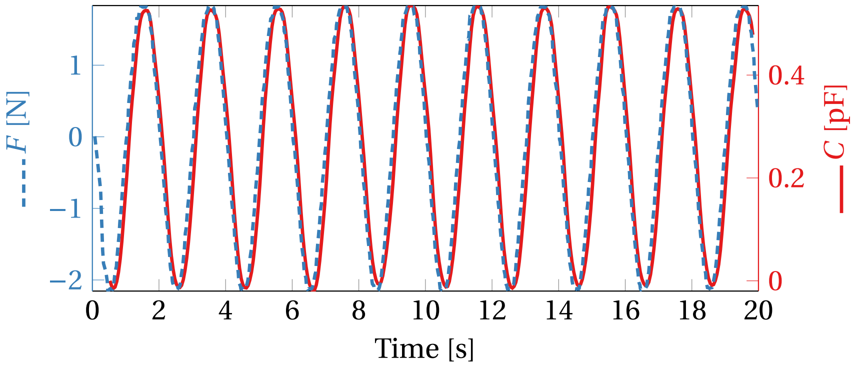

(a) Force-Capacitance

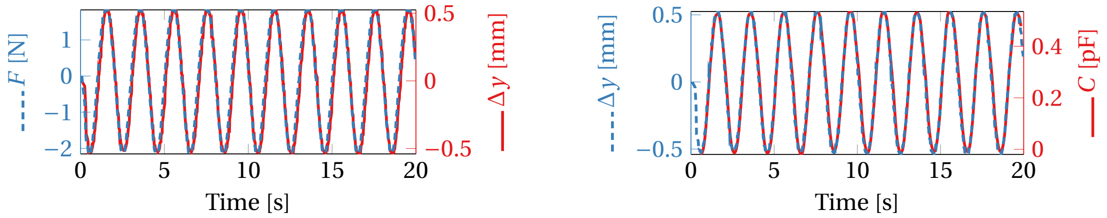

(b) Force-Displacement

(c) Displacement-capacitance

Figure H.14: sine wave input (sensor 3-1a)

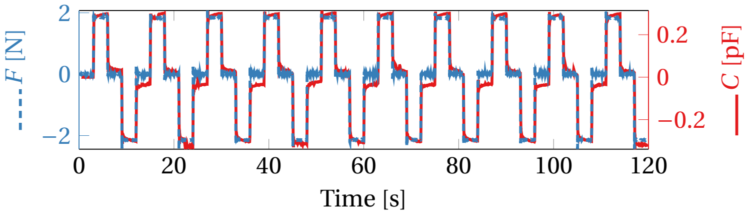

(a) Force-Capacitance

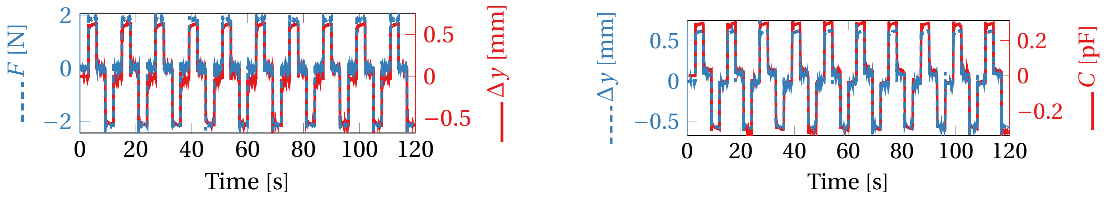

(b) Force-Displacement

(c) Displacement-capacitance

Figure H.15: Square-like wave input (sensor 3-1a)

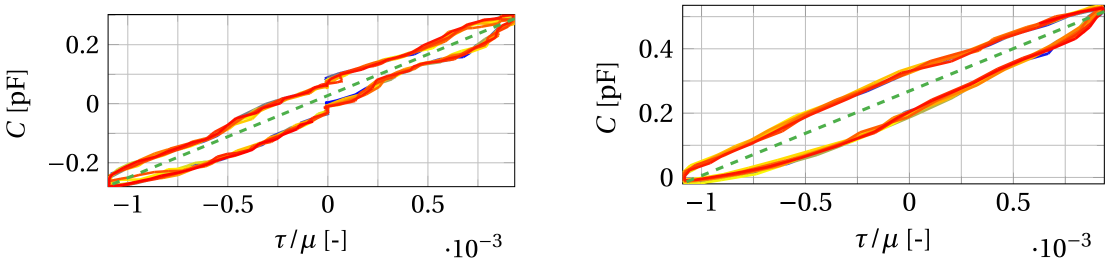

(a) Trapezium

(b) Sine

Figure H.16: Force to capacitance

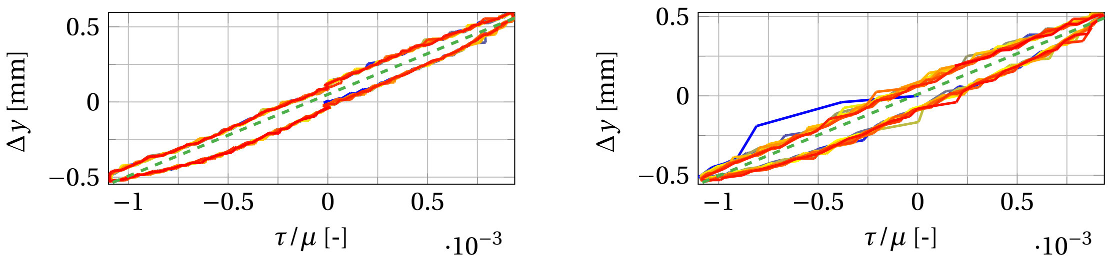

(a) Trapezium

(b) Sine

Figure H.17: Normalized shear stress to displacement

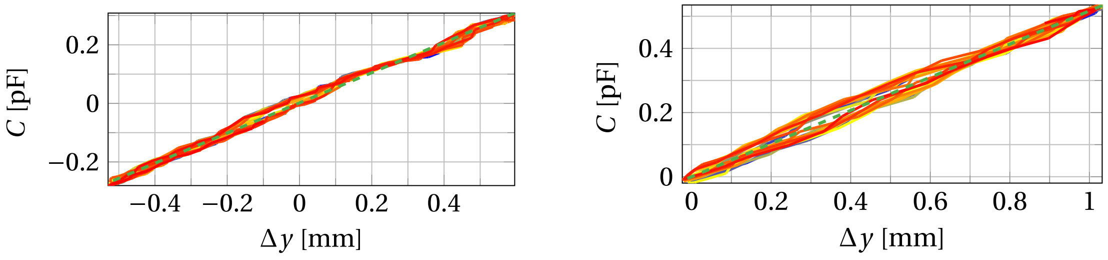

(a) Trapezium

(b) Sine

Figure H.18: Displacement to capacitance

H.1.4 Sensor 3-1b

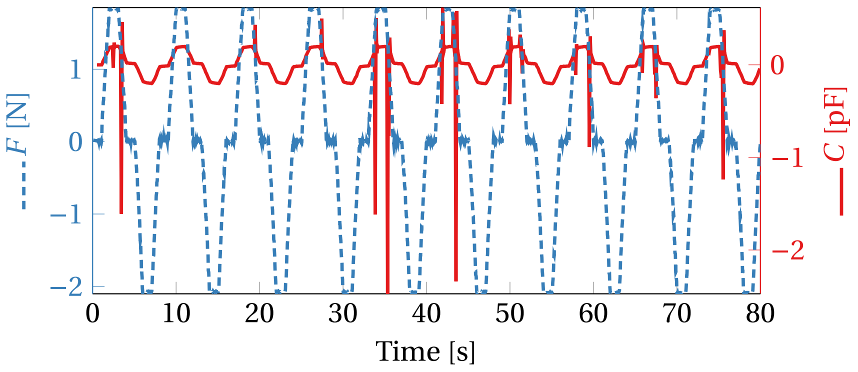

(a) Force-Capacitance

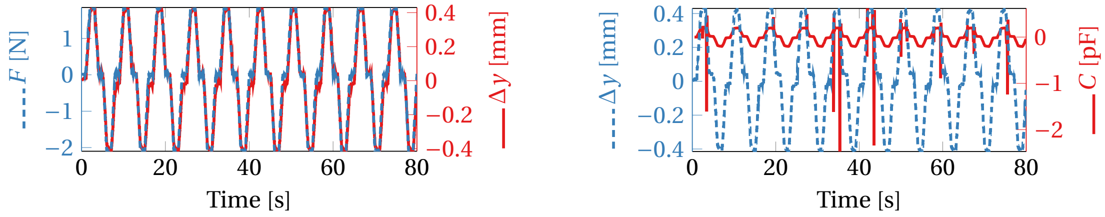

(b) Force-Displacement

(c) Displacement-capacitance

Figure H.19: Trapezium wave input (sensor 3-1b)

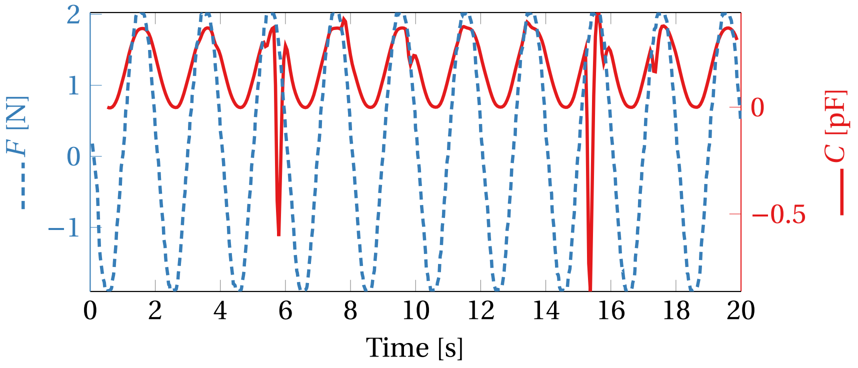

(a) Force-Capacitance

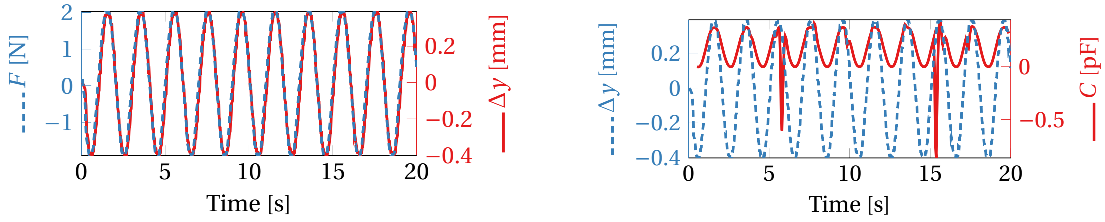

(b) Force-Displacement

(c) Displacement-capacitance

Figure H.20: sine wave input (sensor 3-1b)

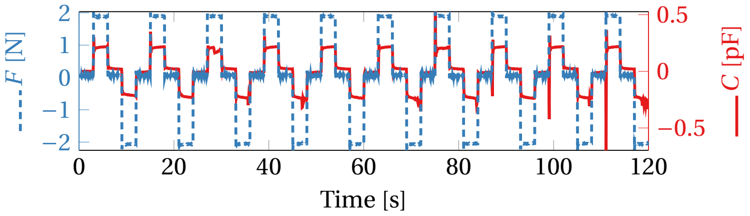

(a) Force-Capacitance

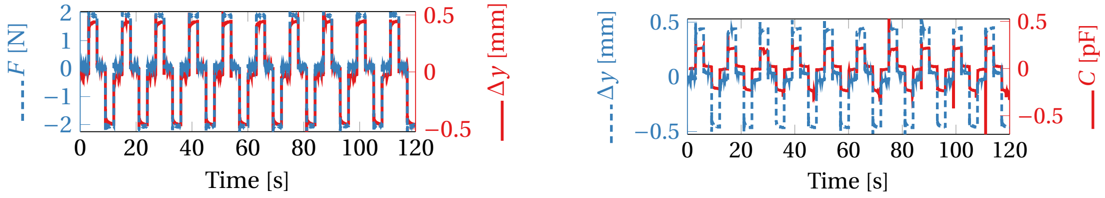

(b) Force-Displacement

(c) Displacement-capacitance

Figure H.21: Square-like wave input (sensor 3-1b)

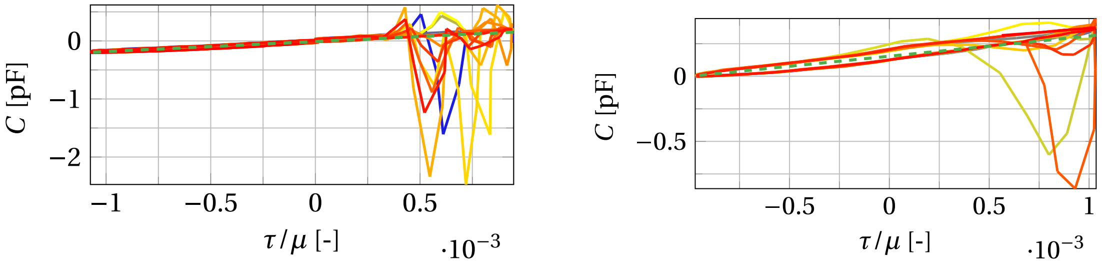

(a) Trapezium

(b) Sine

Figure H.22: Force to capacitance

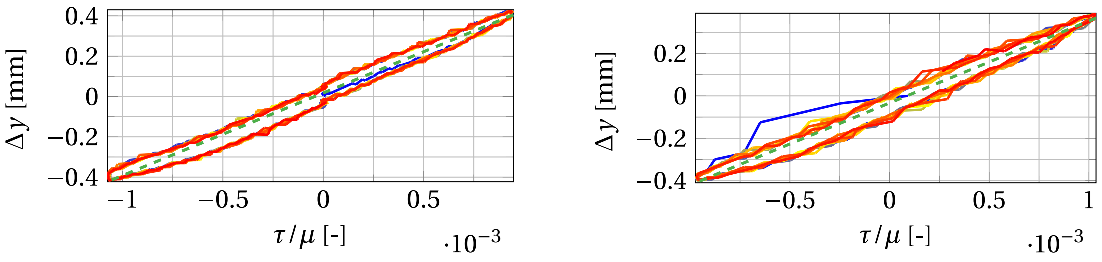

(a) Trapezium

(b) Sine

Figure H.23: Normalized shear stress to displacement

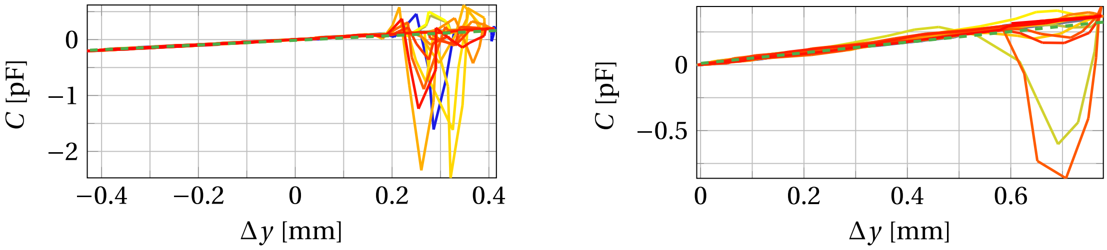

(a) Trapezium

(b) Sine

Figure H.24: Displacement to capacitance

H.1.5 Sensor 3-1c

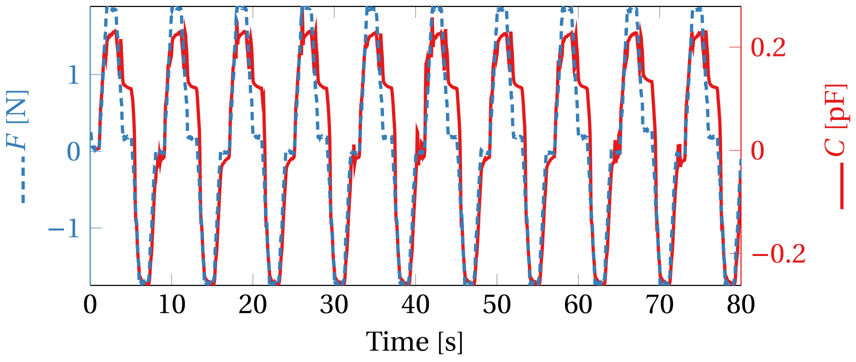

(a) Force-Capacitance

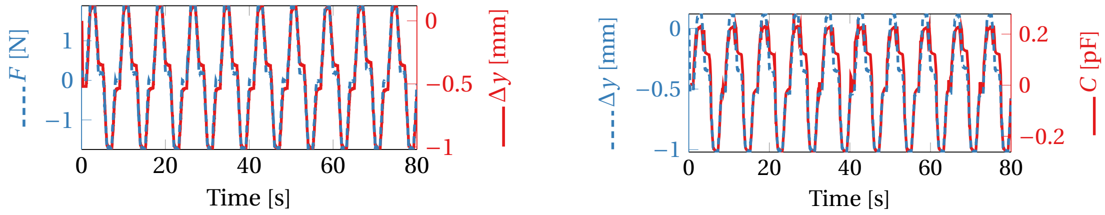

(b) Force-Displacement

(c) Displacement-capacitance

Figure H.25: Trapezium wave input (sensor 3-1c)

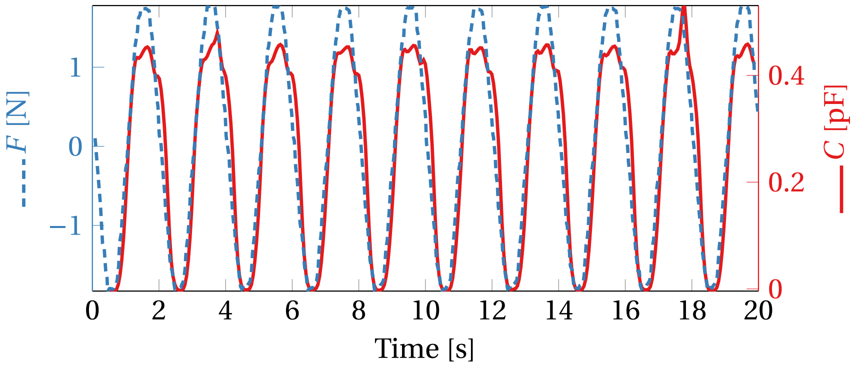

(a) Force-Capacitance

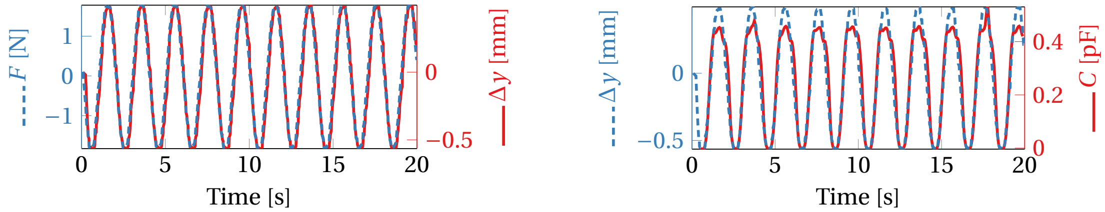

(b) Force-Displacement

(c) Displacement-capacitance

Figure H.26: sine wave input (sensor 3-1c)

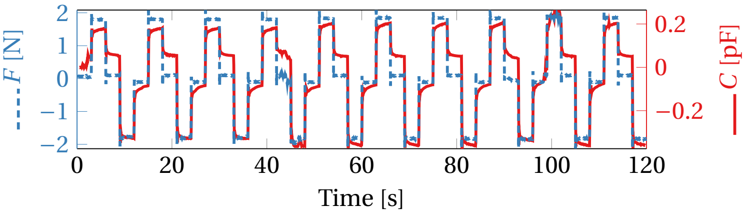

(a) Force-Capacitance

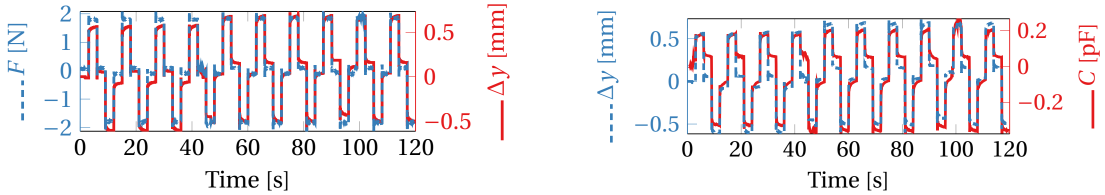

(b) Force-Displacement

(c) Displacement-capacitance

Figure H.27: Square-like wave input (sensor 3-1c)

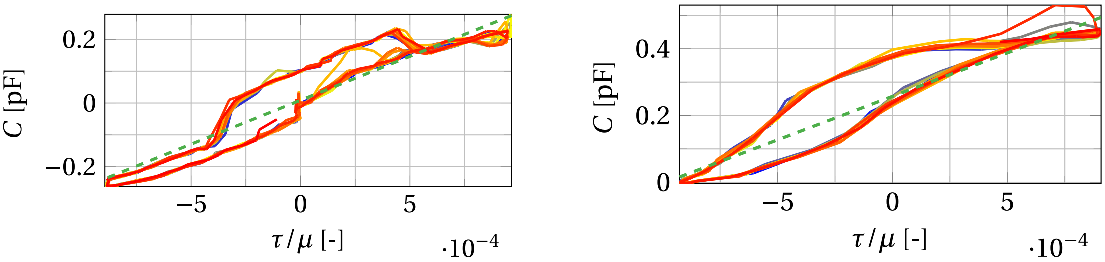

(a) Trapezium

(b) Sine

Figure H.28: Force to capacitance

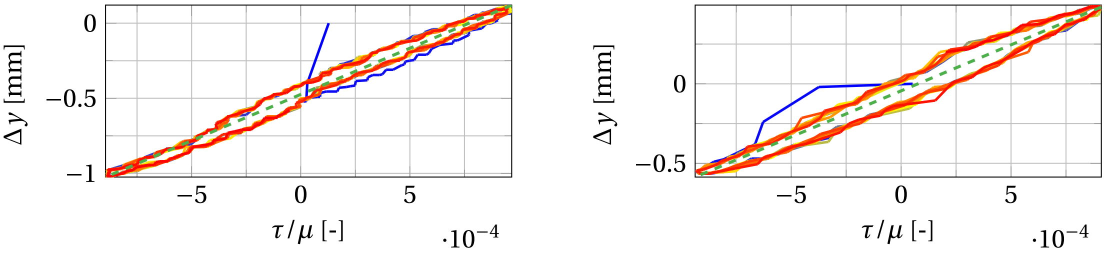

(a) Trapezium

(b) Sine

Figure H.29: Normalized shear stress to displacement

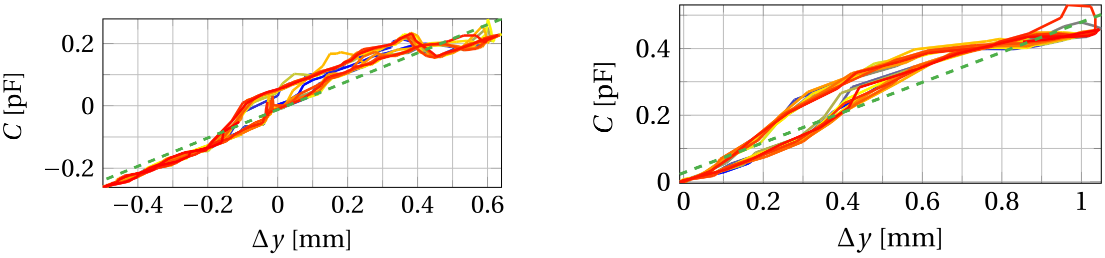

(a) Trapezium

(b) Sine

Figure H.30: Displacement to capacitance

H.1.6 Sensor 5a

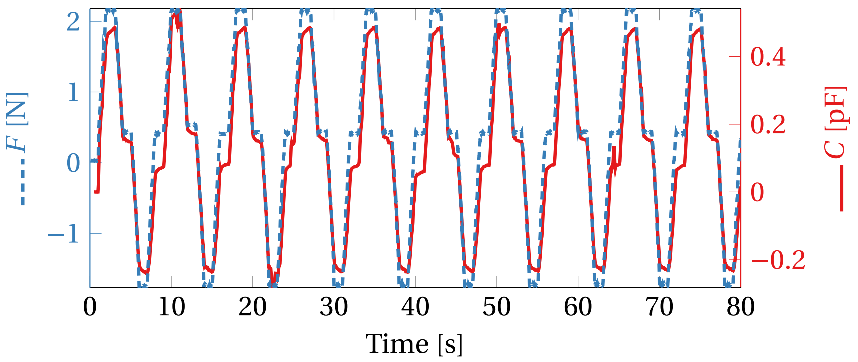

(a) Force-Capacitance

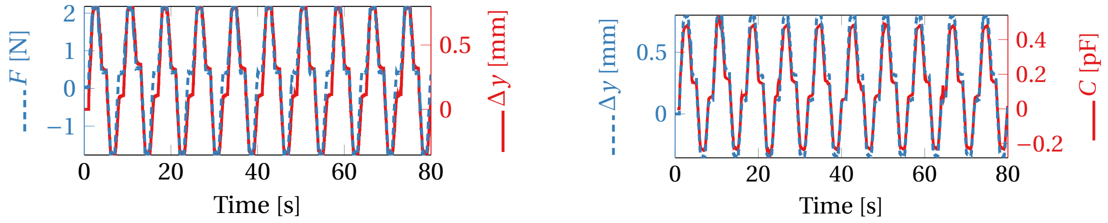

(b) Force-Displacement

(c) Displacement-capacitance

Figure H.31: Trapezium wave input (sensor 5a)

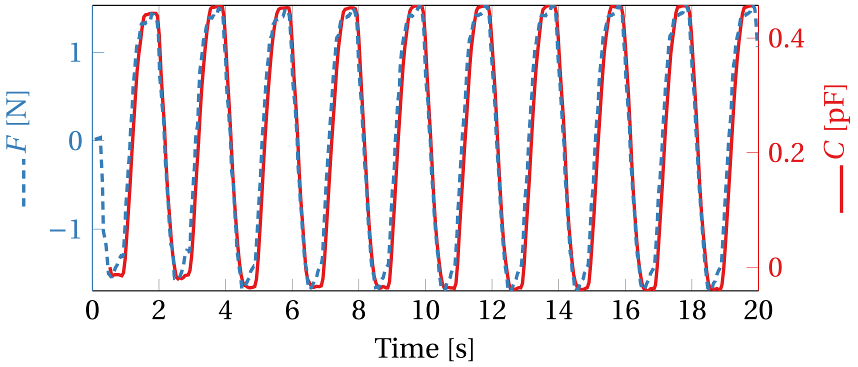

(a) Force-Capacitance

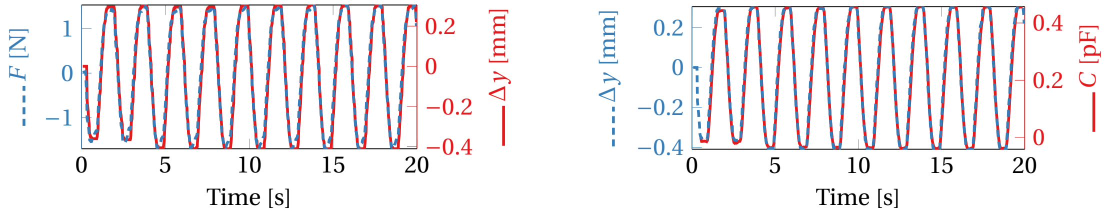

(b) Force-Displacement

(c) Displacement-capacitance

Figure H.32: sine wave input (sensor 5a)

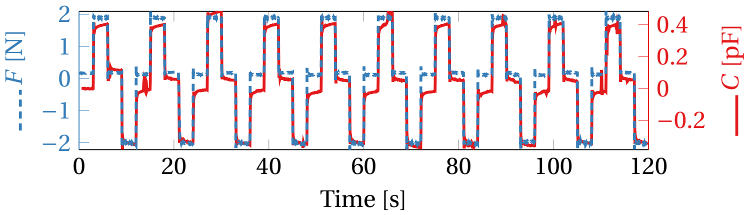

(a) Force-Capacitance

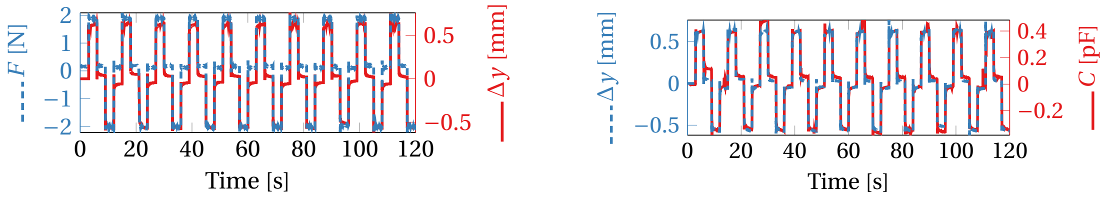

(b) Force-Displacement

(c) Displacement-capacitance

Figure H.33: Square-like wave input (sensor 5a)

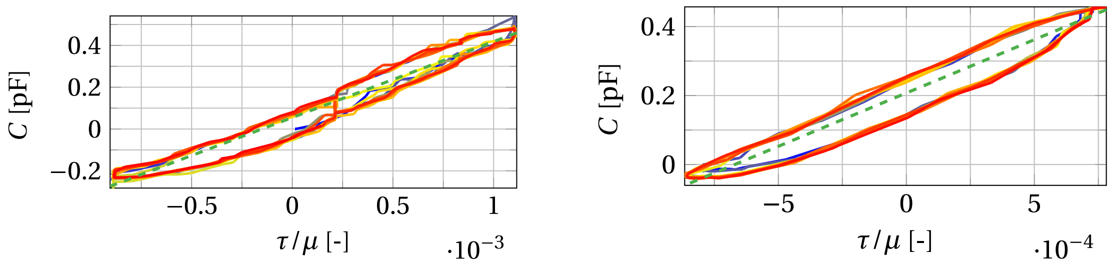

(a) Trapezium

(b) Sine

Figure H.34: Force to capacitance

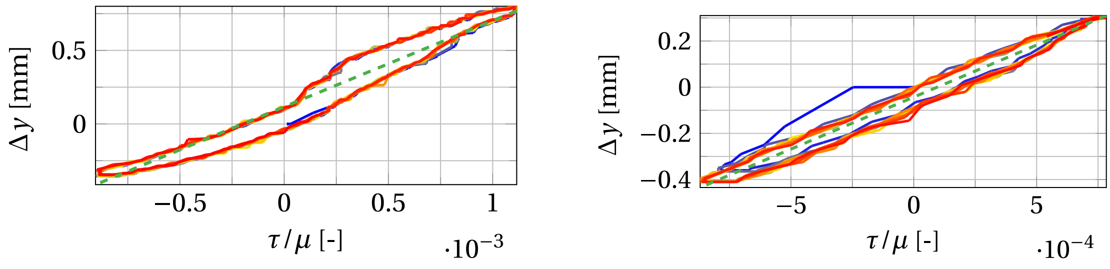

(a) Trapezium

(b) Sine

Figure H.35: Normalized shear stress to displacement

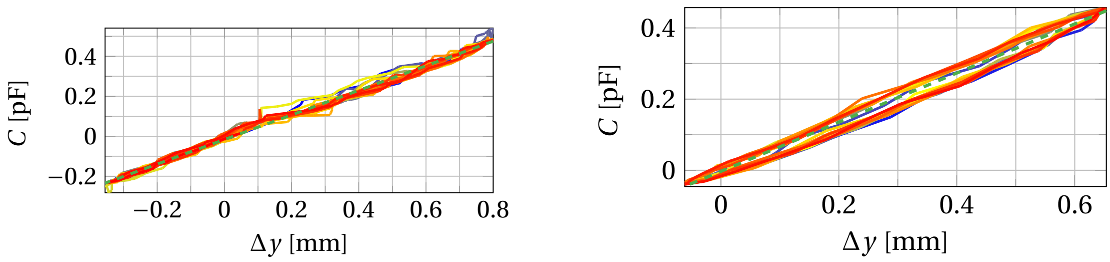

(a) Trapezium

(b) Sine

Figure H.36: Displacement to capacitance

H.1.7 Sensor 5b

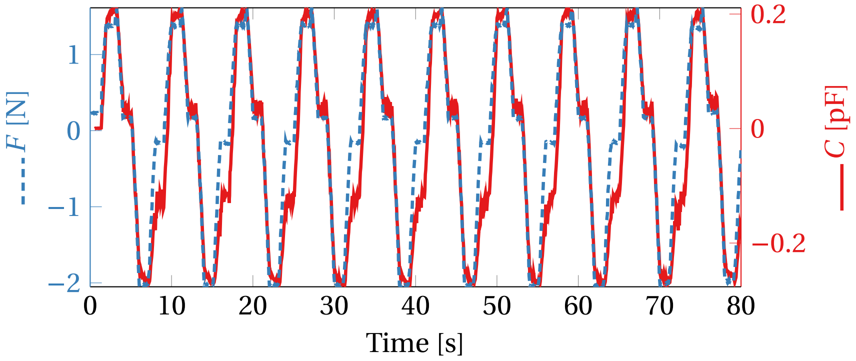

(a) Force-Capacitance

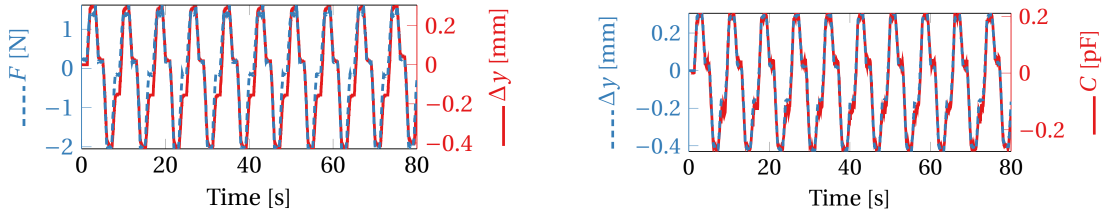

(b) Force-Displacement

(c) Displacement-capacitance

Figure H.37: Trapezium wave input (sensor 5b)

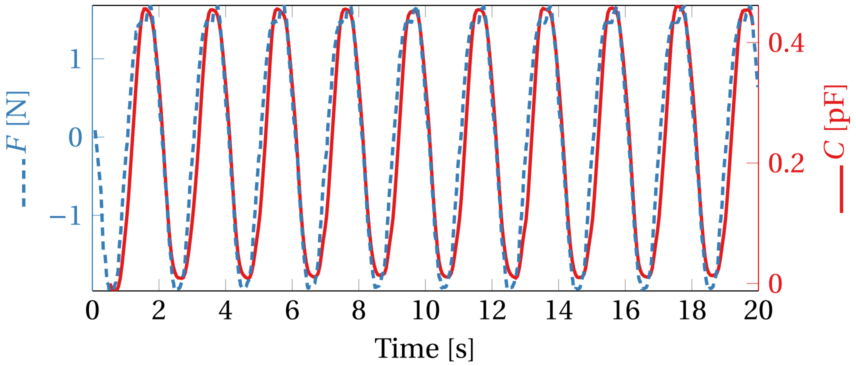

(a) Force-Capacitance

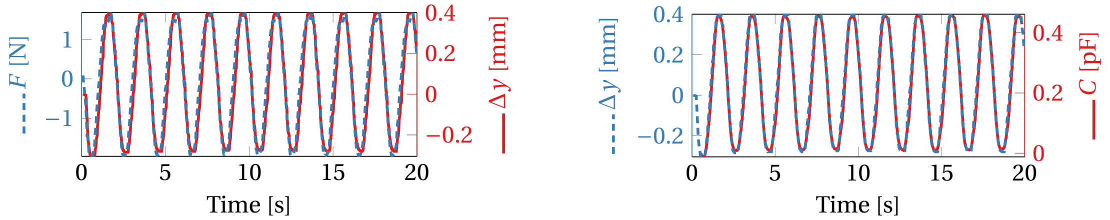

(b) Force-Displacement

(c) Displacement-capacitance

Figure H.38: sine wave input (sensor 5b)

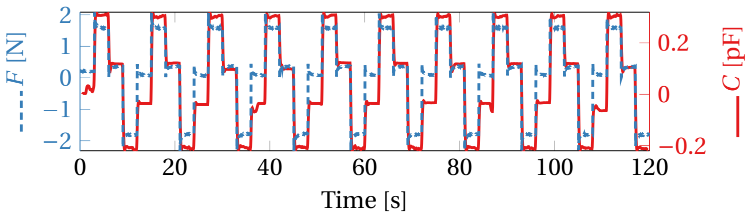

(a) Force-Capacitance

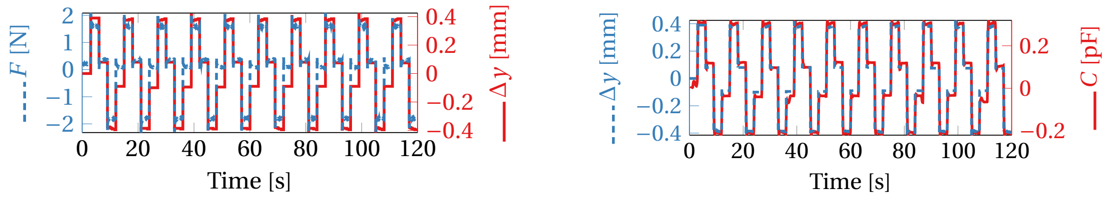

(b) Force-Displacement

(c) Displacement-capacitance

Figure H.39: Square-like wave input (sensor 5b)

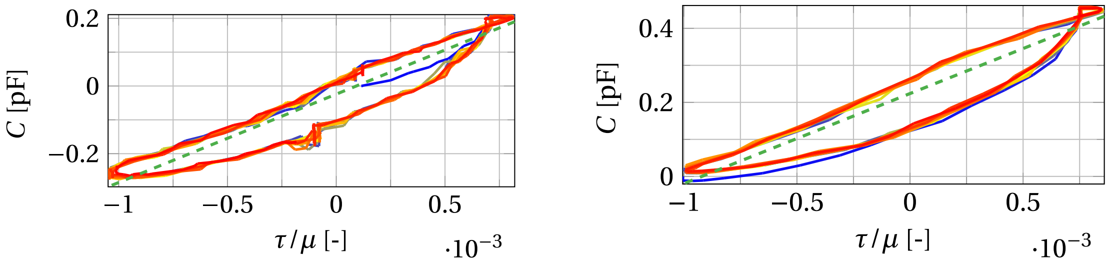

(a) Trapezium

(b) Sine

Figure H.40: Force to capacitance

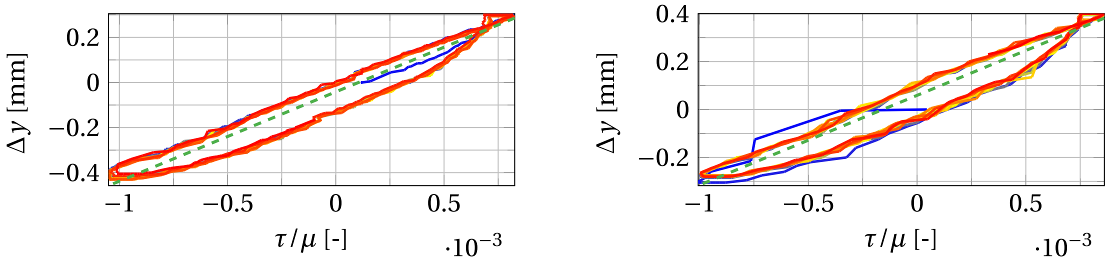

(a) Trapezium

(b) Sine

Figure H.41: Normalized shear stress to displacement

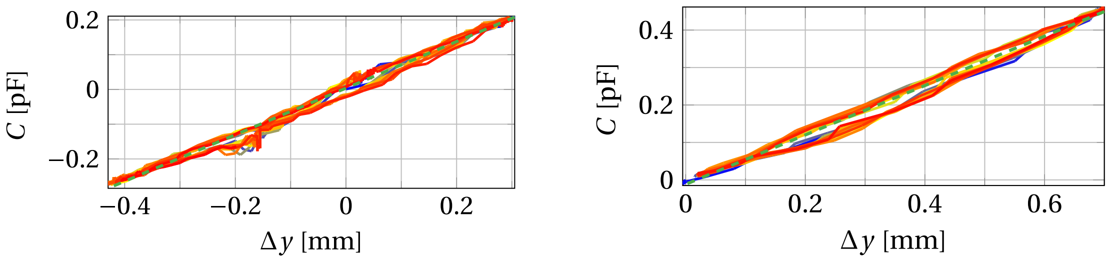

(a) Trapezium

(b) Sine

Figure H.42: Displacement to capacitance

H.2 Large Armadillo sensors

H.2.1 Sensor Armadillo1

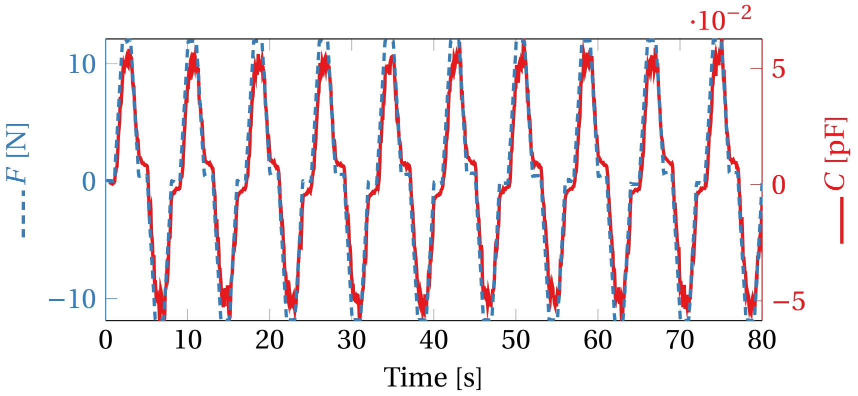

(a) Force-Capacitance

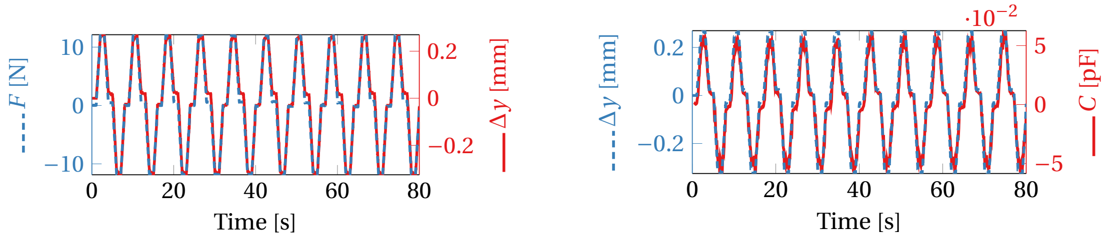

(b) Force-Displacement

(c) Displacement-capacitance

Figure H.43: Trapezium wave input (sensor Armadillo1)

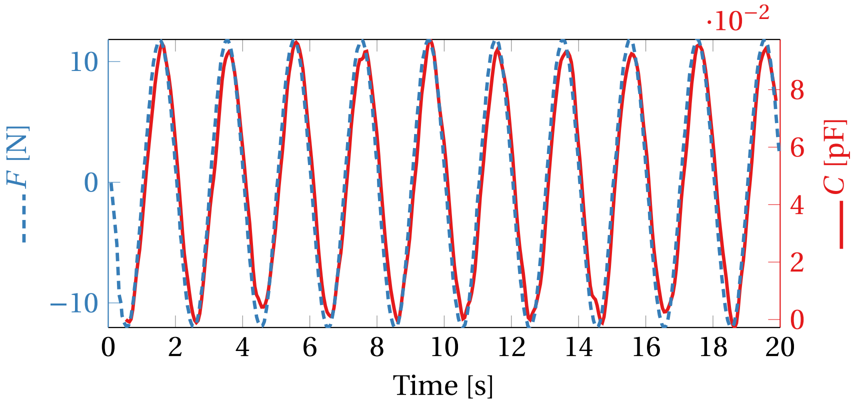

(a) Force-Capacitance

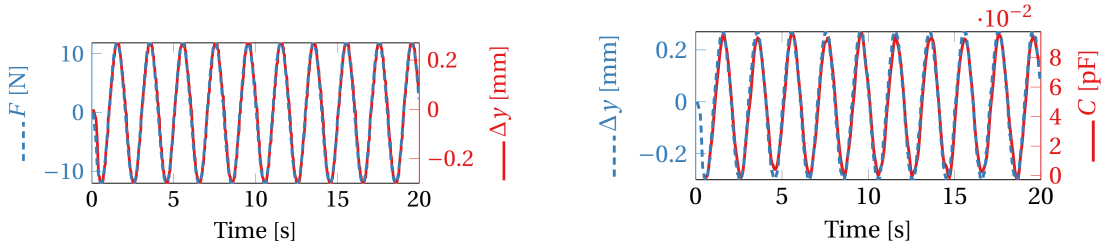

(b) Force-Displacement

(c) Displacement-capacitance

Figure H.44: sine wave input (sensor Armadillo1)

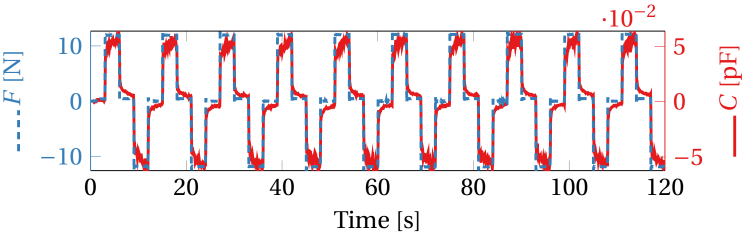

(a) Force-Capacitance

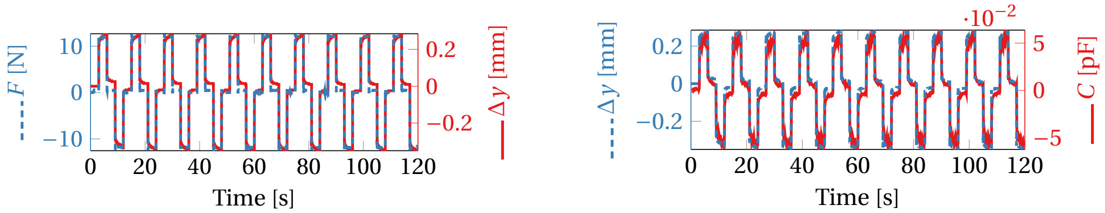

(b) Force-Displacement **(c)** Displacement-capacitance

Figure H.45: Square-like wave input (sensor Armadillo1)

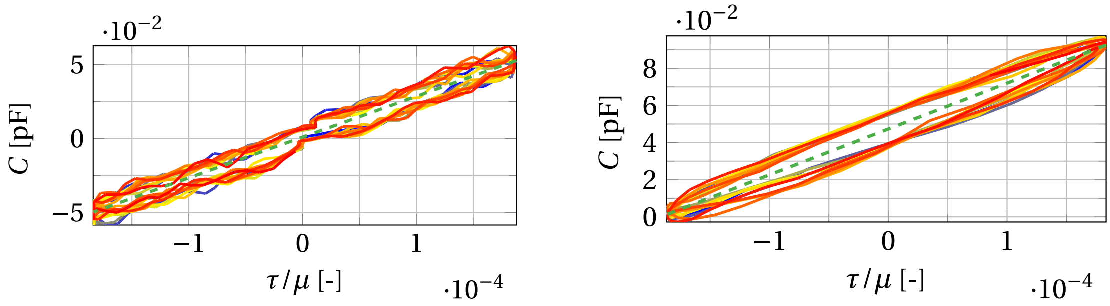

(a) Trapezium **(b)** Sine

Figure H.46: Force to capacitance

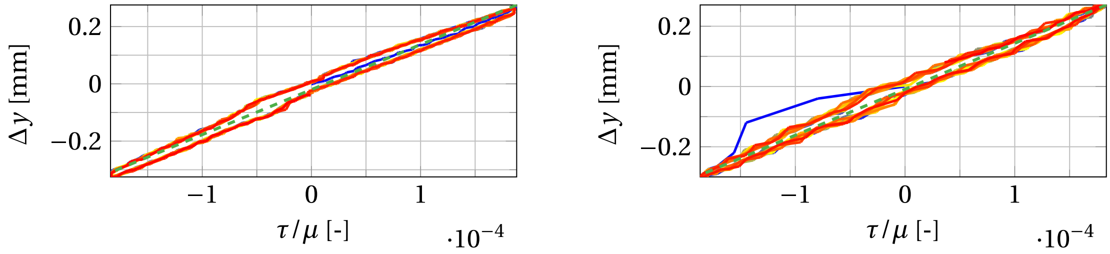

(a) Trapezium **(b)** Sine

Figure H.47: Normalized shear stress to displacement

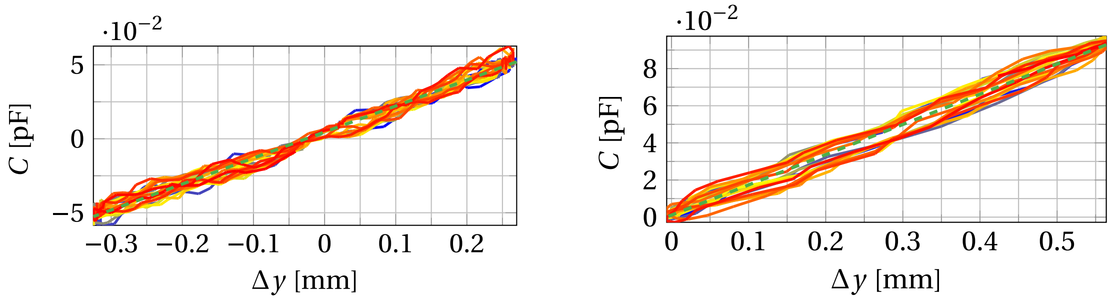

(a) Trapezium **(b)** Sine

Figure H.48: Displacement to capacitance

H.2.2 Sensor Armadillo2

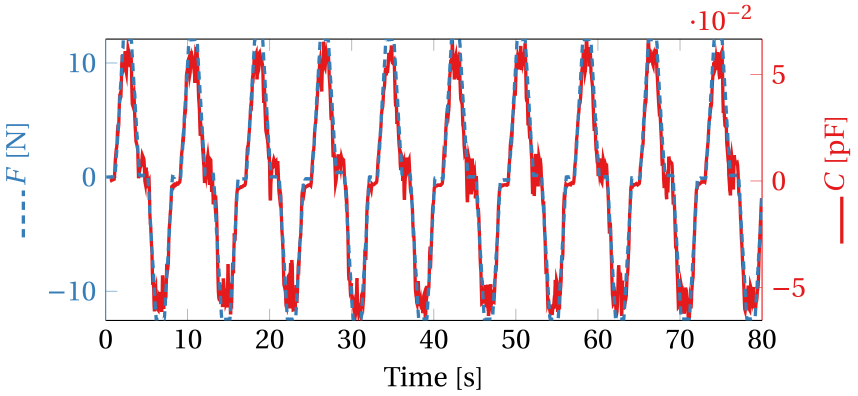

(a) Force-Capacitance

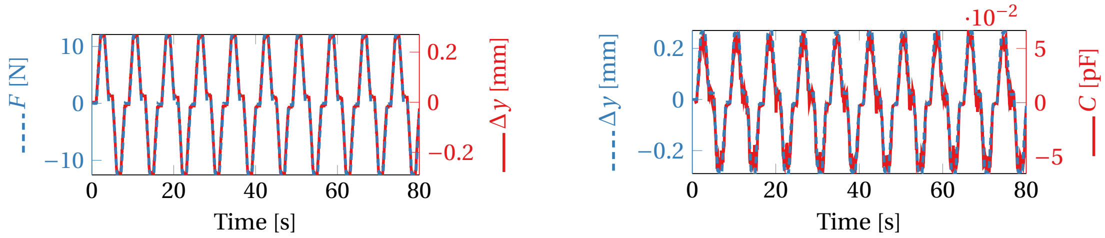

(b) Force-Displacement

(c) Displacement-capacitance

Figure H.49: Trapezium wave input (sensor Armadillo2)

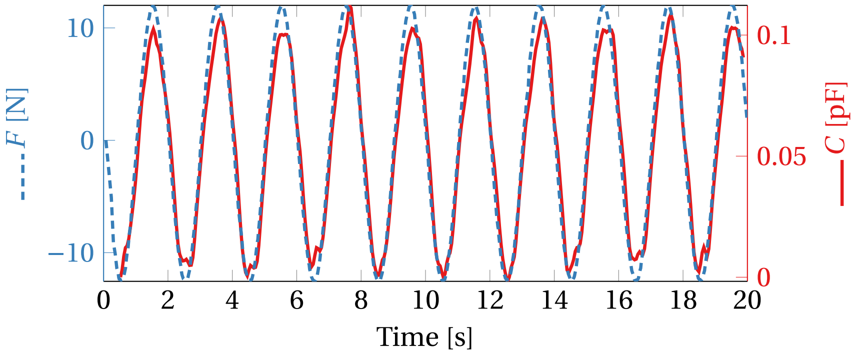

(a) Force-Capacitance

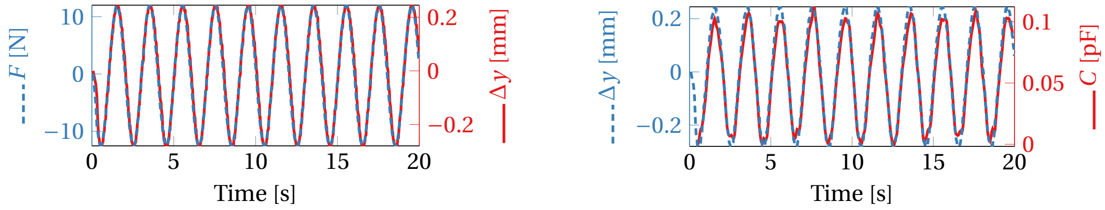

(b) Force-Displacement

(c) Displacement-capacitance

Figure H.50: sine wave input (sensor Armadillo2)

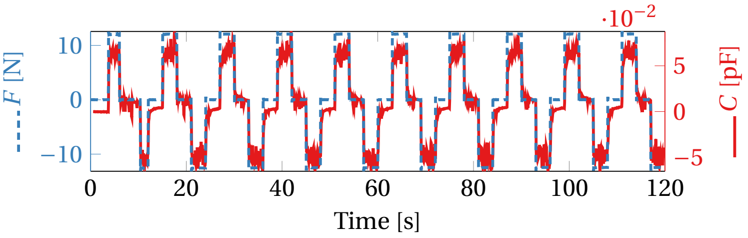

(a) Force-Capacitance

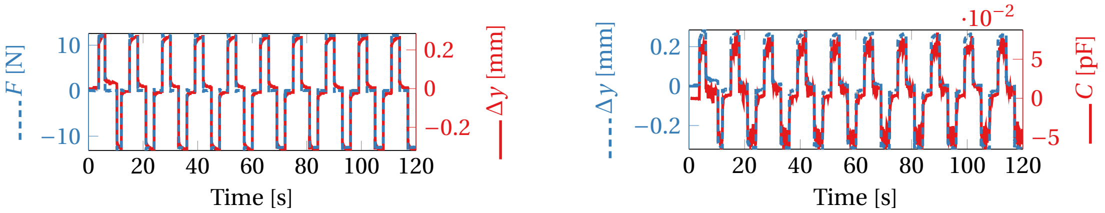

(b) Force-Displacement **(c)** Displacement-capacitance

Figure H.51: Square-like wave input (sensor Armadillo2)

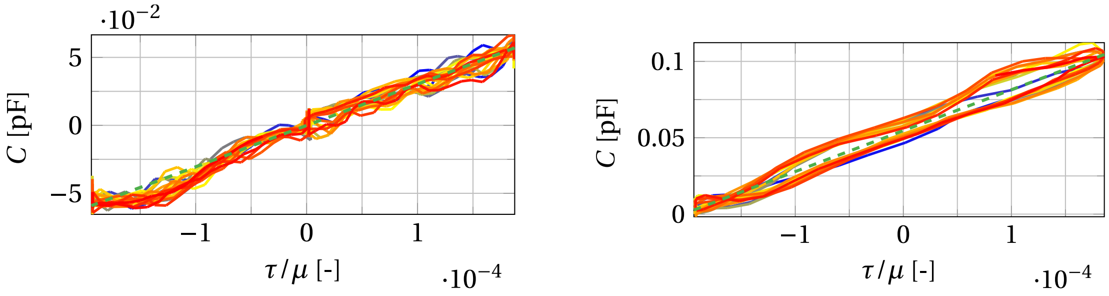

(a) Trapezium **(b)** Sine

Figure H.52: Force to capacitance

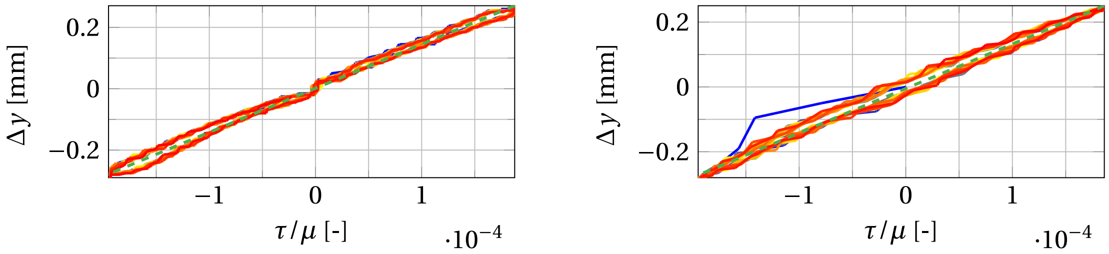

(a) Trapezium **(b)** Sine

Figure H.53: Normalized shear stress to displacement

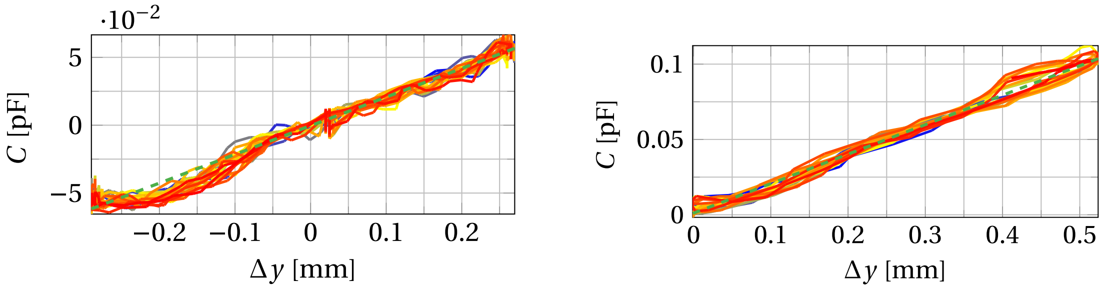

(a) Trapezium **(b)** Sine

Figure H.54: Displacement to capacitance

Bibliography

[1] C.-W. Lung, F.-L. Wu, F. Liao, F. Pu, Y. Fan, and Y.-K. Jan, “Emerging technologies for the prevention and management of diabetic foot ulcers,” *Journal of Tissue Viability*, vol. 29, no. 2, pp. 61 – 68, 2020. doi:10.1016/j.jtv.2020.03.003.

[2] L. Wang, D. Jones, G. J. Chapman, H. J. Siddle, D. A. Russell, A. Alazmani, and P. Culmer, “A review of wearable sensor systems to monitor plantar loading in the assessment of diabetic foot ulcers,” *IEEE Transactions on Biomedical Engineering*, vol. 67, no. 7, pp. 1989–2004, 2020. doi:10.1109/TBME.2019.2953630.

[3] B. E. Sumpio, “Foot ulcers,” *New England Journal of Medicine*, vol. 343, no. 11, pp. 787–793, 2000. doi:10.1056/NEJM200009143431107.

[4] J. J. van Netten, P. E. Price, L. A. Lavery, M. Monteiro-Soares, A. Rasmussen, Y. Jubiz, S. A. Bus, and on behalf of the International Working Group on the Diabetic Foot (IWGDF), “Prevention of foot ulcers in the at-risk patient with diabetes: a systematic review,” *Diabetes/Metabolism Research and Reviews*, vol. 32, no. S1, pp. 84–98, 2016. doi:10.1002/dmrr.2701.

[5] M. Yavuz, H. Master, A. Garrett, L. A. Lavery, and L. S. Adams, “Peak plantar shear and pressure and foot ulcer locations: A call to revisit ulceration pathomechanics,” *Diabetes Care*, vol. 38, no. 11, pp. e184–e185, 2015. doi:10.2337/dc15-1596.

[6] M. Schouten, G. Wolterink, A. Dijkshoorn, D. Kosmas, S. Stramigioli, and G. Krijnen, “A review of extrusion-based 3d printing for the fabrication of electro-and biomechanical sensors,” *IEEE Sensors Journal*, vol. PP, 12 2020. doi:10.1109/JSEN.2020.3042436.

[7] A. Umrani, “3d printed colorimetric flow sensor,” Master’s thesis, University of Twente, Enschede, July 2020. Available online: `http://purl.utwente.nl/essays/83163` [Accessed: 10-2-2021].

[8] G. Wolterink, R. Sanders, and G. Krijnen, “A flexible, three material, 3d-printed, shear force sensor for use on finger tips,” in *IEEE Sensors*, (United States), IEEE, Oct. 2019. doi:10.1109/SENSORS43011.2019.8956757.

[9] A. Dijkshoorn, P. Werkman, M. Welleweerd, G. Wolterink, B. Eijking, J. Delamare, R. Sanders, and G. J. M. Krijnen, “Embedded sensing: integrating sensors in 3-d printed structures,” *Journal of Sensors and Sensor Systems*, vol. 7, no. 1, pp. 169–181, 2018. doi:10.5194/jsss-7-169-2018.

[10] Y. Xu, X. Wu, X. Guo, B. Kong, M. Zhang, X. Qian, S. Mi, and W. Sun, “The boom in 3d-printed sensor technology,” *Sensors*, vol. 17, p. 1166, May 2017. doi:10.3390/s17051166.

[11] G. J. Krijnen and R. G. Sanders, “Recent developments in bio-inspired sensors fabricated by additive manufacturing technologies,” in *7th Forum on New Materials - Part D*, vol. 100 of *Advances in Science and Technology*, pp. 197–206, Trans Tech Publications Ltd, 1 2017. doi:10.4028/www.scientific.net/AST.100.197.

[12] D. J. Janisse and E. J. Janisse, “Shoes, orthoses, and prostheses for partial foot amputation and diabetic foot infection,” *Foot and ankle clinics*, vol. 15, no. 3, pp. 509–523, 2010. doi:10.1016/j.fcl.2010.04.004.

[13] S. Telfer, J. Woodburn, A. Collier, and P. Cavanagh, "Virtually optimized insoles for offloading the diabetic foot: A randomized crossover study," *Journal of Biomechanics*, vol. 60, pp. 157 – 161, 2017. doi:10.1016/j.jbiomech.2017.06.028.

[14] Z. Ma, J. Lin, X. Xu, Z. Ma, L. Tang, C. Sun, D. Li, C. Liu, Y. Zhong, and L. Wang, "Design and 3d printing of adjustable modulus porous structures for customized diabetic foot insoles," *International Journal of Lightweight Materials and Manufacture*, vol. 2, no. 1, pp. 57 – 63, 2019. doi:10.1016/j.ijlmm.2018.10.003.

[15] C. Tavares, M. Domingues, A. Frizera-Neto, T. Leite, C. Leitão, N. Alberto, C. Marques, A. Radwan, E. Rocon, and P. André, "Gait shear and plantar pressure monitoring: A non-invasive ofs based solution for e-health architectures," *Sensors*, vol. 18, p. 1334, Apr 2018. doi:10.3390/s18051334.

[16] A. Amemiya, H. Noguchi, M. Oe, H. Sanada, and T. Mori, "Establishment of a measurement method for in-shoe pressure and shear stress in specific regions for diabetic ulcer prevention," in *2016 38th Annual International Conference of the IEEE Engineering in Medicine and Biology Society (EMBC)*, pp. 2291–2294, IEEE, 2016. doi:10.1109/EMBC.2016.7591187.

[17] T. D. Ngo, A. Kashani, G. Imbalzano, K. T. Nguyen, and D. Hui, "Additive manufacturing (3d printing): A review of materials, methods, applications and challenges," *Composites Part B: Engineering*, vol. 143, pp. 172 – 196, 2018. doi:10.1016/j.compositesb.2018.02.012.

[18] S. W. Kwok, K. H. H. Goh, Z. D. Tan, S. T. M. Tan, W. W. Tjiu, J. Y. Soh, Z. J. G. Ng, Y. Z. Chan, H. K. Hui, and K. E. J. Goh, "Electrically conductive filament for 3d-printed circuits and sensors," *Applied Materials Today*, vol. 9, pp. 167 – 175, 2017. doi:10.1016/j.apmt.2017.07.001.

[19] V. G. Rocha, E. Saiz, I. S. Tirichenko, and E. García-Tuñón, "Direct ink writing advances in multi-material structures for a sustainable future," *J. Mater. Chem. A*, vol. 8, pp. 15646–15657, 2020. doi:10.1039/D0TA04181E.

[20] E. Davoodi, H. Fayazfar, F. Liravi, E. Jabari, and E. Toyserkani, "Drop-on-demand high-speed 3d printing of flexible milled carbon fiber/silicone composite sensors for wearable biomonitoring devices," *Additive Manufacturing*, vol. 32, p. 101016, 2020. doi:10.1016/j.addma.2019.101016.

[21] M. Schouten, R. Sanders, and G. Krijnen, "3d printed flexible capacitive force sensor with a simple micro-controller based readout," in *2017 IEEE SENSORS*, pp. 1–3, 10 2017. doi:10.1109/ICSENS.2017.8233949.

[22] C. Shemelya, L. Banuelos-Chacon, A. Melendez, C. Kief, D. Espalin, R. Wicker, G. Krijnen, and E. MacDonald, "Multi-functional 3d printed and embedded sensors for satellite qualification structures," in *Proceedings IEEE Sensors 2015*, (United States), pp. 1422–1425, IEEE, Nov. 2015. doi:10.1109/ICSENS.2015.7370541.

[23] J. Mertodikromo, F. Zorin, and C. J. Lee, "A low-profile shear force sensor for wearable applications," *IEEE Sensors Journal*, vol. 20, no. 18, pp. 10453–10459, 2020. doi:10.1109/JSEN.2020.2985396.

[24] H.-K. Lee, J. Chung, S.-I. Chang, and E. Yoon, "Real-time measurement of the three-axis contact force distribution using a flexible capacitive polymer tactile sensor," *Journal of Micromechanics and Microengineering*, vol. 21, no. 3, p. 035010, 2011.

[25] M.-Y. Cheng, C.-L. Lin, Y.-T. Lai, and Y.-J. Yang, "A polymer-based capacitive sensing array for normal and shear force measurement," *Sensors*, vol. 10, no. 11, pp. 10211–10225, 2010. doi:10.3390/s101110211.

[26] N. Cross, *Engineering design methods : strategies for product design.* Hoboken, N.J. Chichester: Wiley, 4th ed. ed., 2008.

[27] M. E. Fernando, R. G. Crowther, and S. Wearing, *The Importance of Foot Pressure in Diabetes*, pp. 759–787. Cham: Springer International Publishing, 2018. doi:10.1007/978-3-319-14418-4_39.

[28] M. Hamatani, T. Mori, M. Oe, H. Noguchi, K. Takehara, A. Amemiya, Y. Ohashi, K. Ueki, T. Kadowaki, and H. Sanada, “Factors associated with callus in patients with diabetes, focused on plantar shear stress during gait,” *Journal of Diabetes Science and Technology*, vol. 10, no. 6, pp. 1353–1359, 2016. doi:10.1177/1932296816648164.

[29] M. Yavuz, A. Tajaddini, G. Botek, and B. L. Davis, “Temporal characteristics of plantar shear distribution: Relevance to diabetic patients,” *Journal of Biomechanics*, vol. 41, no. 3, pp. 556 – 559, 2008. doi:10.1016/j.jbiomech.2007.10.008.

[30] V. Berki and B. L. Davis, “Spatial frequency content of plantar pressure and shear profiles for diabetic and non-diabetic subjects,” *Journal of Biomechanics*, vol. 49, no. 15, pp. 3746 – 3748, 2016. doi:10.1016/j.jbiomech.2016.09.023.

[31] S. Stucke, D. McFarland, L. Goss, S. Fonov, G. R. McMillan, A. Tucker, N. Berme, H. Cenk Guler, C. Bigelow, and B. L. Davis, “Spatial relationships between shearing stresses and pressure on the plantar skin surface during gait,” *Journal of Biomechanics*, vol. 45, no. 3, pp. 619 – 622, 2012. doi:10.1016/j.jbiomech.2011.11.004.

[32] N. Madanchi, O. Tabatabaei-Malazy, M. Pajouhi, R. Heshmat, B. Larijani, and M.-R. Mohajeri-Tehrani, “Who are diabetic foot patients? a descriptive study on 873 patients,” *Journal of diabetes and metabolic disorders*, vol. 12, pp. 36–36, 2013. doi:10.1186/2251-6581-12-36.

[33] L.-Y. Zhou, J. Fu, and Y. He, “A review of 3d printing technologies for soft polymer materials,” *Advanced Functional Materials*, vol. 30, no. 28, p. 2000187, 2020. doi:10.1002/adfm.202000187.

[34] H. Nassar, M. Ntagios, W. T. Navaraj, and R. Dahiva, “Multi-material 3d printed bendable smart sensing structures,” in *2018 IEEE Sensors*, pp. 1–4, 2018. doi:10.1109/ICSENS.2018.8589625.

[35] J. Yin, V. J. Santos, and J. D. Posner, “Bioinspired flexible microfluidic shear force sensor skin,” *Sensors and Actuators A: Physical*, vol. 264, pp. 289 – 297, 2017. doi:10.1016/j.sna.2017.08.001.

[36] A. Charalambides and S. Bergbreiter, “A novel all-elastomer MEMS tactile sensor for high dynamic range shear and normal force sensing,” *Journal of Micromechanics and Microengineering*, vol. 25, p. 095009, aug 2015. doi:10.1088/0960-1317/25/9/095009.

[37] A. S. Morris and R. Langari, “Chapter 13 - sensor technologies,” in *Measurement and Instrumentation (Second Edition)* (A. S. Morris and R. Langari, eds.), pp. 375 – 405, Boston: Academic Press, second edition ed., 2016. doi:10.1016/B978-0-12-800884-3.00013-7.

[38] S.-Z. Guo, K. Qiu, F. Meng, S. H. Park, and M. C. McAlpine, “3d printed stretchable tactile sensors,” *Advanced Materials*, vol. 29, no. 27, p. 1701218, 2017. doi:10.1002/adma.201701218.

[39] K. Noda, K. Hoshino, K. Matsumoto, and I. Shimoyama, “A shear stress sensor for tactile sensing with the piezoresistive cantilever standing in elastic material,” *Sensors and Actuators A: Physical*, vol. 127, no. 2, pp. 295 – 301, 2006. doi:10.1016/j.sna.2005.09.023.

[40] R. Li, Q. Zhou, Y. Bi, S. Cao, X. Xia, A. Yang, S. Li, and X. Xiao, "Research progress of flexible capacitive pressure sensor for sensitivity enhancement approaches," *Sensors and Actuators A: Physical*, p. 112425, 2020. doi:10.1016/j.sna.2020.112425.

[41] F. Zhu and J. Spronck, "A capacitive tactile sensor for shear and normal force measurements," *Sensors and Actuators A: Physical*, vol. 31, no. 1, pp. 115 – 120, 1992. doi:10.1016/0924-4247(92)80089-L.

[42] A. Albrecht, M. Trautmann, M. Becherer, P. Lugli, and A. Rivadeneyra, "Shear-force sensors on flexible substrates using inkjet printing," *Journal of Sensors*, vol. 2019, p. 1864239, 2019. doi:10.1155/2019/1864239.

[43] R. Brookhuis, T. Lammerink, and R. Wiegerink, "Differential capacitive sensing circuit for a multi-electrode capacitive force sensor," *Sensors and Actuators A: Physical*, vol. 234, pp. 168–179, 2015. doi:10.1016/j.sna.2015.08.020.

[44] Analog Devices, Norwood USA, *24-Bit Capacitance-to-Digital Converter with Temperature Sensor: AD7747*, 2007. Available online: `https://www.analog.com/en/products/ad7747.html#product-overview` [Accessed: 15-4-2020].

[45] D. J. Griffiths, *Introduction to Electrodynamics*, ch. 2. Electrostatics, p. 59–112. Cambridge University Press, 4 ed., 2017.

[46] R. P. Feynman, R. B. Leighton, and M. L. Sands, *The Feynman lectures on physics*, book II-4. Electrostatics. Reading, Mass.: Addison-Wesley Pub. Co., 1963. Available online: `https://www.feynmanlectures.caltech.edu/II_04.html` [Accessed: 4-2-2021.

[47] A. Dijkshoorn, M. Schouten, G. Wolterink, R. Sanders, S. Stramigioli, and G. Krijnen, "Characterizing the electrical properties of anisotropic, 3d-printed conductive sheets for sensor applications," *IEEE Sensors Journal*, vol. 20, no. 23, pp. 14218–14227, 2020. doi:10.1109/JSEN.2020.3007249.

[48] C. Shemelya, L. Banuelos-Chacon, A. Melendez, C. Kief, D. Espalin, R. Wicker, G. Krijnen, and E. MacDonald, "Multi-functional 3d printed and embedded sensors for satellite qualification structures," in *2015 IEEE SENSORS*, pp. 1–4, 2015. doi:10.1109/ICSENS.2015.7370541.

[49] H. E. Green, "A simplified derivation of the capacitance of a two-wire transmission line," *IEEE Transactions on Microwave Theory and Techniques*, vol. 47, no. 3, pp. 365–366, 1999. doi:10.1109/22.750243.

[50] S. Friedel, "How to calculate a capacitance matrix in comsol multiphysics®," Jun 2017. Available online: `https://www.comsol.com/blogs/how-to-calculate-a-capacitance-matrix-in-comsol-multiphysics/` [Accessed: 27-2-2021].

[51] COMSOL, *LiveLink^{TM} for* MATLAB® *Manual*, COMSOL 5.4 ed., 2018. Available online: `https://doc.comsol.com/5.4/doc/com.comsol.help.llmatlab/LiveLinkForMATLABUsersGuide.pdf` [Accessed: 27-2-2021].

[52] R. Hibbeler, *Mechanics of Materials*, ch. 3. Mechanical Properties of Materials. Pearson Prentice Hall, eighth ed., 2011. pp. 81–118.

[53] R. Hibbeler, *Mechanics of Materials*, ch. 10. Strain Transformation. Pearson Prentice Hall, eighth ed., 2011. pp. 485–537.

[54] Ultimaker, Geldermalsen, The Netherlands, *Technical Data Sheet PLA*, 4.002 ed., 2018. Available online: `https://support.ultimaker.com/hc/en-us/sections/360003504300` [Accessed: 7-3-2021].

[55] BCN3D Filaments, *Technical Data Sheet PLA*, 2021. Available online: `https://www.bcn3d.com/technical-safety-datasheets/` [Accessed: 7-3-2021].

[56] NinjaTek, Manheim, USA, *Technical specifications-metric*. Available online: `https://ninjatek.com/tech-specs/` [Accessed: 7-3-2021].

[57] J. T. Cantrell, S. Rohde, D. Damiani, R. Gurnani, L. DiSandro, J. Anton, A. Young, A. Jerez, D. Steinbach, C. Kroese, *et al.*, "Experimental characterization of the mechanical properties of 3d-printed abs and polycarbonate parts," *Rapid Prototyping Journal*, 2017. doi:10.1007/978-3-319-41600-7_11.

[58] BASF 3D Printing Solutions BV, Emmen, The netherlands, *Technical Data Sheet Ultrafuse PET*, 3.2 ed., 2019. Available online: `https://www.ultrafusefff.com/pet-technical-data/` [Accessed: 7-3-2021].

[59] NinjaTek, Manheim, USA, *NinjaFlex 3D Printing Fillament: Flexible Polyurethane Material for FDM printers (Technical Specifications)*. Available online: `https://ninjatek.com/ninjaflex/`. [Accessed: 23-02-2021].

[60] H. J. Qi and M. C. Boyce, "Stress–strain behavior of thermoplastic polyurethanes," *Mechanics of materials*, vol. 37, no. 8, pp. 817–839, 2005.

[61] NinjaTek, Manheim, USA, *SemiFlex 3D Printing Fillament: Flexible Polyurethane Material for FDM printers (Technical Specifications)*.

[62] NinjaTek, Manheim, USA, *Armadillo 3D Printing Fillament: Semi-rigid Polyurethane Material for FDM printers (Technical Specifications)*. Available online: `https://ninjatek.com/armadillo/`. [Accessed: 10-03-2021].

[63] E. Carrera, G. Giunta, and M. Petrolo, *Beam Structures: Classical and Advanced Theories*, ch. 2. The Euler–Bernoulli and Timoshenko Theories, pp. 9–22. John Wiley & Sons, Ltd, 2011. doi:10.1002/9781119978565.ch2.

[64] G. R. Cowper, "The Shear Coefficient in Timoshenko's Beam Theory," *Journal of Applied Mechanics*, vol. 33, pp. 335–340, 06 1966. doi:10.1115/1.3625046.

[65] A. Bower, *Applied Mechanics of Solids*, ch. 3. Constitutive Models – Relations between Stress and Strain. CRC Press, 2009.

[66] G. Marckmann and E. Verron, "Comparison of Hyperelastic Models for Rubber-Like Materials," *Rubber Chemistry and Technology*, vol. 79, pp. 835–858, 11 2006. doi:10.5254/1.3547969.

[67] T. Reppel and K. Weinberg, "Experimental determination of elastic and rupture properties of printed ninjaflex," *Technische Mechanik-European Journal of Engineering Mechanics*, vol. 38, no. 1, pp. 104–112, 2018. doi:10.24352/UB.OVGU-2018-010.

[68] L. He, J. Lou, Y. Dong, S. Kitipornchai, and J. Yang, "A shearable and thickness stretchable finite strain beam model for soft structures," *Meccanica*, vol. 53, no. 15, pp. 3759–3777, 2018. doi:10.1007/s11012-018-0905-4.

[69] Mathworks, *Equation Solving Algorithms*, 2021. Available online: `https://nl.mathworks.com/help/optim/ug/equation-solving-algorithms.html` [Accessed:30-03-2021].

[70] J. C. Lagarias, J. A. Reeds, M. H. Wright, and P. E. Wright, “Convergence properties of the nelder–mead simplex method in low dimensions,” *SIAM Journal on optimization*, vol. 9, no. 1, pp. 112–147, 1998. doi:10.1137/S1052623496303470.

[71] Mathworks, *Optimizing Nonlinear Functions*, 2021. Available online: `https://nl.mathworks.com/help/matlab/math/optimizing-nonlinear-functions.html`[Accessed: 10-04-2021].

[72] SMAC Corporation, California, *Linear actuators: LCA series*, 2021. Available online: `https://www.smac-mca.com/products/linear-actuators/lca-series` [Accessed: 15-4-2020].

[73] D. Kosmas, “Model-based hysteresis compensation and control with 3d printed lousy sensors,” Master’s thesis, University of Twente, October 2020. Available online: `http://purl.utwente.nl/essays/84814` [Accessed: 20-4-2021].